

PRODUCTION OF LONG-CHAIN OLEFIN AND FATTY ALCOHOL
FROM BIODIESEL OVER COPPER PHYLLOSILICATE BASED
CATALYSTS



A THESIS SUBMITTED IN PARTIAL FULFILLMENT OF THE REQUIREMENT FOR THE
DEGREE OF DOCTOR OF PHILOSOPHY IN APPLIED CHEMISTRY
DEPARTMENT OF CHEMISTRY SCHOOL OF SCIENCE
KING MONGKUT'S INSTITUTE OF TECHNOLOGY LADKRABANG
2023

KMITL-2023-SC-D-012-066

This material is reserved for educational use only, not allowed for commercial use.

Forbidden to modify the content, and cite the document when use.



COPYRIGHT 2023

SCHOOL OF SCIENCE

KING MONGKUT'S INSTITUTE OF TECHNOLOGY LADKRABANG

This material is reserved for educational use only, not allowed for commercial use.

Forbidden to modify the content, and cite the document when use.

Thesis Title	Production of Long-chain Olefin and Fatty Alcohol from Biodiesel over Copper Phyllosilicate Based Catalysts
Student Name	Warot Prasanseang
Student ID	61605010
Degree	Doctor of Philosophy (Applied Chemistry)
Department	Chemistry
Year	2023
Thesis Advisor	Prof. Dr. Tawan Sooknoi
Thesis Co-advisor	Assoc. Prof. Dr. Kittisak Choojun

Abstract

This thesis focuses on the production of linear long-chain α -olefins and fatty alcohols from biodiesel over copper phyllosilicate (CuPS) based catalysts. The reactions were carried out in a fixed-bed reactor at 250 °C under atmospheric H₂ pressure, using Methyl palmitate (MP) as a feed model. The CuPS catalysts (8-30 wt.% Cu) were prepared by ammonia evaporation-hydrothermal method. The crystal structure, surface area, reducibility, Cu dispersion, Cu particle size and acidity of the catalysts were examined by XRD, BET, H₂-TPR, TEM, NH₃-TPD and Py-IR. The existence of Cu²⁺ species (octahedral (O_h)/square planar (Sq)), Cu⁺ and Cu⁰ upon calcination/reduction was investigated by *in situ* TR-XANES. The Cu dispersion was related to the Cu⁺ fraction in CuPS, while Brønsted acid sites (BAS) depends on Cu⁰ particles. The MP conversion to 1-hexadecene proceeds via hydrogenation-dehydration promoted by the synergy of Cu⁰ surface and BAS at the interface. The α -olefin selectivity depends on a balance between Cu⁺ and Cu loading. 20CuPS possessing 10% Cu⁺ fraction provides a high conversion at 72% with 45% α -olefin selectivity. In another approach, Cu⁺ species and BAS of CuPS were tuned by doping with K⁺ for selective hydrogenation of methyl palmitate to hexadecanol. The catalysts were prepared by impregnating K⁺ on reduced and non-reduced CuPS. *In situ* TR-XANES and Py-IR suggest that the presence of K⁺ could stabilize Cu⁺ species and neutralize BAS. As compared to the non-reduced sample, K⁺ loading (0.01–0.10 wt%) on the reduced CuPS provide higher Cu⁺ fraction (10–16%), lower BAS (0.82 to 0.16 $\mu\text{mol/g}$)

This material is reserved for educational use only, not allowed for commercial use.

and lower Cu dispersion (75 to 52%). A balance between Cu^0 active surface and Cu^+ content provides an optimum hydrogenation activity (up to 80 %). The increased Cu^+ species, together with the decreased BAS, does not only enhance the catalyst stability, but also hexadecanol selectivity (from 35 to 60%, at ~50% conversion).

Keywords: Hydrodeoxygenation, Selective hydrogenation, Copper phyllosilicate, Potassium doping, Methyl palmitate; Fatty acid methyl esters; FAMES



Acknowledgements

Foremost, I would like to express my sincere thanks to my advisor, Prof. Dr. Tawan Sooknoi, and my co-advisor, Assoc. Prof. Dr. Kittisak Choojun, for their supervision, helpful suggestions on catalysis, skill coaching, and encouragement throughout my Ph.D. research. Also, I would like to thank for the valuable comments by the examination committee, including Assoc. Prof. Dr. Siriporn Jongpatiwut (Chairperson), Dr. Yingyot Poo-Arporn, Assoc. Prof. Dr. Panpailin Seeharaj and Asst. Prof. Dr. Chaval Sriwong.

I would like to thank the Department of Chemistry, School of Science, King Mongkut's Institute of Technology Ladkrabang (KMIL) for workplace and facility. I would like to acknowledge the KMIL Doctoral Scholarship (KDS2018/009) for financial support.

I very appreciate to our collaborators: Dr. Yingyot Poo-Arporn from Synchrotron Light Research Institute (SLRI) for XAS experiments and analysis, Prof. Dr. Yu-Chuan Lin from National Cheng Kung University (NCKU), Taiwan for the Pyridine adsorption FTIR results, Dr. Po-Wen Chung from Institute of Chemistry, Academia Sinica for the TEM images. I also would like to thank Asst. Prof. Dr. Watchareeya Kaveevitthai from NCKU for giving a short-term experience with her laboratory as a visiting student.

I would like to thank all staff members of the School of Science, KMIL and also colleagues, and members in the Catalytic Chemistry Research Unit (CCR) for help and advice on my research.

Finally, this success could not have happened without support from my family. I would like to dedicate this work to them who have tremendously inspired and encouraged me throughout this Ph.D. Thesis.

Mr. Warot Prasanseang

Table of Contents

	Page
Abstract	i
Acknowledgements.....	iii
Table of Contents.....	iv
List of Tables	vii
List of Figures.....	viii
List of Schemes.....	xi
Abbreviations/Symbols.....	xii
Chapter 1 Introduction	1
1.1 Research Motivation	1
1.2 Objectives of the study.....	3
1.3 Scopes of the study.....	4
1.4 Benefits of the study	5
Chapter 2 Theory and Literature Reviews	6
2.1) Biomass.....	6
2.2) Palm oil	7
2.3) Biodiesel.....	8
2.3.1) Definition of biodiesel	8
2.3.2) The benefit of biodiesel	9
2.3.3) The production of FAMES.....	11
2.4) Methyl palmitate	13
2.5) Linear long-chain α -olefin	14
2.6) Hydrodeoxygenation of FAMES.....	15
2.7) Fatty alcohols.....	17
2.8) Hydrogenation of FAMES.....	19
2.9) Phyllosilicate	22
2.9.1) Synthesis of copper phyllosilicate (CuPS).....	22

This material is reserved for educational use only, not allowed for commercial use.

Forbidden to modify the content, and cite the document when use.

Table of Contents (Continued)

	Page
2.9.2) Characterization of copper phyllosilicate (CuPS)	23
2.9.3) Catalytic hydrogenation of esters on CuPS catalysts	25
2.10) Potassium doping on Cu catalysts.....	28
2.11) Literature reviews.....	30
Chapter 3 Research Methodology	36
3.1 Chemicals and materials.....	36
3.2 Instrument and apparatus	37
3.3 Catalysts preparation.....	37
3.3.1 Copper phyllosilicate catalyst (CuPS)	37
3.3.2 Copper supported on silica (Cu/SiO ₂)	38
3.3.3 K-doped on copper phyllosilicate (K-CuPS).....	38
3.3.4 K-doped on reduced copper phyllosilicate (K-rCuPS).....	38
3.4 Catalyst characterizations	38
3.4.1 X-ray Fluorescence (XRF).....	38
3.4.2 Inductively coupled plasma-optical emission spectroscopy (ICP).....	39
3.4.3 X-ray Diffraction (XRD)	39
3.4.4 Surface area analysis (BET).....	39
3.4.5 Hydrogen Temperature programmed reduction (H ₂ -TPR).....	39
3.4.6 Ammonia Temperature programmed desorption (NH ₃ -TPD)	40
3.4.7 Pyridine-adsorbed infrared spectroscopy (Py-IR)	40
3.4.8 Dissociative N ₂ O adsorption using H ₂ -TPR	40
3.4.9 Transmission electron microscopy (TEM).....	41
3.4.10 <i>In situ</i> X-ray absorption near-edge structure spectroscopy.	41
3.5 Catalytic activity.....	43

This material is reserved for educational use only, not allowed for commercial use.

Forbidden to modify the content, and cite the document when use.

Table of Contents (Continued)

	Page
Chapter 4 Linear long-chain α-olefins from Hydrodeoxygenation of Methyl palmitate over Copper phyllosilicate catalysts	45
4.1 Results and discussion.....	46
4.1.1 Characterization of catalysts	46
4.1.2 Catalytic activity.....	56
4.2 Conclusion	61
Chapter 5 Tuning Cu⁺ species/Brønsted acids of Copper phyllosilicate by K⁺ doping for Selective Hydrogenation of Methyl palmitate to Hexadecanol	63
5.1 Results and discussion.....	64
5.1.1 Characterization of catalysts	64
5.1.2 Catalytic activity.....	74
5.2 Conclusion	83
Chapter 6 Conclusions and Suggestions	84
6.1 Conclusions.....	84
6.2 Suggestions	86
References.....	87
Appendices	96
Supporting information in chapter 4	97
Supporting information in chapter 5	101
Temperature program condition for all experiments.....	105
Calculations.....	109
The linear combination fitting (LCF) from <i>in situ</i> TR-XANES.....	121
Author Biography	133

List of Tables

Table	Page
2.1. Compositions of fatty acid in palm oil (SFAs; saturated fatty acid MUFAs; mono-unsaturated fatty acid and PUFAs; polyunsaturated fatty acid).....	8
2.2 Comparison of the properties between biodiesel and conventional diesel.....	10
2.3. The list of FAMEs and their structures.....	12
2.4. Chemical and physical properties of methyl palmitate.....	13
3.1. List of chemicals.....	36
3.2. Operating condition of gas chromatography.....	44
4.1. Metal loading, surface area, pore size, pore volume, H ₂ -consumption, Cu surface area and Cu dispersion of CuPS and Cu/SiO ₂ samples.....	46
4.2 Acidity and type of acid sites of all reduced catalysts.....	55
4.3. Catalytic activity, product yields and selectivity in hydrodeoxygenation of methyl palmitate over CuPS catalysts.....	56
5.1 Cu and K ⁺ loading, surface area, pore size, pore volume, H ₂ -consumption, specific Cu surface area and Cu dispersion of all catalysts.....	64
5.2 Acidity and type of acid sites of all catalysts.....	74
5.3 Fatty alcohol selectivity from ester hydrogenation over various Cu-based catalysts.....	78
5.4 Catalytic activity and product yields in hydrogenation of methyl palmitate over K ⁺ doped catalyst.....	79
5.5 Fatty alcohol selectivity from gas phase conversion of methyl palmitate in the fixed-bed reactor over various catalysts.....	82

List of Figures

Figure	Page
2.1 The photosynthesis process of plant to produce glucose ($C_6H_{12}O_6$) and biomass resource.....	6
2.2 Triglyceride components and structures.....	7
2.3 The example of biodiesel of fatty acid methyl ester structures derived from C_{18} -FAMES.....	9
2.4 Transesterification of triglycerides with methanol to produce FAMES.....	11
2.5 Transesterification mechanism of triglyceride using basic catalyst.....	12
2.6 Chemical structure of methyl palmitate.....	13
2.7 Chemical structure of Linear long-chain α -olefin.....	14
2.8 The oligomerization of ethylene to linear long-chain α -olefin.....	14
2.9 The application of linear alpha olefin in chemical industry.....	15
2.10 a) the decarboxylation and b) deoxygenation of fatty acids over Pt based catalyst.....	16
2.11 The summarizes deoxygenation pathway of FAMES.....	17
2.12 The example of fatty alcohol molecules.....	17
2.13 The hydrogenation of FAMES to fatty alcohols.....	18
2.14 Fatty alcohol applications.....	19
2.15 The general step of FAMES hydrogenation.....	20
2.16 Mechanism of the direct hydrogenation of FAMES to fatty alcohol over $RuSnB/Al_2O_3$ catalyst.....	21
2.17 The formation of 1:1 phyllosilicate structure.....	22
2.18 The preparation of CuPS by AHM.....	23
2.19 The synergetic effect between Cu^0 and Cu^+ of CuPS catalyst on the hydrogenation.....	26
2.20 Reaction pathway of the hydrogenation of esters (DMO and DEO) to MG, EG, and EtOH.....	27
2.21 The crystal structure of potassium oxide (K_2O).....	28

List of Figures (Continued)

Figure	Page
2.22 The effect of K doping on a) acidity b) basicity and c) reducibility	29
3.1 Temperature program of <i>in situ</i> XANES experiments.....	42
3.2. Catalytic system of metal palmitate conversion.	43
4.1 XRD patterns of a) calcined and b) reduced CuPS and Cu/SiO ₂ samples	47
4.2 Cu K edge XANES spectra of a) Cu standards and b) CuPS samples and 20Cu/SiO ₂ after calcination at 400 °C for 2 h.....	48
4.3 Fractions of Cu ²⁺ species from LCF of a) 8CuPS, b) 20CuPS, c) 30CuPS and d) 20Cu/SiO ₂ upon calcination.....	49
4.4 a) H ₂ -TPR profiles (from 50-900°C) and b) first H ₂ -TPR (solid line) and second H ₂ - TPR (dash line) (from 50-250°C) after dissociative N ₂ O adsorption for i) 20Cu/SiO ₂ , ii) 8CuPS, iii) 20CuPS and iv) 30CuPS.....	50
4.5 Fractions of Cu species from the LCF of a) 8CuPS, b) 20CuPS, c) 30CuPS and d) 20Cu/SiO ₂ under upon the reduction.	51
4.6 TEM images and particle size distribution histograms of a) 8CuPS, b) 20CuPS, c) 30CuPS and d) 20Cu/SiO ₂	53
4.7 a) NH ₃ -TPD desorption profiles and b) pyridine-adsorbed IR spectra of i) 20Cu/SiO ₂ , ii) 8CuPS, iii) 20CuPS and iv) 30CuPS	54
4.8 The relationship between a) Lewis acid sites (LAS) vs Cu ⁺ content and b) Brønsted acid sites (BAS) vs Cu ⁰ content.....	56
4.9 Methyl palmitate conversion and yields vs. contact time of 20CuPS catalyst	57
4.10 Products selectivity vs. conversion of 20CuPS catalyst.....	58
4.11 The relationship between a) conversion vs Cu surface area and b) Products selectivity and Brønsted acid sites vs Cu loadings	59
4.12 Product selectivity at 20% of conversion vs Cu ⁺ fractions in CuPS catalysts	61
5.1 a) The XRD pattern, b) the H ₂ -TPR profiles, and c-e) TEM images of the CuPS samples.....	65

List of Figures (Continued)

Figure	Page
5.2 XANES spectra of CuPS and 0.05K-CuPS after a) impregnation c) calcination and e) reduction, The first derivative of CuPS and 0.05K-CuPS after b) impregnation d) calcination and f) reduction	68
5.3 a) <i>in situ</i> TR-XANES spectra of 0.05K-CuPS during the calcination and b) linear combination fitting (LCF)	69
5.4 The <i>in situ</i> TR-XANES spectra during reduction of a) CuPS b) 0.05K-CuPS c) 0.05K-rCuPS and the linear combination fitting of a) CuPS and b) 0.05K-CuPS and c) 0.05K-rCuPS	70
5.5 Acidity of CuPS, 0.05K-CuPS and 0.05K-rCuPS, a) the <i>in situ</i> pyridine-adsorbed infrared spectra (Py-IR) and b) NH ₃ temperature-programmed desorption (NH ₃ -TPD)	73
5.6 The catalytic activity of CuPS, 0.05K-CuPS, and 0.05K-rCuPS for methyl palmitate hydrogenation.....	75
5.7 The relationship between conversion Vs. a) specific Cu surface area and b) Cu ⁺ content and the relationship between hexadecanol selectivity Vs. c) Cu ⁺ content and d) BAS	76
5.8 Conversion and hexadecanol selectivity over various CuPS based catalysts and impregnated Cu/SiO ₂ catalyst	78
5.9 Relationship between K ⁺ loading with a) conversion, specific Cu surface area and Cu ⁺ content b) hexadecanol selectivity, BAS and Cu ⁺ content.....	80
5.10 The LCF of <i>in situ</i> TR-XANES spectra of a) 0.01K-rCuPS d) 0.10K-rCuPS, TEM of b) 0.01K-rCuPS and e) 0.10K-rCuPS, the H ₂ -TPR profiles of c) 0.01K-rCuPS and f) 0.10K-rCuPS.....	80
5.11 The total acidity from a) NH ₃ -TPD and b) <i>in situ</i> pyridine-adsorbed infrared spectra (Py-IR) of 0.01K-rCuPS, 0.05K-rCuPS and 0.10K-rCuPS.....	81
5.12 The catalytic stability of a) CuPS and b) 0.05K-rCuPS over 5 hours of time on steam at 374 g [•] h/mol of contact time.....	82

List of Schemes

Scheme	Page
4.1 The demonstration of $\text{Cu}^{2+}(\text{O}_h)$ transformation to $\text{Cu}^{2+}(\text{Sq})$ under the calcination at 400 °C.....	49
4.2 Propose reaction pathway of methyl palmitate conversion over CuPS catalysts .	59
5.1 The demonstration of K^+ doping on CuPS forming 0.05K-CuPS.....	67
5.2 The change of coordination on $\text{Cu}^{2+}(\text{O}_h)$ to $\text{Cu}^{2+}(\text{Sq})$ during reduction under H_2 atmospheres	71
5.3 The demonstration of K^+ doping on rCuPS forming 0.05K-rCuPS	72
5.4 Proposed mechanism of hydrogenation-dehydration of methyl palmitate.....	75



Abbreviations/Symbols

°C	Celcius
wt. %	%Weight by weight
Å	Aungstorm
AHM	Ammonia evaporation and hydrothermal method
Al ₂ O ₃	Aluminum oxide
Ar	Argon
ASA	Alkyl succinic anhydride
ASTM	American Society for Testing and Materials
Atm	Atmospheric pressure at sea level
B	Boron
Ba	Barium
BAS	Brønsted acid
BET	Brunauer–Emmett–Teller
HMF	5-hydroxymethylfurfural
BHMF	2,5-bis(hydroxymethyl)furan
BTU	British thermal unit
CaF ₂	Calcium fluoride
Ce	Cerium
Cl	Chlorine
cm ³	Cubic centimeter
Co	Cobalt
CO	Carbon monoxide
CO ₂	Carbon dioxide
CPO	Crude palm oil
Cr	Chromium
Cs	Cesium
Cu	Copper
CuPS	Copper phyllosilicate
D _{Cu}	Copper dispersion
DEO	Diethyl oxalate

This material is reserved for educational use only, not allowed for commercial use.

Forbidden to modify the content, and cite the document when use.

Abbreviations/Symbols (Continued)

DI	Deionized water
DMO	Dimethyl oxalate
EG	Ethylene glycol
EtOH	Ethanol
eV	Electron volt
F	Fluorine
FAMEs	Fatty acid methyl esters
Fe	Iron
FFAs	Free fatty acids
FID	Flame ionization detector
g	Gram
GC	Gas chromatography
h	hour
H ₂	Hydrogen gas
H ₂ O	Water
H ₂ SO ₄	Sulfuric acid
HDO	Hydrodeoxygenation
He	Helium
HMF	5-hydroxymethylfurfural
ICP-OES	Inductively coupled plasma atomic emission spectroscopy
K	Potassium
K ₂ O	Potassium oxide
KCO ₃	Potassium carbonate
KNO ₃	Potassium nitrate
LAS	Lewis acid
lb	Pound
LCF	Linear combination fitting
Li	Lithium
LLAO	Linear long-chain alpha olefin
Mg	Magnesium

This material is reserved for educational use only, not allowed for commercial use.

Forbidden to modify the content, and cite the document when use.

Abbreviations/Symbols (Continued)

MG	Methyl glycolate
mg	Milligram
mL	Milliliter
mm	Millimeter
mmol	Millimole
mol	Mole
MP	Methyl palmitate
MUFAs	Mono-unsaturated fatty acid
N ₂	Nitrogen gas
N ₂ O	Nitrous oxide gas
Na	Sodium
NaOH	Sodium hydroxide
NH ₃	Ammonia gas
Ni	Nickle
nm	Nanometer
NO _x	Nitrogen oxides
O	Oxygen
O.D.	Outside diameter
OH	Hydroxide
O _n	Octahedral
Pd	Palladium
PM	Particular matter
ppm	Part per million
Pt	Platinum
PUFAs	Poly unsaturated fatty acid
Py-IR	Pyridine-adsorbed infrared spectroscopy
Ru	Ruthenium
SFAs	Saturated fatty acid
Si	Silicon
SiO ₂	Silicon dioxide

This material is reserved for educational use only, not allowed for commercial use.

Forbidden to modify the content, and cite the document when use.

Abbreviations/Symbols (Continued)

SLRI	Synchrotron Light Research Institute
Sn	Tin
Sq	Square planar
Sr	Strontium
TAG	Triglyceride
TCD	Thermal conductivity detector
TEM	Transmission electron microscopy
TGA	Thermogravimetric analysis
TOF	Turnover frequency
TPR	Temperature program reduction
TR-XANES	Time-resolved X-ray adsorption near-edge structure spectroscopy
W	Tungsten
XAS	X-ray absorption spectroscopy
XPS	X-ray photoelectron spectroscopy
XRD	X-ray powder diffraction
XRF	X-ray fluorescence spectrometer
Zr	Zirconium
α	Alpha
η	Eta
μ	Micro
θ	theta

Chapter 1

Introduction

1.1 Research Motivation

Biodiesels, known as fatty acid methyl esters (FAMES), are typically obtained from the transesterification of palm oils. Accordingly, FAMES are classified as an alternative renewable bio-based chemical to substitute the petroleum fuels.¹⁻² Due to the large supply of palm oils in South east Asia, South America, and North America³⁻⁴, the production of FAMES has been rapidly increased with the average growth of 11% per year. However, the consumption, mainly as biodiesels, is relatively steady and tends to decrease in 2030 due to the electric vehicle development.⁵⁻⁶ In turn, this brings out the opportunity to use FAMES as a feedstock to produce key intermediate chemicals for the industries since the production of FAMES has commercially developed.

In general, the molecule of FAMES is more readily converted to fatty alcohol, linear long-chain α -olefins and long-chain paraffins.⁷⁻¹⁰ Amongst these products, linear long-chain α -olefins and fatty alcohols have more valuable than others due to their widely applications. Linear long-chain α -olefins have been used as a lubricant and surfactant. Fatty alcohols are widely applied for cosmetic pharmaceutical industries.¹¹⁻¹² In order to obtain these products selectively from FAMES, the catalyst design and the reaction conditions need to be developed and optimized.

Typically, the hydrodeoxygenation of FAMES to linear long-chain α -olefins can proceed via decarbonylation¹³⁻¹⁴ or hydrogenation-dehydration.¹⁵ Even though supported Ni¹⁶⁻¹⁷ and Co¹⁸⁻¹⁹ catalysts had been reported to effectively promote the decarbonylation of FAMES. The loss of carbon backbone from FAMES as a CO, yielding one short-carbon backbone α -olefins is obtained over these catalysts. Moreover, the fast deactivation due to the coke formation is normally observed. On the other hand, hydrogenation-dehydration of FAMES could provide long-chain α -olefins without carbon loss. In this reaction, FAMES molecule is hydrogenated at the C=O bond of ester group to form fatty alcohol, which can be subsequently dehydrated to linear long-chain α -olefin.¹⁵ Therefore, a bifunctional catalyst consisting of a chemoselective metal for C=O hydrogenation and acid sites for alcohol dehydration is required for the

hydrogenation-dehydration system. In addition, the decarbonylation should be suppressed over this bifunctional catalyst.

Cu-based catalysts tend to perform the hydrogenation over the decarbonylation, especially those with the Cu^+ species. This is because the Cu^+ would interact with C=O bond of ester groups via η^1 -adsorption.²⁰ Pestman. *et al.* (1997) suggested that the presence of Cu^+ and Cu^0 species in the Cu-based catalysts were responsible for C=O interaction and C=O hydrogenation, respectively.²¹⁻²² Moreover, the present of Cu^+ on the catalyst would provide the acid site for the subsequent dehydration of the alcohol product.²³ However, maintaining both Cu^+ and Cu^0 species in the catalysts with high Cu dispersion is challenging because the poor interaction between the metal and the support. Furthermore, the Cu agglomeration and sintering tend to occur when the Cu loading is >10 wt.%.²⁴⁻²⁶

Recently, the copper catalysts derived from copper phyllosilicate (CuPS) precursor have been reported to provide a high Cu dispersion with Cu^+ and Cu^0 species after the reduction even at >20wt.% of Cu loading.^{22,27} This is due to a strong interaction between Cu^{2+} and SiO_2 in the lamellar structure.²⁸⁻³⁰ Furthermore, the chrysocolla structure of CuPS could offer additional Brønsted acid sites (BAS) from surface silanol groups.³¹ Che. *et al.* (2011) mentioned that the condensation of $\text{Si-O-M}^{2+}\text{-OH}$ species in the octahedral layer of phyllosilicate structure during the calcination yielded MO_x clusters and Si-OH .³² Such generated silanols, especially those at the perimeter of metal particles, could have a stronger Brønsted acidity than that of the typical silanol.³¹ Accordingly, this could lead CuPS to act as a bifunctional catalyst for hydrogenation-dehydration of FAMES to produce long-chain α -olefins.

In turn, the CuPS catalysts without BAS could yield only fatty alcohols since the hydrogenation-dehydration is a series reaction where the fatty alcohol would be firstly generated followed by the dehydration to linear long-chain α -olefins. The BAS of CuPS could be reduced by adding the secondary basic metal, such as Li, Na, K, and Cs. Li. *et al.* (2022) reported the addition of alkali metal (Li, Na, K, Cs) over CuMgCe catalysts promoted *iso*-butanol selectivity from syn-gas reaction.³³ Among these alkali metals, the doped K^+ over CuMgCe provided the optimum basicity, yielding the highest *iso*-butanol selectivity. In similar manner, Hu. *et al.* (2018) reported that the doped K over $\text{Cu/Al}_2\text{O}_3$ catalyst could prevent the dehydration of 2,5-bis(hydroxymethyl)furan (BHMF) from the hydrogenation of 5-hydroxymethylfurfural (HMF).³⁴ Therefore, the

This material is reserved for educational use only, not allowed for commercial use.

doping of K on CuPS catalysts is a promising technique to reduce the acidity of CuPS catalysts for the production of fatty alcohols from FAMEs. In fact, K is cheap and easy to obtain, which is favorable in an industry.

Accordingly, this thesis focuses on i) the hydrogenation-dehydration of FAMEs to linear long-chain α -olefins using copper phyllosilicate (CuPS) as a bifunctional catalyst and ii) the selective hydrogenation of FAMEs to fatty alcohols using the modified CuPS by K doping (K-CuPS). Methyl palmitate (MP) was selected as a feed model from FAMEs. The CuPS catalysts were prepared by the ammonia evaporation and hydrothermal method (AHM) with 8, 20 and 30 wt.% of Cu loadings. The K-CuPS catalyst with 0.01, 0.05 and 0.10wt.% K loadings were prepared by the incipient wetness impregnation. The crystallinity and textural properties of catalysts were studied by XRD, TEM and BET. The reducibility and Cu dispersion were evaluated by H₂-TPR. The Cu species in these prepared samples were investigated by *in-situ* XANES technique. The acidity was evaluated by NH₃-TPD and pyridine-FTIR. The catalytic reaction was carried out in a continuous fixed-bed reactor at 250 °C under atmospheric H₂ pressure. The relationship between the active species and catalytic performance were demonstrated. The reaction pathways were also proposed.

1.2 Objectives of the study

- 1) To produce linear long-chain α -olefins from FAMEs via hydrogenation-dehydration using CuPS as a catalyst.
- 2) To obtain fatty alcohol from FAMEs via selective hydrogenation using K-CuPS as a catalyst.
- 3) To create the platform of FAMEs conversion using CuPS-based catalysts.
- 4) To understand the effect of Cu loadings, Cu dispersion, Cu active species and role of acidity of CuPS catalysts on the hydrogenation-dehydration of FAMEs.
- 5) To understand the effect of doped K over CuPS catalysts on the Cu dispersion, Cu active species, acidity, and the alcohol selectivity from the selective hydrogenation of FAMEs.
- 6) To optimize the reaction conditions related to these two reactions.
- 7) To understand the reaction mechanism pathways of these two reactions
- 8) To investigate the catalytic stability and recyclability of the CuPS based catalyst.

This material is reserved for educational use only, not allowed for commercial use.

Forbidden to modify the content, and cite the document when use.

1.3 Scopes of the study

1.3.1) Hydrogenation-dehydration of FAMEs to linear long-chain α -olefins using CuPS catalysts

1) To synthesize the CuPS catalysts with the difference Cu loading (8, 20 and 30 wt.%) by the ammonia evaporation and hydrothermal method (AHM) denote as 8CuPS, 20CuPS and 30CuPS. The 20wt.% Cu over silica (20Cu/SiO₂) was prepared by incipient wetness impregnation method for the comparison.

2) To characterize the catalysts by X-ray fluorescence spectrometer (XRF), X-ray powder diffraction (XRD), Nitrogen adsorption (BET), H₂-temperature-programmed reduction (H₂-TPR), Transmission electron microscope (TEM), *in situ* time-resolved X-ray adsorption near-edge structure spectroscopy (*in situ* TR-XANES), NH₃ temperature-programmed desorption (NH₃-TPD) and Pyridine-adsorbed infrared spectroscopy (Py-IR).

3) Investigate the catalytic activity of methyl palmitate conversion in a continuous fixed-bed reactor under the atmospheric H₂ pressure at 250 °C.

3.1) To compare the catalytic activity between 20CuPS and 20Cu/SiO₂ catalyst.

3.2) To investigate the effect of contact time and reaction pathway over 20CuPS catalyst.

3.3) To study the effect of Cu loading (8, 20 and 30 wt.%) on CuPS catalyst for the catalytic activity.

3.5) To investigate the effect of Cu species and acid sites toward the linear long-chain α -olefins.

1.3.2) Selective hydrogenation of FAMEs to fatty alcohols over K-CuPS catalysts

1) To synthesize the 20 wt.% CuPS catalyst (denote as CuPS) via the ammonia evaporation and hydrothermal method (AHM).

2) To preparation the K doping on CuPS and reduced CuPS (rCuPS) via impregnation method (0.01, 0.05 and 0.10 wt.% loadings).

3) To characterize the catalysts by X-ray fluorescence spectrometer (XRF), X-ray powder diffraction (XRD), Nitrogen adsorption, H₂-temperature-programmed reduction (H₂-TPR), Transmission electron microscope (TEM), *in situ* time-resolved X-ray

adsorption near-edge structure spectroscopy (*in situ* TR-XANES), NH₃ temperature-programmed desorption (NH₃-TPD) and Pyridine-adsorbed infrared spectroscopy (Py-IR)

5) To investigate the catalytic activity of methyl palmitate conversion in a continuous fixed-bed reactor under the atmospheric H₂ pressure at 250 °C.

5.1) To investigate the effect of K doping method on CuPS.

5.2) To investigate the effect of K loading on rCuPS catalysts (0.01, 0.05, and 0.10K-rCuPS) for the catalytic activity.

5.3) To evaluate the relationship between conversion and fatty alcohol selectivity of K-CuPS catalysts.

5.5) To examine the catalytic stability over time on steam of CuPS and K-CuPS catalyst.

1.4 Benefits of the study

This thesis would provide a new aspect and valuable knowledge of copper phyllosilicate-based catalysts (CuPS) for the catalytic conversion of FAMEs. In the first study, CuPS would act as a bifunctional catalyst for the production of linear long-chain α -olefins. This could presumably due to the cooperation between Cu active species and acid sites on the surface leading to the improving of hydrogenation-dehydration ability. For the second study, the acidity on CuPS surface would be modified with the K-doping to suppress the dehydration ability. This could produce a higher yield of fatty alcohol due to the naturalization of active BAS by K⁺. Therefore, the CuPS based catalysts would be a promising tunable catalyst for FAMEs conversion to produce linear long-chain α -olefins and fatty alcohol for many industries, such as lubricant, surfactant, cosmetic and pharmaceutical.

Chapter 2

Theory and Literature Reviews

2.1) Biomass

Biomass is renewable organic materials derived from plants and animals. Plant could produce biomass via the process called “Photo-synthesis”. This process takes place when the plant captures solar energy and reacts with carbon-dioxide (CO₂) and water to produce the chemical energy in form glucose (C₆H₁₂O₆) or sugar (Figure 2.1). Accordingly, the basic element of biomass includes carbon, hydrogen and oxygen.³⁵⁻³⁶

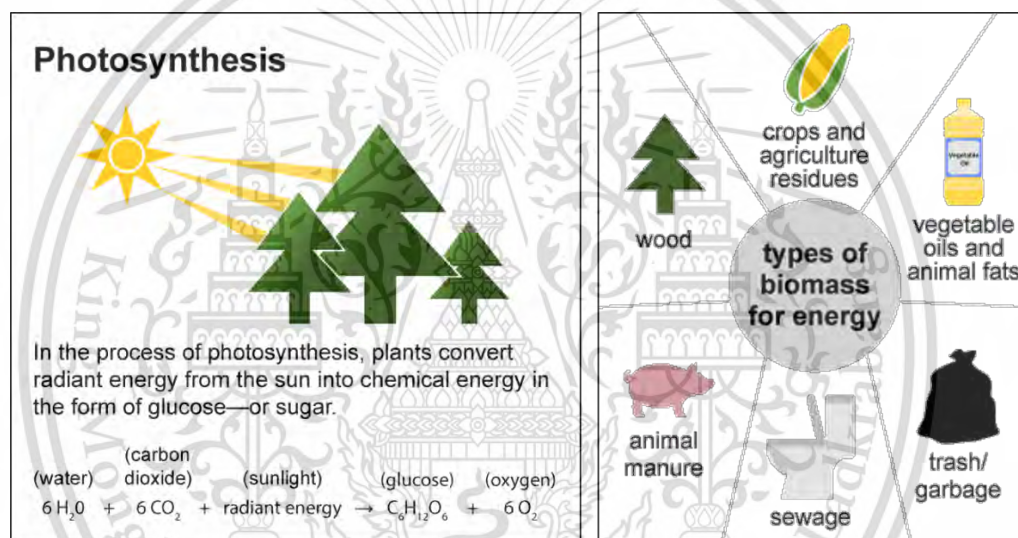


Figure 2.1 The photosynthesis process of plant to produce glucose (C₆H₁₂O₆) and biomass resource.

The source of biomass could be obtained from several feedstocks includes:

- **Wood and wood processing wastes**, such as wood pellet, wood chip, firewood, lumber, paper mill and sawdust.
- **Agricultural crop and materials**, such as vegetable oil, corn, soybean, sugar cane, switchgrass, crop and food process residual.
- **Biogenic materials**, such as paper, cotton, wool product and yard.
- **Animal manure and human sewage**, for producing biogas/renewable natural gas.

Table 2.1 Compositions of fatty acid in palm oil (SFAs; saturated fatty acid MUFAs; mono-unsaturated fatty acid and PUFAs; polyunsaturated fatty acid).

Fatty acids	Composition (%)
Caprylic (C8:0)	0.3±0.04
Caproic (C10:0)	0.2±0.01
Lauric (C12:0)	1.2±0.04
Myristic (C14:0)	1.6±0.02
Palmitic (C16:0)	41.8±0.35
Stearic (C18:0)	3.5±0.08
Oleic (C18:1)	37.4±0.40
Linoleic (C18:2)	14.1±0.06
SAFA	48.6
MUFA	37.4
PUFA	14.1

2.3) Biodiesel

Biodiesel is a renewable liquid fuel which used to replace conventional diesel produced from petroleum sources for diesel engines. It could be manufactured from several biomass feedstocks, such as vegetable oils, animal fats and cooking oils.

2.3.1) Definition of biodiesel

From the ASTM D6751 standard, the definition of biodiesel is stated that biodiesel is composed of “*mono-alkyl ester of long-chain fatty acids derived from plant oils or animal fats*”. This indicates that biodiesel contains only one ester linkage in each molecule.³⁹ Biodiesel could be produced from methyl, ethyl, isopropyl and other alcohols. However, most of biodiesel is based on methyl ester called “Fatty acid methyl ester” or FAMES. This is because the methanol using as an alcohol for producing FAMES are lower price, high conversion of FAMES and the excess methanol is easily to recycling from the finished FAMES product. The long-chain structure of

FAMES would be consisted of saturated, mono and poly-unsaturated molecules as shown as examples in the Figure 2.3.

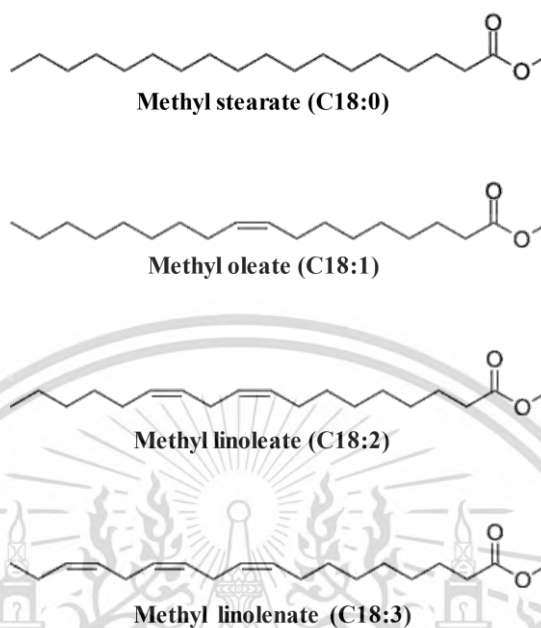


Figure 2.3 The example of biodiesel of fatty acid methyl ester structures derived from C₁₈-FAMES.

2.3.2) The benefit of biodiesel

Biodiesel can help several countries to reduce the usage of petroleum fuel because it is domestically product and can be used in any diesel engine with little or no modification of engine and fuel system. The additional benefits of biodiesel usage are also listed as shown;

- **Biodiesel reduces greenhouse gas emissions.**

Biodiesel can reduce the CO₂ emission 74% lower than petroleum diesel. This because the CO₂ emission from the biodiesel burning could be recycled for the photo synthesis of plant growth.

- **Biodiesel reduces tailpipe emission.**

Biodiesel is fully compatible the emission control catalyts and filters, which dramatically reduce the emission of nitrogen oxide (NO_x).

- **Biodiesel is good for human health.**

Biodiesel has lower particulate matter (PM) and hydrocarbon emission than petroleum diesel, which could be toxic and carcinogenic with human health.

- **Biodiesel improves engine operation.**

Biodiesel with a very low concentration could improve fuel lubricity and increase the cetane number of the fuel. This could prevent the moving parts in the engine from wearing prematurely.

- **Biodiesel is easy to use.**

Biodiesel can be blended, such as B20 (20% biodiesel in 80% conventional) or lower require no new equipment or modification. It can be stored and pumped with the same equipment as diesel fuel.

Moreover, biodiesel is not only a renewable and non-toxic fuel, but it has nearly the same properties as the petroleum diesel, as shown in Table 2.1.

Table 2.2 Comparison of the properties between biodiesel and conventional diesel.³⁹

Fuel property	Conventional diesel	Biodiesel
Fuel standard	ASTM D975	ASTM D6751
Higher heating value, Btu/gal	~138,490	~127,960
lower heating value, Btu/gal	~129,488	~119,550
Kinematic viscosity, @ 40°C	1.3 - 4.1	4.0 - 6.0
Specific gravity, @ 15.5°C	0.85	0.88
Density, lb/gal @ 15.5°C	7.1	7.3
Carbon, wt %	87	77
Hydrogen, wt %	13	12
Oxygen, by dif. wt %	0	11
Sulfur, wt % (ppm)	15 ppm	15 ppm
Boiling point (°C)	180 - 340	315 - 350
Flash point (°C)	60 - 80	100 - 170
Cloud point (°C)	-35 - 5	-3 - 15
Pour point (°C)	-35 - -15	-5 - 10
Cetane number	40 - 55	47 - 65

This material is reserved for educational use only, not allowed for commercial use.

Forbidden to modify the content, and cite the document when use.

2.3.3) The production of FAMES

Transesterification reaction is the most widely used to convert vegetable oils to FAMES. According to this approach, 1 mole of triglyceride reacts with 3 moles of methanol in the presence of acid or base catalysts, such as sodium hydroxide (NaOH) and sulfuric acid (H₂SO₄), to produce 3 moles of FAMES and 1 mole of glycerol, as shown in Figure 2.4.⁴⁰

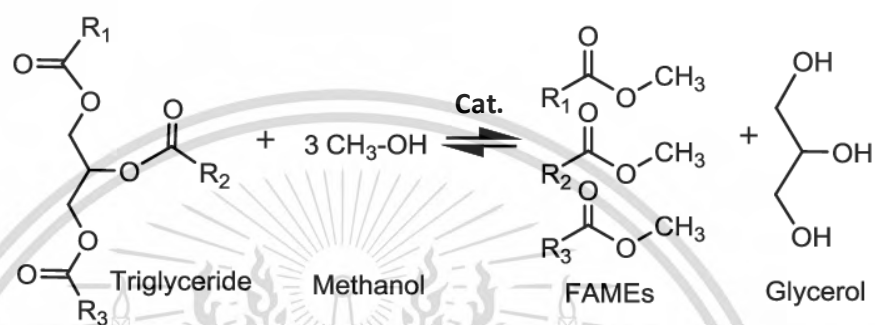


Figure 2.4 Transesterification of triglycerides with methanol to produce FAMES.

Transesterification using a homogenous catalyst is the first conventional method applied for FAMES production in the industrial scale. Traditionally, inorganic bases, such as alkali metal hydroxides and alkoxides are usually used as a catalyst. The transesterification is carried out in a batch reactor with an excess of methanol under mild conditions (30–70 °C, atmospheric pressure). In general, a basis homogenous catalyst provides a higher transesterification rate than an acid catalyst (Figure 2.5). The FAMES yield was 98% after 9 min at 60 °C in the presence of sodium hydroxide, while acids catalyst could yield 90% of FAMES after 12 h at 65–120 °C. However, the main disadvantage of the alkali homogeneous catalysts is their unsuitability for feedstock with high free fatty acids (FFAs) content.

In recent years, the transesterification of vegetable oils was conducted using a two-step process. The first step is an acid catalyzed reaction which involves the esterification of free fatty acid into FAMES. The reaction mixture is then washed and separated. After that, the reaction mixture is subjected to transesterification. The transesterification reaction is carried out for 30–60 min in the presence of potassium hydroxide. The total FAMES yield after these operations is 98–99%.⁴¹

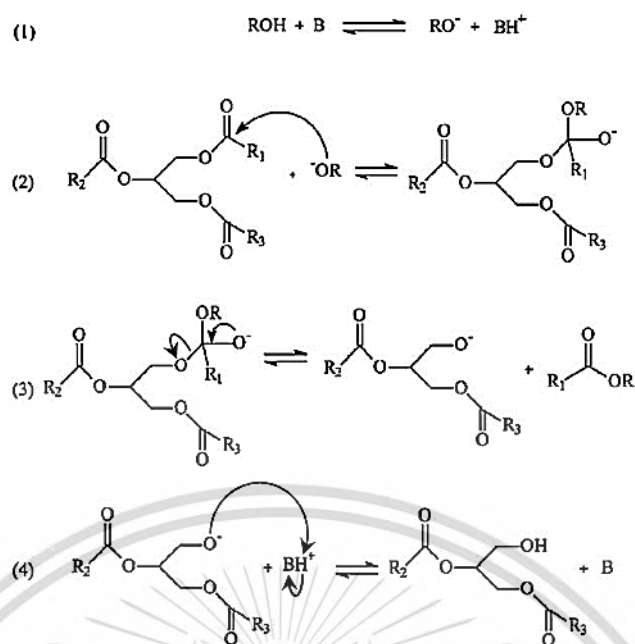


Figure 2.5 Transesterification mechanism of triglyceride using basic catalyst.

Chemically, FAMES are mono-alkyl esters of long-chain fatty acids (C_{18} – C_{22}) synthesized from various renewable feedstocks, such as vegetable oils and animal fats. The common methyl esters are listed in Table 2.3.

Table 2.3 The list of FAMES and their structures.⁴²

Name	Structure
Methyl octanoate (C8 : 0)	$CH_3(CH_2)_6COOCH_3$
Methyl decanoate (C10 : 0)	$CH_3(CH_2)_8COOCH_3$
Methyl laurate (C12 : 0)	$CH_3(CH_2)_{10}COOCH_3$
Methyl myristate (C14 : 0)	$CH_3(CH_2)_{12}COOCH_3$
Methyl palmitate (C16 : 0)	$CH_3(CH_2)_{14}COOCH_3$
Methyl stearate (C18 : 0)	$CH_3(CH_2)_{16}COOCH_3$
Methyl oleate (C18 : 1)	$CH_3(CH_2)_7CH=CH(CH_2)_7COOCH_3$
Methyl linoleate (C18 : 2)	$CH_3(CH_2)_4CH=CHCH_2CH=CH(CH_2)_7COOCH_3$
Methyl linolenate (C18 : 3)	$CH_3CH_2CH=CHCH_2CH=CHCH_2CH=CH(CH_2)_7COOCH_3$
Methyl arachidate (C20 : 0)	$CH_3(CH_2)_{18}COOCH_3$
Methyl behenate (C22 : 0)	$CH_3(CH_2)_{20}COOCH_3$
Methyl erucate (C22 : 1)	$CH_3(CH_2)_7CH=CH(CH_2)_{11}COOCH_3$
Methyl ricinoleate (C18 : 1, OH)	$CH_3(CH_2)_5CH(OH)CH_2CH=CH(CH_2)_7COOCH_3$

This material is reserved for educational use only, not allowed for commercial use.

Forbidden to modify the content, and cite the document when use.

2.5) Linear long-chain α -olefin

Linear long-chain α -olefin or (LLAO) is a long-chain alkene with a chemical formula C_nH_{2n} . The linear long-chain consists of C_{10} - C_{30} carbon number with an unsaturated C=C at the primary or alpha-position, as shown in Figure 2.7.

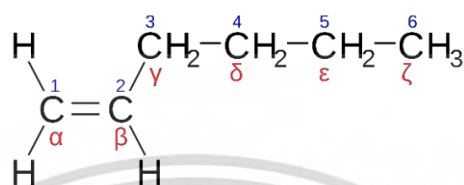


Figure 2.7 Chemical structure of Linear long-chain α -olefin.

Linear long-chain α -olefin is industrially manufactured by the oligomerization of ethylene (Figure 2.8) and Fisher-Tropsch synthesis. Another route for producing Linear long-chain α -olefin is dehydration of alcohols. However, this process is commercially used for a small scale in gas phase reaction.⁴⁴

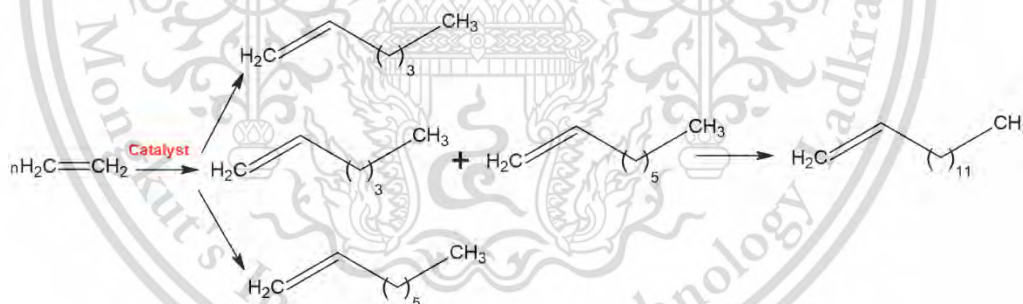


Figure 2.8 The oligomerization of ethylene to linear long-chain α -olefin.

The applications of linear long-chain α -olefin are depending on the length of carbon number (Figure 2.9). C_{10} - C_{14} linear α -olefins are used in making surfactants for aqueous detergent formulations. Moreover, C_{14} can be used as on-land drilling fluid basestock to replace the used of diesel or kerosene in that application. Although C_{14} is more expensive than middle distillates, it has a significant advantage for the environment, such as being much more biodegradable materials and less irritating to skin and less toxic. C_{16} - C_{18} linear olefins are primarily used in oil-soluble surfactants. This material is reserved for educational use only, not allowed for commercial use.

and lubricant. The C_{16} - C_{18} alpha or internal olefins are widely used as synthetic drilling fluid. The preferred materials for this application are linear internal olefins, which could produce by isomerization of linear α -olefins to an internal position. The higher internal olefins are recognized as a better lubricant. Another important application for C_{16} - C_{18} olefins is in paper sizing. Once again, Linear α -olefins are isomerized into linear internal olefins are then reacted with maleic anhydride to make an alkyl succinic anhydride (ASA), a popular paper sizing chemical. For C_{20} - C_{30} linear α -olefins, these compounds can be produced only 5-10% of the total production of a linear α -olefin plant production. They are used in a number of reactive and non-reactive applications, including as feedstocks to make heavy linear alkyl benzene (LAB) and low molecular weight polymers, which are used to enhance properties of waxes.

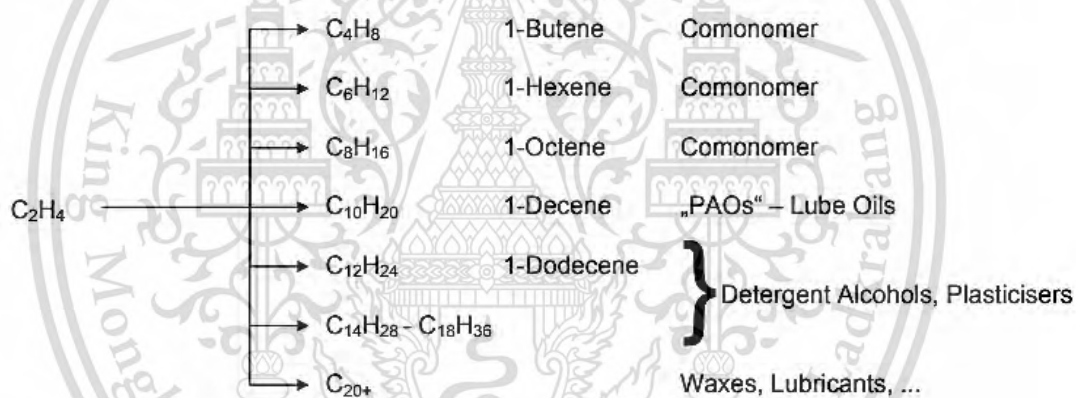


Figure 2.9 The application of linear alpha olefin in chemical industry.⁴⁵

2.6) Hydrodeoxygenation of FAMES

Deoxygenation is a reaction involving the removal of the oxygen in FAMES molecules to produce a hydrocarbon. There are three different types of the deoxygenation process, namely decarboxylation, decarbonylation and hydrogenation-dehydration. In general, FAMES molecules could be converted to fatty acid (carboxylic acid) via the hydrogenolysis at C-O bond with releasing of methane or hydrolysis with water (H_2O) and remove methanol as a by-product. This fatty acid could be deoxygenated to form hydrocarbon and produce carbon dioxide (CO_2) as a by-product

from decarboxylation. This process is generally taking place on the noble metal catalyst such as palladium (Pd)⁴⁶ and platinum (Pt).⁴⁷ Another parallel pathway is hydrogenation of fatty acid to aldehyde together with the removal of water. This aldehyde intermediate could be deoxygenated to hydrocarbon with the releasing of carbon monoxide (CO) by decarbonylation. This process is favorable on the non-noble metal catalysts such as nickel (Ni)¹⁶ and cobalt (Co)¹⁸ catalysts. The major disadvantage of these deoxygenation process is to sacrifice a carbon atom in the backbone, leading to an one shorter hydrocarbon.

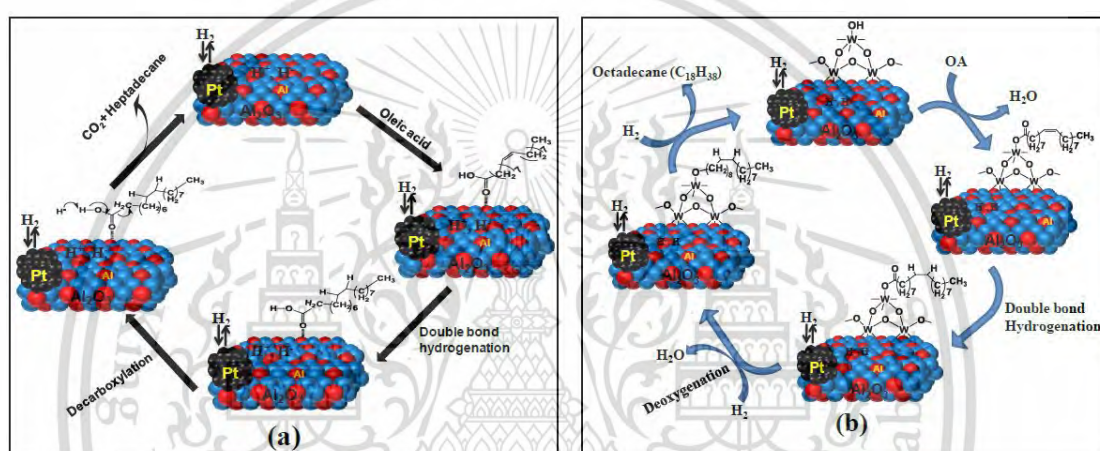


Figure 2.10 a) the decarboxylation and b) deoxygenation of fatty acids over Pt based catalyst.¹³

Hydrogenation-dehydration, on the other hand, can produce hydrocarbon molecule without the carbon loss. Aldehyde is an intermediate from hydrogenation of FAMES that can be readily hydrogenated to an alcohol. This alcohol can be dehydrated to α -olefin in the present of acid sites (*i.e.* Brønsted acid, (BAS)) and can further hydrogenated to a paraffin, respectively. Hence, the non-carbon loss hydrocarbon can be produced via this pathway. A preferred catalyst for this reaction is a bifunctional catalyst which contains a metallic phase and acid site. The synergistic effect between these active sites could be performed via the acid site, especially BAS, motivate the dehydration of an adsorbed alcohol, while a metallic phase facilitates the hydrogen dissociation and spillover.¹⁵ The summarized reaction pathway are shown in Figure 2.11.

This material is reserved for educational use only, not allowed for commercial use.

Forbidden to modify the content, and cite the document when use.

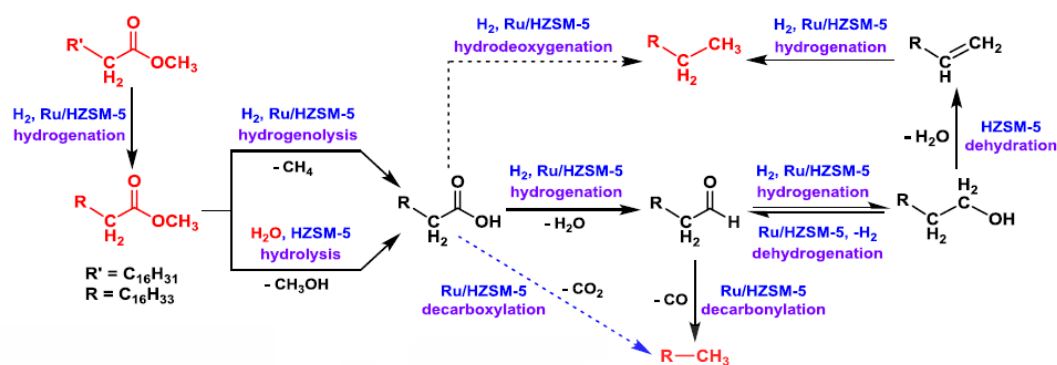


Figure 2.11 The summarizes deoxygenation pathway of FAMES.¹⁶

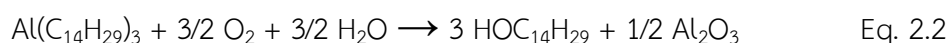
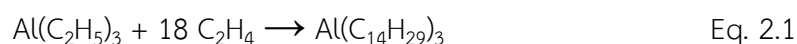
2.7) Fatty alcohols

Fatty alcohols or long-chain alcohols are straight-chain primary alcohols which contained range of carbon from 6 to 26 atoms (C_6 - C_{26} alcohol). They are also obtained in the formed of saturated and unsaturated molecules. The carbon chain length is depended on varieties with the sources. The molecule of fatty alcohol is shown in Figure 2.12.

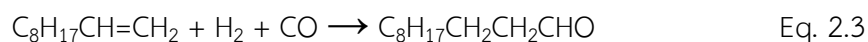


Figure 2.12 The example of fatty alcohol molecules

Industrially, fatty alcohols are produced from the oligomerization of ethylene (Ziegler process) using triethylaluminium (Eq 2.1) followed by oxidation in air (Eq 2.2).⁴⁸ This process can give even-numbered alcohol



In addition, a long-chain alkene mixture from the oligomerization of ethylene can be subjected to hydroformylation, forming odd-numbered long-chain alkene and subsequently hydrogenated to fatty alcohol as following equations;⁴⁹



However, the Ziegler process are produced from petrochemical resources, which are considered as a non-green chemistry. It could also produce more carbon dioxide (CO₂) to the atmosphere. Alternatively, fatty alcohols are also produced from FAMES derived from vegetable oils and fats via the hydrogenation process (Figure 2.13). These renewable resources could be obtained in several countries in South east Asia. The main sources of C₁₂-C₁₄ alcohols are coconut oils and palm kernel oils. C₁₆-C₁₈ alcohols are produced from tallow oils, soybean oils and palm oils; the C₂₂-C₂₆ alcohols are obtained from rapeseed oils and fish oils. In general, FAMES have gained more attention to use as a feedstock to produce fatty alcohols rather than free fatty acid (FFAs). This is because FAMES are much less corrosive and more stable than FFAs. Moreover, their preliminary fractionation could provide a narrow fraction of alcohols.⁵⁰

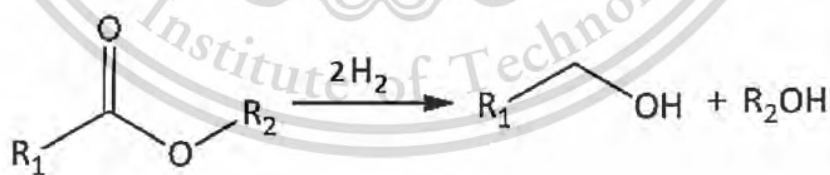


Figure 2.13 The hydrogenation of FAMES to fatty alcohols.

Fatty alcohols and their derivatives can be used in various home and personal care applications like creams, lotions, detergents, shampoos, and toothpastes. In addition, they are very widely used in agricultures, crude oil exploration, emulsion polymerization, paints and coatings, perfumery chemicals, pharmaceuticals, pulp and

This material is reserved for educational use only, not allowed for commercial use.

Forbidden to modify the content, and cite the document when use.

paper, lubricants, and in the preparation of textile auxiliaries. The fatty alcohol applications are shown in Figure 2.14.



Figure 2.14 Fatty alcohol applications.⁵¹

2.8) Hydrogenation of FAMES

Hydrogenation is a chemical reaction between hydrogen molecule (H_2) and another compound in the presence of metal catalysts, such as platinum (Pt), palladium (Pd), nickel (Ni) and copper (Cu). In general, the hydrogenation of FAMES is used to obtain fatty alcohols.⁵⁰ Fatty alcohols or long-chain alcohols are usually a straight chain primary alcohol, containing 4-6 atoms (C_4-C_6) to 22-26 atoms ($C_{22}-C_{26}$). There are several reactions occurring simultaneously during the hydrogenation of FAMES as shown in Figure 2.15. In term of unsaturated FAMES, the first step is hydrogenation of $C=C$ bond forming saturated compound (Eq. 2.5) or isomerization to *trans* $C=C$ bond (Eq. 2.6). The second step which obtained from both unsaturated and saturated FAMES is the hydrogenation at carboxyl group (*i.e.* ester), which leads to the formation of long-chain aldehyde as an intermediate with the loss of methanol (Eq. 2.7). After that, this intermediate could be further hydrogenated to fatty alcohol (Eq. 2.8). In addition, the formation of a long-chain hydrocarbon could be formed owing to the “over-hydrogenation” of fatty alcohol with the removal of water (Eq. 5).

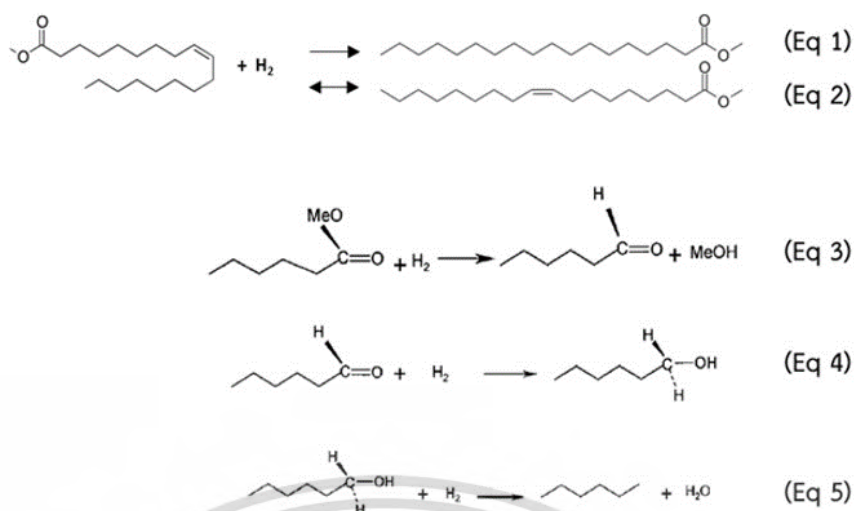


Figure 2.15 The general step of FAMEs hydrogenation.⁵²

Industrially, Cu-Cr based catalysts are used as a heterogenous catalyst to produce fatty alcohols, which typically required a harsh condition (250–350 °C and 10–20 MPa).⁵³ This process can be performed in a slurry reactor or a fixed bed reactor. Even though, these catalysts could provide a good selectivity in alcohols, they induce environmental risks, harsh reaction conditions, and high energy consumption. In addition, the deactivation of catalysts was observed. Therefore, continuously adding a small amount of fresh catalysts in the recycle stream and withdrawing spent catalysts are needed for a high conversion. According to these problems, considerable improvements in a catalyst performance are needed to improve the process in terms of the economic efficiency and environmental impact. There are two main problems that requires to solve (1) the achievement of high activity, selectivity, and stability of a catalyst under milder reaction conditions and (2) the elimination of environmental risks, which are associated with the use of chromium in the catalyst composition.

Nowadays, there many works have been done to develop the Cr-free catalysts. Especially, catalysts based on noble metal (Pt, Pd and Ru) and non-noble metal (Ni and Co). However, the undesired products from the loss carbon backbone of FAMEs, as well as, the over hydrogenation can be obtained. Pt and Pd catalysts tend to promote the decarboxylation due to the strong feed adsorption (η^2 -adsorption) on the catalyst surface. Moreover, the over hydrogenation of fatty alcohols can be observed due to the high performance of hydrogen dissociation and spillover of Pt and Pd catalysts. In similar manner, Ni and Co catalysts are favorable to decarbonylation of

This material is reserved for educational use only, not allowed for commercial use.

Forbidden to modify the content, and cite the document when use.

fatty aldehydes to one short chain olefin and further hydrogenated to a one short chain hydrocarbon, respectively. Since the single metal catalyst promotes the strong feed adsorption on the catalyst surface, the catalyst development by adding second metal have been studied. Pouilloux. *et al.* (1998) reported the use of RuSnB/Al₂O₃ catalysts for selective hydrogenation of FAMES to fatty alcohols. The incorporated Sn as a secondary metal could promote the η^1 -adsorption of C=O on their surface rather than η^2 -adsorption (Figure 2.16). This could indicate the synergetic effect between SnO and Ru metal which SnO act as an electrophilic site provide the η^1 -adsorption of C=O and the Ru facilitates the hydrogen dissociation and spillover. Although this noble metal catalyst showed the good performance to produce fatty alcohols, it still not available in term of the industrial usage due to the expensive cost.⁵⁴ Nowadays, Cu- based catalysts have gained more attention to substitute the use of noble and non-noble metals. This is because the Cu-based catalyst is cheaper than noble and non-noble metals. It could also facilitate the η^1 -adsorption of C=O on their surface rather than η^2 -adsorption. This weak adsorption could lead to the formation of fatty alcohols without the loss of CO₂ from the decarboxylation process. In addition, the over hydrogenation is lower pronounced than on the noble metal catalysts due to the lower hydrogen dissociation and spillover ability.²⁰

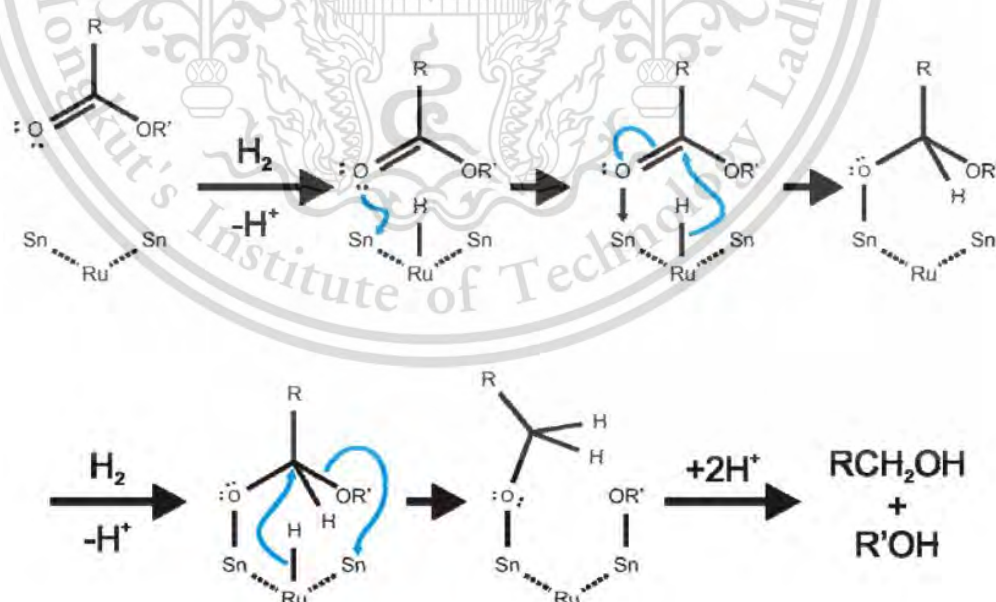


Figure 2.16 Mechanism of the direct hydrogenation of FAMES to fatty alcohol over RuSnB/Al₂O₃ catalyst.⁵⁴

2.9) Phyllosilicate

Phyllosilicate (PS) is a laminar-structured silicate mineral, which consists of a tetrahedral layer and an octahedral layer, as shown in Figure 2.17. For the tetrahedral layer, each central cation is bonded with 4 oxygen atoms and linked to neighboring tetrahedra by sharing 3 corners oxygen atoms, forming a tetrahedral sheet. In the octahedral layer, each octahedron consists of metal cations (Ni^{n+} , Cu^{n+} , Fe^{n+} , Co^{n+}) coordinated with 6 anions (O^{2-} , F^- , Cl^- , OH^-) and connects with adjacent octahedral sites by sharing edges. The free oxygen atoms on the tetrahedral sheet point in the same direction and connect with the octahedral sheet, forming a 1:1 phyllosilicate structure (Kaolinite) or the octahedral sheet is sandwiched between two tetrahedral sheets to form a 2:1 phyllosilicate structure (Smectite). The demonstration of phyllosilicate is shown in Figure 2.17.²⁸

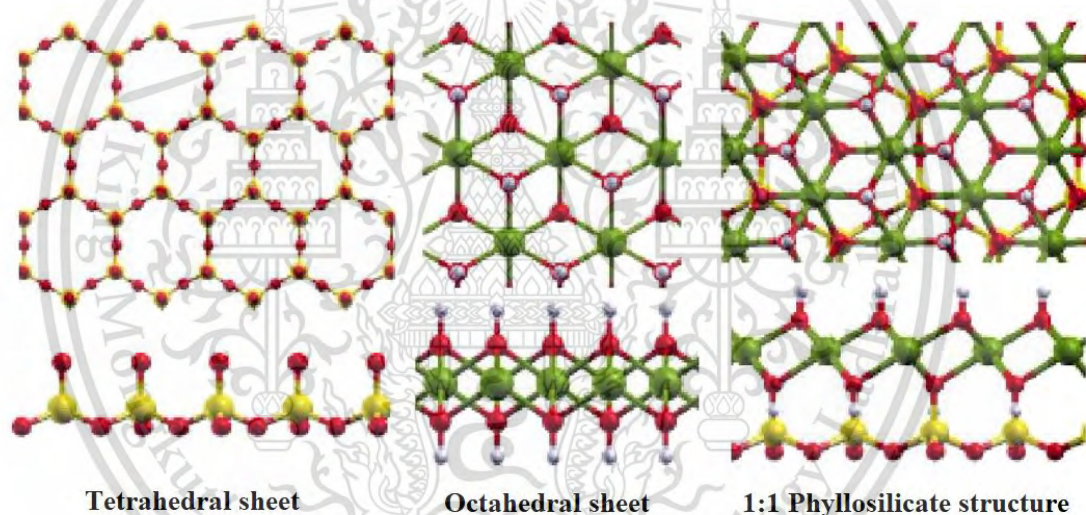


Figure 2.17 The formation of 1:1 phyllosilicate structure.²⁵

2.9.1) Synthesis of copper phyllosilicate (CuPS)

In the past 20 years, several methods for the preparation of CuPS have been developed, such as precipitation, deposition-precipitation, sol-gel method and ammonia evaporation and hydrothermal method (AHM). Among these techniques, the AHM method has gained more attention due to a more convenience to prepare and give a high yield.³⁰

CuPS could be prepared via the AHM technique by using tetraamine copper(II) complexes $[\text{Cu}(\text{NH}_3)_4(\text{H}_2\text{O})_2]^{2+}$ as a precursor and then deposited on the silica at room temperature. The preparation procedures consist of adding the appropriate ammonia

solution into the Cu^{2+} solution to form $[\text{Cu}(\text{NH}_3)_4(\text{H}_2\text{O})_2]^{2+}$. This step will provide a highly dispersion Cu^{2+} in the solution. After that, the solution was well mixed with colloidal silica overnight. In this step, the silica precursor in the basic environment will provide a silicate anion which facilitate the deposition of $[\text{Cu}(\text{NH}_3)_4(\text{H}_2\text{O})_2]^{2+}$ on its surface. The formation of CuPS are obtained after the copper evaporation of ammonia at the temperature 80-90 °C until neutralized. The gradually removal of ammonia will provide the formation of neutral Cu^{2+} complex $[\text{Cu}(\text{OH})_2(\text{H}_2\text{O})_2]^{2+}$ and then condensation to form precipitation of CuPS at the pH = 7. The hydrothermal technique is used to increase the crystallinity of CuPS. The CuPS slurry was transferred to autoclave and hydrothermal at 150 °C for 24 h. Finally, the product is washed, dried and calcined at 400 °C. The preparation of CuPS is summarized in Figure 2.18.

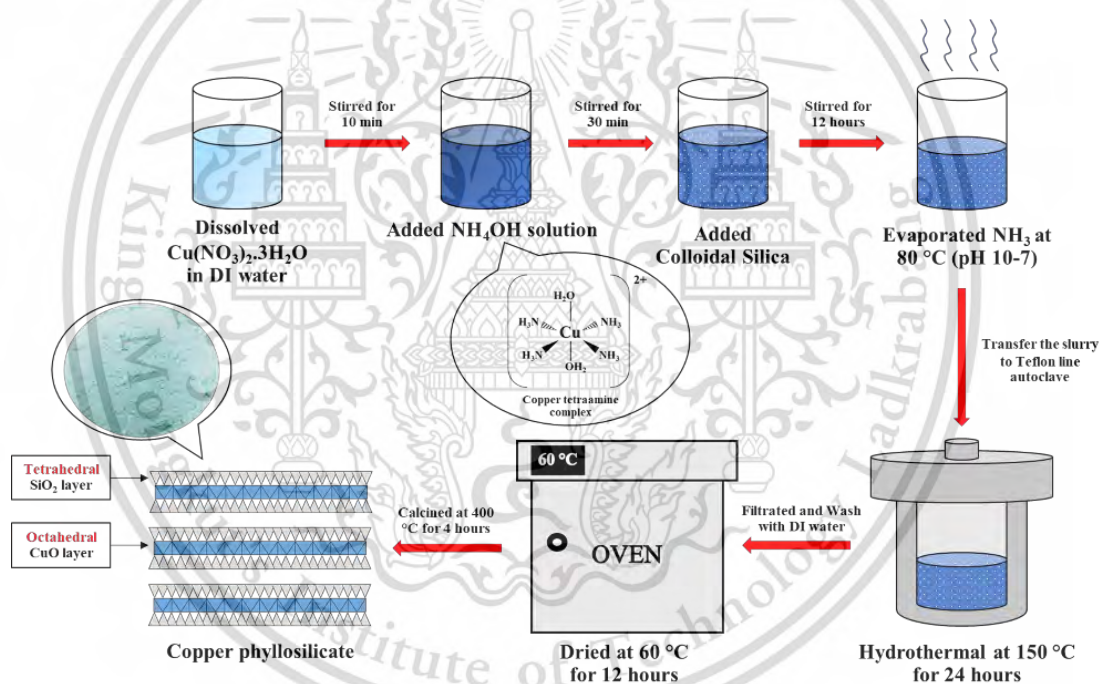


Figure 2.18 The preparation of CuPS by AHM.²⁶

2.9.2) Characterization of copper phyllosilicate (CuPS)

In general, several characterization techniques are performed to investigate the properties and characteristic of CuPS, such as crystal and textural structure, reducibility, surface acidity and electronic properties.

2.9.2.1) Crystal and textural structure

X-ray diffraction spectroscopy (XRD) is a technique to identify crystal structure of inorganic materials by indexing the peaks into standard database. It could also further calculate the unit parameters and get more information on the crystal structure. The investigation of crystal structure by XRD is a very important for the CuPS. CuPS also known as “Chrysocolla” with formula $\text{Cu}_2\text{Si}_2\text{O}_5\text{OH}$, which could be obtained on earth as a hydrated copper phyllosilicate mineral. The comparison between the prepared CuPS and standard chrysocolla peak can identify the complete or incomplete formation of CuPS after preparation. The complete formation of CuPS would provide a board peak at 30.8° , 35.0° , 57.5° and 62.4° , corresponding with the characteristic chrysocolla structure without the presence of CuO phase.²⁹

For the textural properties, N_2 isothermal adsorption-desorption gives an information on surface area, pore size and pore volume. CuPS usually shows high surface area due to the lamellar structure.²⁹ Moreover, TEM is carried out to investigate the morphology of lamellar structure and also Cu metallic particles distribution after the reduction.

2.9.2.2) Reducibility

H_2 temperature programmed reduction (H_2 -TPR) is widely used to characterize the reducibility of supported metal catalysts. This technique provides the information on the reducibility of the metal oxides and the interaction between the metal oxide and support. The testing procedure for H_2 -TPR is as following: the sample is first degassed to remove the surficial gas species and then the reduced gas (hydrogen diluted in argon) is introduced as the temperature increasing. The peak position indicates the reducibility, while shape and area of H_2 -TPR profile provide the metal oxide particles size and the amount of H_2 consumption. For CuPS, the reduction temperature is usually lower than bulk CuO particles ($< 300^\circ$) and the shape of H_2 -TPR profile is more narrow than bulk CuO. This is because the highly dispersed Cu due to the formation of well-defined Cu^{2+} species in octahedral layer on CuPS as a precursor.²²

2.9.2.3) Electronic properties

X-ray photoelectron spectroscopy (XPS) is a very important surface spectrum technique, which is could investigate elemental composition and electronic properties of the material.²⁷ In the case of CuPS, this technique could clarify the interaction

This material is reserved for educational use only, not allowed for commercial use.

Forbidden to modify the content, and cite the document when use.

between the Cu^{2+} and Si^{4+} in the calcined CuPS. When comparing the binding energy between Cu 2p in the CuPS and CuO supported on SiO_2 (CuO/SiO_2), the binding energy of Cu^{2+} in CuPS is shifted to the higher energy than bulk CuO and also the binding energy of Si 2p on CuPS is lower than CuO/SiO_2 . This could indicate the strong interaction between Cu and SiO_2 on CuPS.

2.9.2.4) The transformation of CuPS in the reduction step.

The active sites for hydrogenation and hydrodeoxygenation are a metallic Cu instead of Cu^{2+} species in CuPS structure. In this case, CuPS is just a catalyst precursor which could convert to highly dispersed metallic Cu particles after the reduction. Hence, the investigation of structure transformation on CuPS is important. In general, the formation of metallic with partially reduced Cu^+ species are usually obtained by the XPS technique.²⁷ However, it not capable to investigate the transformation of Cu^{2+} species during the reduction since most of their experiment take placed in the *ex-situ* system. X-ray adsorption spectroscopy (XAS) is a widely used technique for determining the local geometric and/or electronic structure of materials. The experiment is usually performed at the synchrotron radiation facilities, which provide intense and tunable X-ray beams. In case of CuPS, the transformation of the CuPS structure upon the reduction can be investigated by the *in situ* XANEs experiments. It could also identify the Cu species during the reduction process from linear combination fitting (LCF) using the fitting between shape of the spectra or edge energy.⁵⁵

2.9.2.5) Surface acidity

The investigation of acidity of the catalyst surface is generally performed by the NH_3 temperature program desorption (NH_3 -TPD). This technique could identify the weak, medium and strong acid sites on the catalyst surface.³¹ In addition, the type of acid sites could also study by the pyridine-adsorbed infrared spectroscopy (Py-IR) technique. In case of CuPS, this technique is useful to clarify the Cu^+ species which act as Lewis acid site (LAS). Moreover, some of Brønsted acids (BAS) might be observed since silanol at the catalyst surface could be produced after the reduction.³¹

2.9.3) Catalytic hydrogenation of esters on CuPS catalysts

CuPS is widely used as a catalyst precursor for the hydrogenation of esters. This is because CuPS after the reduction, could provide both of metallic Cu (Cu^0) and

This material is reserved for educational use only, not allowed for commercial use.

partially reduced Cu^+ species. Many studies claimed that the synergistic effect between these active species (Cu^+/Cu^0) could promote the reduction of the carbonyl group.⁵⁶ The Cu^+ species act as an electrophilic site to polarize a carbonyl group, while the Cu^0 facilitates the hydrogen dissociation and spillover to the feed (Figure 2.19). Therefore, the composition between Cu^0 and Cu^+ species would play a crucial role for the catalytic conversion as well as selectivity of the desired hydrogenation product.

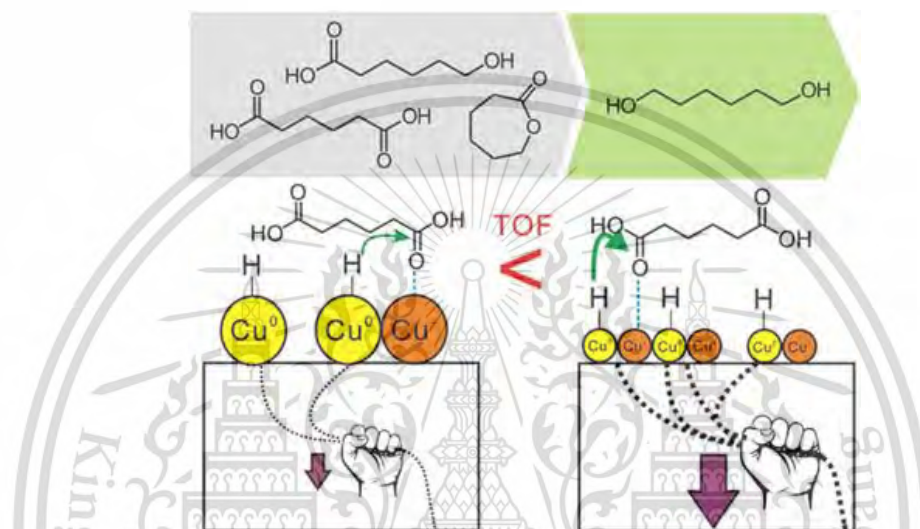


Figure 2.19 The synergistic effect between Cu^0 and Cu^+ of CuPS catalyst on the hydrogenation.²²

The hydrogenation of esters, for example, dimethyl oxalate (DMO) and diethyl oxalate (DEO), could produce methyl glycolate (MG), ethylene glycol (EG) and ethanol (EtOH). The catalytic reaction pathway is a series reaction, as shown in Figure 2.20. Among these products, EG is the most favorable product because of its essential application as an antifreeze and a coolant. To obtain a high yield of EG, the appropriate of Cu^+/Cu^0 ratio needs to be optimized. Sun. *et al.* (2018) founded a strong dependence of DMO hydrogenation performance and the Cu^+/Cu^0 ratio by controlling the reduction temperature of CuPS catalysts. At a reduction temperature of 250 °C, the $\text{Cu}^+ / (\text{Cu}^+ + \text{Cu}^0)$ ratio was 0.4, indicating the amounts of Cu^+ and Cu^0 were similar. The CuPS reduced at 250 °C showed the highest hydrogenation activity of DMO to EG with a complete 100% conversion and 95.2% of EG selectivity at 180 °C for a 16 h. The selectivity of EG from DMO hydrogenation can be obtained by controlled reduction temperatures.⁵⁷

This material is reserved for educational use only, not allowed for commercial use.

Forbidden to modify the content, and cite the document when use.

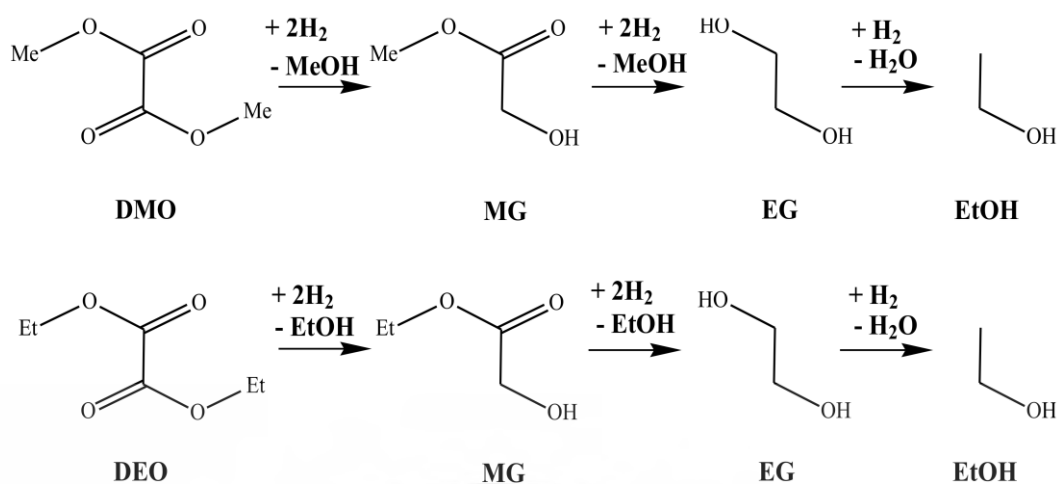


Figure 2.20 Reaction pathway of the hydrogenation of esters (DMO and DEO) to MG, EG, and EtOH.⁵⁷

On the contrary, to obtain a high yield of MG, a partial inhibition of DMO hydrogenation using CuPS was proposed.⁵⁸ Since Cu^0 promote hydrogenation activity, suppressing Cu^0 concentration should improve the selectivity of MG. Thus, increasing the Cu^+ concentration of CuPS would be a key to produce more yield of MG. Huang *et al.* (2020) reported the modification of CuPS by impregnated sodium silicate into CuPS powder prepared by AE method. This concept use to increase the interaction between Cu and SiO_2 via the formation of Si-O-Cu bonds, to limit surface concentration of Cu^0 . As expected, the reducibility of Cu^{2+} cations were decreased with additional sodium silicate. In addition, the surface area of Cu^0 decreased along with the increase in Cu^+ surface area (the ratio of $\text{Cu}^0/\text{Cu}^+ = 0.50\text{--}0.54$). The selectivity of MG increased from 0.8 to, approximately, 100% at 84% of DMO conversion by doping 0.5 wt % of sodium silicate. This could highlight the strong correlation between desired products and surface Cu species.

In order to increase EtOH yield form DMO hydrogenation, a high dispersion of metallic Cu is the key to promote a further hydrogenation of EG. Ai *et al.* (2018) reported the introducing of Ce to CuPS, the dispersion and electron density of copper could be enhanced.⁵⁹ This modified CuPS catalyst can produce 92% of EtOH within 200 h. In addition, the large amount of H_2 ($\text{H}_2/\text{DMO} = 200$) and higher reaction temperature (280 °C) are required to further hydrogenate EG to EtOH. Hydrogen concentration could be enhanced from the feed-in stream or from an increase in local

partial pressure. Moreover, the longer contact time of reactants and catalytic promotes the EtOH selectivity.

2.10) Potassium doping on Cu catalysts

Potassium (K) is one of the alkali metals which have a single valence electron in the outer electron shell. This valence electron is easily removed to create an ion with a positive charge (+ cation) that could combine with anions to form salts. In general, potassium salts such as KNO_3 , K_2CO_3 , are wide used as a potassium precursor to doped on catalysts. After doping with the precursor and then calcination, it could form potassium oxide (K_2O) due to the thermal decomposition. K_2O is an ionic compound having an antifluorite structure. In their crystals, the positions of the anions and cations are reversed relative to their positions in CaF_2 , with potassium ions coordinated to 4 oxide ions and oxide ions coordinated to 8 potassium (Figure 2.21).⁶⁰ K_2O is a basic oxide and reacts with water to produce the potassium hydroxide.

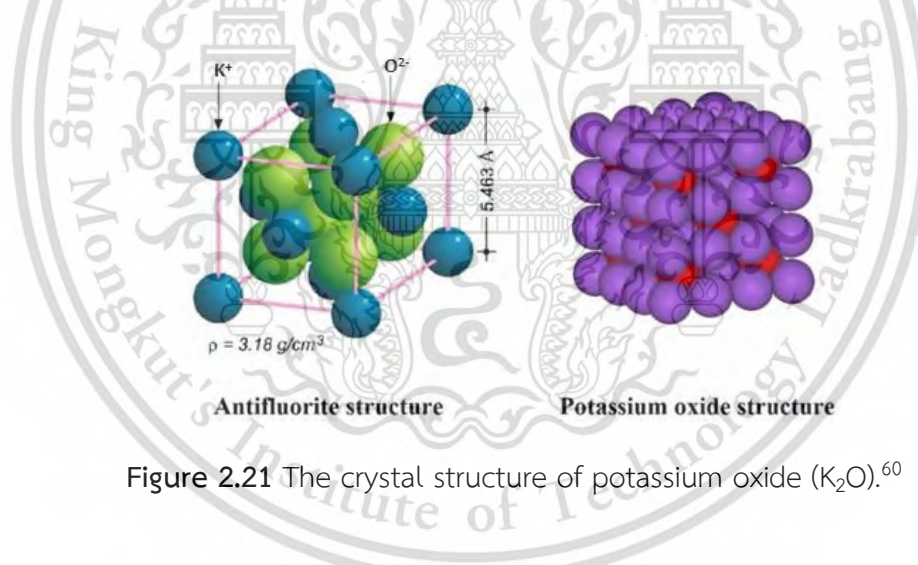


Figure 2.21 The crystal structure of potassium oxide (K_2O).⁶⁰

Nowadays, K doping on Cu catalysts has been studied. Hu. *et al.* (2018) reported the use of K-doped on $\text{Cu}/\text{Al}_2\text{O}_3$ catalyst for hydrogenation of 5-hydroxymethylfurfural (HMF) to 2,5-bis(hydroxymethyl)furan (BHMF). The incipient wetness impregnation method was applied to prepare the catalysts. After the addition of 0.5 - 5.0 wt.% of K on $\text{Cu}/\text{Al}_2\text{O}_3$, the strong acid site evaluated from NH_3 -TPD were significantly decreased with the increase of the K content. This suggested that K could neutralize strong acid due to their basic properties. In a supportive manner, the basic site was increased with the increase of the K content. The interaction between K and Cu could also

evidence by the H₂-TPR, in which the reduction temperature of 5.0 wt.% K on Cu/Al₂O₃ were shifted to a higher temperature (Figure 2.22). In addition, the appropriate amount of K content could provide the highly dispersed of Cu metallic particle.³⁴

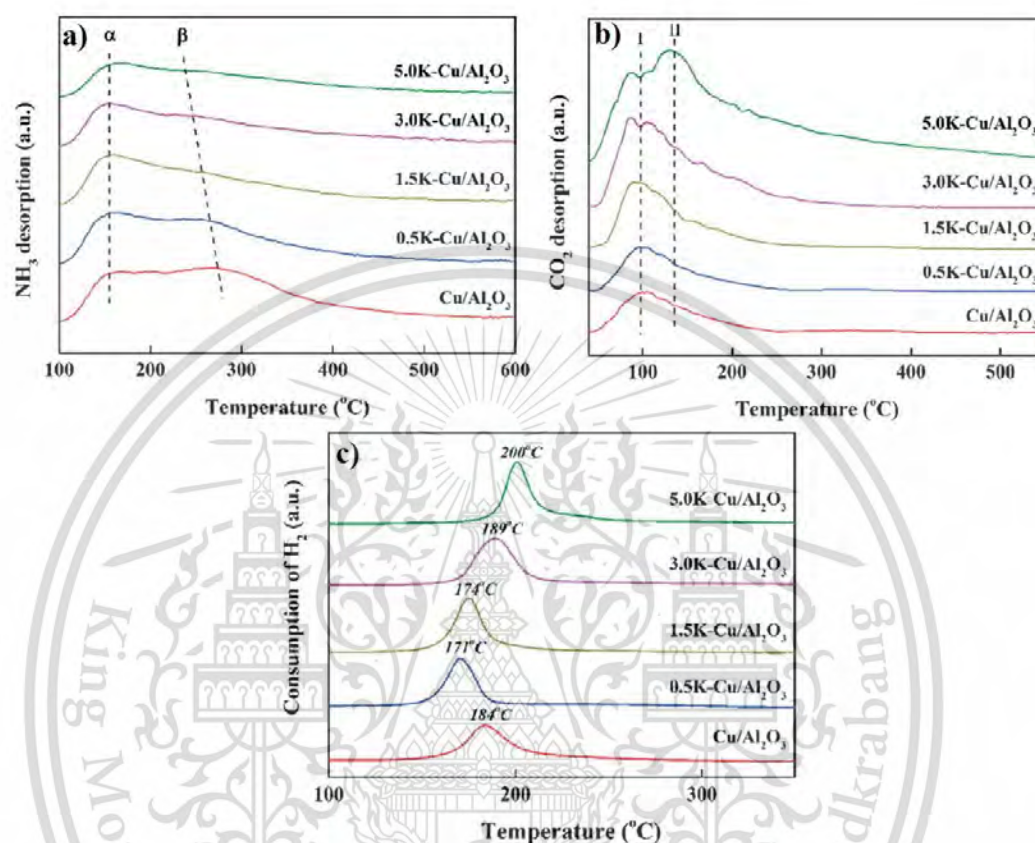


Figure 2.22 The effect of K doping on a) acidity b) basicity and c) reducibility.³⁴

Li. *et al.* (2022) studied the effect of different alkali metal, including Li, Na, K and Cs doping on CuMgCe catalysts for the *iso*-butanol synthesis from syn gas. The addition of these alkali metals also affects on the acid-base properties of the catalyst, leading to the increased the strength and density of basic sites. The order of alkalinity strength was Cs>K>Na>Li. Among these alkali metal, the doping of K could provide the highest catalytic performance as well as the *iso*-butanol selectivity. In addition, the using of K is cheap and easy to obtain, which is conducive to industrialization.³³

2.11) Literature reviews

Biodiesel or FAMEs has gained more attention to substitute the use of petroleum fuels to produce intermediate chemicals.³⁹⁻⁴⁰ In general, FAMEs could be produced by transesterification of vegetable oils with methanol using basic catalysts.⁴¹⁻⁴² In Thailand, most of FAMEs are produced from palm oils which are represented almost 80% of the crop production in the market. Methyl palmitate, a saturated methyl ester, is mostly obtained from transesterification of palm oils, approximately 45%.⁴³ This compound could be converted to various intermediate chemicals, such as fatty aldehydes, fatty alcohols, long-chain α -olefins and long-chain hydrocarbon. Fatty aldehydes and fatty alcohols could obtain via the hydrogenation, while long-chain α -olefins and long-chain hydrocarbons could product via hydrodeoxygenation of FAMEs. Among these products, linear long-chain α -olefins and fatty alcohols would be more valuable than others due to their widely applications in many industries. Linear long-chain α -olefins has been used as a lubricant and surfactant.⁴⁵ Also, fatty alcohols widely used in cosmetic and pharmaceutical industries.⁵¹ Therefore, in order to obtain a higher yield of these product, the catalyst design and suitable catalytic reaction need to be optimized.

Typically, the hydrodeoxygenation of FAMEs to linear long-chain α -olefins could be proceed via the decarbonylation¹³⁻¹⁴ and hydrogenation-dehydration.¹⁵ The decarbonylation yields one short linear long-chain α -olefins with CO, over noble metal and non-noble metal catalysts. Snåre. *et al.* (2006) reported the deoxygenation of steric acid over 5%Pt/Al₂O₃ catalyst. The catalytic reaction was carried out in semi-batch reactor at 300 °C under 6 bar of He pressure. This Pt-based catalyst could produce 17% of heptadecene and 19% of heptadecane selectivity at 20 of steric acid conversion. This suggested that the Pt catalyst promoted the decarbonylation forming an one short linear long-chain α -olefins product. Moreover, this olefin could be hydrogenated to a long-chain hydrocarbons due to the ready hydrogen dissociation ability of Pt catalysts.¹⁷ Janampelli. *et al.* (2017) also studied the deoxygenation of oleic acid derived from palm oils using Pt supported on Al₂O₃ catalysts and modified with WO_x. The catalytic reactions were carried out in a batch reactor from 260 to 320 °C with 1-20 bar of H₂ pressure. The result showed that the 2Pt-12WO_x/Al₂O₃ catalyst could get 100% conversion and yielded only long-chain hydrocarbon (67% of

octadecane and 31% of heptadecane) without long-chain olefin. This again could be attributed to a high decarbonylation with the ready hydrogen dissociation ability of this noble metal catalysts. Therefore, the olefin formed can be subsequently hydrogenated to paraffin at 100% conversion.⁴⁷ Not only the decarbonylation reaction but the decarboxylation yielding a long-chain hydrocarbon with the loss of CO₂ also could be obtained on noble metal catalysts. Han. *et al.* (2010) reported the use of Pd catalysts for the aliphatic ester conversion over several supports (SrSO₄, BaCO₃, CaCO₃, BaSO₄ and C support). The catalytic reactions were carried out in batch reactor at 270 °C to 300 °C with the H₂ pressure 1.0 to 2.2 MPa. The result showed that Pd/BaSO₄ catalysts provided almost 100% of the methyl stearate conversion. However, only pentadecane (C₁₇) was obtained with 98% selectivity. This could suggest that the Pd-based catalyst more facilitated the decarboxylation producing an one carbon loss hydrocarbon product rather than the decarbonylation to produce a long-chain olefin.⁴⁶

In term of non-noble metal catalysts, such as Ni and Co, these catalysts can provide the decarbonylation product similar to noble metal. Snåre. *et al.* (2006) reported the deoxygenation of steric acid over Ni supported on silica catalysts (60%Ni/SiO₂). The catalytic reaction was carried out in semi-batch reactor at 300 °C under 6 bar of He pressure. The Ni catalyst produced 30% of heptadecene and 19% of heptadecane selectivity even at low conversion (~18%).¹⁷ In a similar manner, Yan. *et al.* (2013) reported the use of Ni phyllosilicate-based catalysts (Ni@PSi) for the deoxygenation of methyl palmitate. The reactions were carried out in batch reactor at 240 °C under 3MPa of H₂ pressure. Even though the Ni@PSi showed a high catalytic conversion (83.3%), the high yield of C₁₅ hydrocarbon (54.7%) was still obtained as a major product. This process suffers two-carbon loss (the methyl and the carbonyl groups), bearing a hydrocarbon with one carbon shorter than the parent FAMES backbone.¹⁶ Krishnapriya. *et al.* (2012) also studied methyl oleate conversion using Co supported on SiO₂-Al₂O₃ catalysts. The deoxygenation of methyl oleate was carried out in batch reactor 280 °C under 15 bar of H₂ pressure. They found that 6 wt.% Co on SiO₂-Al₂O₃ could provide 100 % methyl oleate conversion with 50% pentadecane/octadecane. These products could proceed via the parallel reaction pathway, including decarboxylation and hydrodeoxygenation, respectively. Although, the latter could produce no carbon loss product (octadecane), the trace amount of linear long-chain α -olefins (octadecene) could be obtained. This could indicate that

This material is reserved for educational use only, not allowed for commercial use.

the Co catalysts still promoted over hydrogenation of linear long-chain α -olefins at high conversion.¹⁸ Phichitsurathaworn. *et al.* (2020) reported Co-based catalysts over silica support to produce olefin from heptanoic acid (C_7) as a feed model. The reaction was taking place in a continuous fixed-bed reactor at 400 °C under atmospheric pressure of H_2 . The catalytic result showed that the 5%Co/SiO₂ catalyst could provide 84.7% conversion and yielded C_6 olefin (46.4%) with 19.1% of cracking product (C_1 - C_5). This again could be attributed to the decarbonylation over non-noble metal catalysts. Moreover, the deactivation activity after 6 h of time on stream on this Co based catalyst could be observed.¹⁹

Hydrogenation-dehydration, on the other hand, could provide the linear long-chain α -olefins without a carbon loss over a bifunctional catalysts. In this reaction, FAMES would be selectively hydrogenated at C=O to alcohol (C-OH) intermediate that could be subsequently dehydrated to α -olefins. Li. *et al.* (2019) reported the N-doped Fe-based catalysts over carbon-Al₂O₃ support for hydrodeoxygenation of steric acid. The reaction was carried out in batch reactor at 320 °C under 4 MPa of H_2 pressure. The most efficient catalyst (Fe-N-C@Al₂O₃-900) could provide the chemoselective of hydrodeoxygenation, which produced 98% conversion and yielded >90% of C_{18} hydrocarbon as a major product. They proposed that the reaction pathway would proceed via the hydrogenation to a fatty alcohol and dehydrated to an olefin due to the present of acid site on the Al₂O₃ support. Then, the olefin product was subsequently hydrogenated to a long-chain hydrocarbon without the carbon loss product.¹⁵ However, using this metal based catalysts still provide an over hydrogenation to paraffins. Therefore, to produce a higher yield of olefins with lower paraffinic hydrocarbons, the suitable metal catalysts and reactions condition need to be operated.

A preferred bifunctional catalyst for the hydrogenation-dehydration shall consist of a chemoselective metal for the C=O hydrogenation and a weak acid for the alcohol dehydration. Typically, Cu-based catalysts interact with FAMES via η^1 -adsorption of C=O, providing selective hydrogenation of ester to alcohol without the decarbonylation.²⁰ Pestman. *et al.* (1997) reported the selective hydrogenation of acetic acid to aldehyde using several metal oxide precursors. They suggested that the selective C=O hydrogenation could be obtained from Cu catalysts by the synergistic

effect of Cu^+/Cu^0 species in the partially reduced CuO catalysts, where Cu^+ species is responsible for η^1 -adsorption of $\text{C}=\text{O}$, and Cu^0 species is active for $\text{C}=\text{O}$ hydrogenation.²¹ However, maintaining both Cu^+ and Cu^0 species in the catalysts with a high Cu dispersion is challenging because of the poor interaction between Cu and the support. Furthermore, the Cu agglomerate and/or sintering would be readily at above 10wt.% Cu loading. Zhang. *et al.* (2017) reported the preparation of Cu over several support including ZrO_2 , Al_2O_3 and MgO for the hydrogenation of lauric acid to lauryl alcohol using methanol as a hydrogen source. The catalysts were prepared via the co-precipitation method with the Cu loading of 20 wt.%. The reaction was carried out in micro batch reactor at 330 °C. Although $\text{Cu}/\text{Al}_2\text{O}_3$ showed a high alcohol selectivity (98%), the Cu dispersion was relatively low (10 nm). Moreover, the partial reduced Cu^+ could not be formed by this preparation method.²⁶

Recently, the copper catalysts derived from copper phyllosilicate (CuPS) precursor have been reported to provide a high Cu dispersion (even at >20wt.% Cu loading) with the presence of both Cu^+ and Cu^0 species after the reduction. This is due to a strong interaction between Cu^{2+} and SiO_2 in the well-defined lamellar structure. Gong. *et al.* (2012) reported the preparation of copper phyllosilicate by the ammonia evaporation and hydrothermal method (AEH) for the synthesis of ethanol by syngas. The preparation procedures consist the forming of tetraamine copper(II) complex ($[\text{Cu}(\text{NH}_3)_4(\text{H}_2\text{O})_2]^{2+}$) after added with ammonia solution into copper nitrate solution. After that the solution was well mixed with colloidal silica overnight. The formation of CuPS would be obtained after the evaporation of ammonia at 80 °C to pH 7. To increase the crystallinity of CuPS, the slurry was transferred to autoclave and hydrothermal at 150 °C for 24 h. Finally, the product was washed, dried and calcined at 400 °C. The CuPS were used as a catalyst precursor for the synthesis of ethanol via syngas. The characterization showed that after the reduction CuPS could provide the partially reduced Cu^+ species with Cu metal active species ($\text{Cu}^0/(\text{Cu}^0+\text{Cu}^+)$). This could be attributed to a strong interaction between Cu^{2+} and SiO_2 in the well-defined lamellar structure. The appropriate amount of $\text{Cu}^0/(\text{Cu}^0+\text{Cu}^+)$ at 0.35 with 20 wt.% of Cu loading could provide highest TOF (18 h^{-1}) of the reaction.²⁷ Jiang. *et al.* (2018) also prepared CuPS by AEH method for the hydrogenation of adipic acid to 1,6-hexanediol. The reaction was carried out in batch reactor at 240 °C with 90 bars of H_2 pressure.

The characterization showed that, after CuPS reduction could provide very fine Cu

This material is reserved for educational use only, not allowed for commercial use.

particles size (<5 nm) together with the formation of partial Cu^+ species. They also proposed that the synergetic effect between Cu^+ and Cu^0 species could promote the hydrogenation activity which Cu^+ acts as an electrophilic site to polarize the $\text{C}=\text{O}$ bond, while Cu^0 dissociates H_2 to form adsorbed hydrides for the subsequent hydride insertion. The best catalysts would be 30 wt.% of Cu on CuPS which could provide highest activity at 88.3% conversion and 87.2% 1,6-hexanediol selectivity within 3 h.⁵⁷

Apart from Lewis acid sites (LAS) provided by Cu^+ species, the chrysocolla structure of CuPS could offer additional Brønsted acid sites (BAS) from surface silanol groups. Che. *et al.* (2011) mentioned that the condensation of $\text{Si-O-M}^{2+}\text{-OH}$ species in the octahedral layer of phyllosilicate structure during the calcination yielded MO_x clusters and Si-OH .³² Tsou. *et al.* (2020) also mentioned the formation of BAS on the 30 wt.% CuPS catalyst after reduction at 240 °C (CuPS-R₂₄₀) and 350 °C (CuPS-R₃₅₀). The result showed that CuPS-R₂₄₀ could provide a higher BAS (3.1 $\mu\text{mol/g}$) than the CuPS-R₃₅₀. In addition, CuPS-R₂₄₀ also gives a higher Cu surface area (116.7 m^2/g) than CuPS-R₃₅₀ (66.9 m^2/g). Accordingly, this could suggest that the BAS might be generated at the perimeter of Cu particles since the amount of BAS depends on the Cu dispersion. Such generated silanols, especially those on the perimeter of metal particles after reduction, could have a stronger BAS acidity than that of the typical silanol.³¹ Even though no catalytic activity of these BAS has been revealed, these sites shall promote the dehydration of alcohols to α -olefins over the CuPS. Moreover, the high selectivity of α -olefins could be obtained since Cu is less active towards the olefin hydrogenation.

In sharp contrast, the catalysts to promote fatty alcohols from hydrogenation of FAMEs need to have only minimal BAS. In other words, they should only catalyzed hydrogenation without the further dehydration of the produced fatty alcohols. Accordingly, the BAS of CuPS could be reduced by adding the secondary basic metal, such as Li, Na, K, and Cs. In general, alkaline metals have been used as basic doped to neutralize the acid site on the catalyst. Li. *et al.* (2022) reported the effect of alkali metal (Li, Na, K, Cs) doping on the CuMgCe catalysts for *iso*-butanol synthesis from syngas. The reactions were carried out in the batch reactor at 300 °C with 5.0 MPa of 10% H_2/N_2 pressure. Among these alkali metals, they found that potassium (K) provided the highest conversion (64%) and *iso*-butanol selectivity (14%). This could due to the reducing of the acidity on catalyst surface promoting the aldol condensation of lower

alcohol to higher alcohol. Moreover, the lower hydrocarbon yields could be obtained due to the lower dehydration ability of the alcohol product. They also suggested the advantages on K doping i) a better electron-donating effect to transfer charges to the active phase of the catalyst, ii) highly efficient to neutralize the acid sites on the catalyst surface, iii) K is cheap and easy to obtain, which is favorable to industrialization.¹³ In addition, Hu. *et al.* (2018) also reported the effect of K content on Cu/Al₂O₃ catalysts for hydrogenation of 5-hydroxymethylfurfural (HMF) to 2,5-bis(hydroxymethyl)furan (BHMF). The reactions were carried out in the continuous fixed-bed reactor at 120°C and 2.0 MPa of H₂ pressure. They found that the K doped on Cu/Al₂O₃ catalyst could prevent the dehydration ability of -OH group providing the higher selectivity of BHMF. Moreover, the appropriate amount of K loading at 1.5 wt.% (1.5K-Cu/Al₂O₃) could facilitate Cu dispersion (60.5%) and reduced acidity (0.47 mmol/g) leading to the increase in the catalytic performance (99.2 % of conversion and 99.7 % on BHMF selectivity).³³ Therefore, the doping of K on CuPS catalysts would be a promising technique to modify the acidity of CuPS-based catalysts and would play a crucial role for the production of fatty alcohols from FAMES.

Chapter 3

Research methodology

3.1 Chemicals and materials

The details of the chemicals and substrates used in this research are shown in Table 3.1.

Table 3.1 List of chemicals.

Chemicals	Formula	Grade/Purity	Supplier
Copper(II) nitrate trihydrate	$\text{Cu}(\text{NO}_3)_2 \cdot 3\text{H}_2\text{O}$	99.50%	CARLO ERBA
Potassium nitrate	KNO_3	99.00%	CARLO ERBA
LUDOX® AS-40 colloidal silica	SiO_2	40.0%	SIGMA-ALDRICH
Silica gel (Davisil Grade 646)	SiO_2	99.00%	SIGMA-ALDRICH
Ammonia solution	NH_4OH	30.0%	CARLO ERBA
Methyl palmitate	$\text{C}_{17}\text{H}_{34}\text{O}_2$	97.00%	SIGMA-ALDRICH
<i>n</i> -dodecanes	$\text{C}_{12}\text{H}_{26}$	99.00%	ACROS ORGANICS
<i>n</i> -octane	C_8H_{18}	99.00%	CARLO ERBA
<i>n</i> -heptane	C_7H_{16}	99.00%	CARLO ERBA
Deionized water	H_2O	-	-
Air zero gas	Air	99.99%	UIG
Hydrogen gas	H_2	99.99%	UIG
Nitrogen gas	N_2	99.99%	UIG
Nitrous oxide gas	N_2O	99.99%	LINDE
Ammonia in helium	1% NH_3 , He	99.99%	LINDE
10% Hydrogen in Argon	10% H_2 , Ar	99.99%	UIG
1 % Hydrogen in Argon	10% H_2 , Ar	99.99%	UIG

3.2 Instrument and apparatus

1. Laboratory glassware
2. Pipette and red bulb
3. Protector laboratory hood, Science Technology
4. Mass flow controller, BROOKS INSTRUMENT LLC,
5. Sieve, AASHO N-92, U.S.A standard sieve
6. Glass wool
7. Glass tube
8. Universal Indicator
9. Hotplate
10. Hot air oven, UMS00, Memmert
11. Tube furnace with a programmed temperature controller, VCTF4, Vecstar
12. Digital Round-Top Stirring Hot Plate, 3810001, IKA
13. Thermal conductivity detector (TCD), VICI, Valco instrument)
14. Gas chromatography, 7890B, Agilent, USA with MXT-1 column
15. Autoclave

3.3 Catalysts preparation

3.3.1 Copper phyllosilicate catalyst (CuPS)

Copper phyllosilicates (CuPS) were prepared by the ammonia evaporation hydrothermal method.³⁰ Briefly, the appropriate amounts of $\text{Cu}(\text{NO}_3)_2 \cdot 3\text{H}_2\text{O}$ was dissolved in 30 mL of deionized water. Then, four equivalent moles of NH_3 (30wt.% NH_4OH solution) were added to the solution under vigorous stirring. After 30 min, 5.84 g of colloidal silica were introduced into this mixture and stirred for 24 h. The mixture was heated at 80 °C in a water bath to evaporate NH_3 , in which the pH was dropped from 11 to ~7. The remaining mixture was transferred to Teflon-line autoclaved and was treated hydrothermally at 150 °C for 24 h. After that, the suspension was filtered, washed with deionized water, and dried at 60 °C for 24 h. The obtained solids was calcined in a horizontal tube furnace under air (60 mL/min) at 400 °C (2 °C/min) for 4 h. The samples were denoted as xCuPS where x = 8, 20 and 30wt.% of Cu loading. These samples were reduced at 250 °C (10 °C/min) under H_2 (60 mL/min) for 2 h.

3.3.2 Copper supported on silica (Cu/SiO₂)

20wt.% copper supported on silica (denoted as 20Cu/SiO₂) was prepared by incipient wetness impregnation method using copper nitrate trihydrate as a precursor. Briefly, 9.51 g of Cu(NO₃)₂•3H₂O were dissolved in 30.0 mL of deionized water. After that, 10 g of SiO₂ were impregnated by the prepared solution to the wetness and dried at 60 °C. The process was repeated until the prepared solution was used up. Then, the obtained solids were dried in an oven at 60 °C for 24 h. The dried sample was calcined in a horizontal tube furnace under air (60 mL/min) at 400 °C (10 °C/min) for 4 h. The obtained samples were reduced at 250 °C (10 °C/min) under H₂ (60 mL/min) for 2 h, assigned as 20Cu/SiO₂.

3.3.3 K-doped on copper phyllosilicate (K-CuPS)

K-doped on calcined CuPS (K-CuPS) was prepared by incipient wetness impregnation method using KNO₃ as a precursor. Shortly, the appropriate amount of KNO₃ was dissolved in 5 mL of DI water. After that, 1.0 g of CuPS obtained above will be impregnated by the prepared solution to the wetness and dried at 60 °C. The process was repeated until the prepared solution was used up. Then, the obtained sample was dried in an oven at 60 °C for 24 h, denoted as xK-CuPS where x is a K loading (0.05 wt.%).

3.3.4 K-doped on reduced copper phyllosilicate (K-rCuPS)

K-doped on reduced CuPS (K-rCuPS) was prepared by incipient wetness impregnation method using KNO₃ as a precursor. Shortly, 1.0 g of CuPS obtaining from the above preparation, was reduced under H₂ (60 mL/min) at 250 °C (10 °C/min) for 2 h. After cooling down to room temperature, it was impregnated with the appropriate amount of KNO₃ solution (~ 5 mL). The obtained samples were dried at 60 °C for 24 h, denoted as xK-rCuPS where x is a K loading (0.01, 0.05 and 0.10 wt.%)

3.4 Catalyst characterizations

3.4.1 X-ray Fluorescence (XRF)

The chemical composition of catalysts was determined by a wavelength dispersive X-ray fluorescence spectrometry (WD-XRF). The sample was prepared by mixing 4.5 grams of boric acid and 0.5 grams of catalyst, followed by manual grinding. The mixture was packed onto the sample holder and then compressed at 150 kN. The

This material is reserved for educational use only, not allowed for commercial use.

Forbidden to modify the content, and cite the document when use.

sample was placed in the sample chamber. Cu-K α was employed as a source for the measurement with 50kV and 60mA.

3.4.2 Inductively coupled plasma-optical emission spectroscopy (ICP)

The potassium content determination was investigated using inductively coupled plasma-optical emission spectrometer. The sample was digested in hydrofluoric (HF) solution. The solution is introduced into the plasma in a process that desolvates, ionizes, and excites them. The constituent elements can be identified by their characteristic emission lines and quantified against blank. The potassium content was calculated using calibration curve.

3.4.3 X-ray Diffraction (XRD)

X-ray diffraction methods are the most effective methods for determining the crystal structure of materials. The sample was packed onto the sample holder and then pressed surface smooth. X-ray tube Copper is employed as a source for the measurement with 40 kV, 30 mA, Scan range 10-80 deg, step size 0.0200 deg.

3.4.4 Surface area analysis (BET)

The surface area of the catalyst was determined by a surface area analyzer (Autosorb-1C, Quantachrome). The sample was prepared by weighing approximately 30-60 mg of samples and loaded into a cleaned and dried sample cell. The sample was then degassed in an out-gassing station after being filled with nitrogen and attached to the analytical station. The adsorption isotherm was measured in a pressure range of 0.05-0.30 P/P₀ at -196 °C.

3.4.5 Hydrogen Temperature programmed reduction (H₂-TPR)

The reducibility property of metal contents can be determined by a temperature-programmed reduction by H₂ gas (H₂-TPR). The measurement was performed in a quartz tube connected with a thermal conductivity detector (TCD). Prior to an analysis, the sample (0.015 g approximately) was activated in the air (30 mL/min) from room temperature to 400 °C at a heating rate 1 °C /min. The system was naturally cooled down in the atmosphere of nitrogen gas (30 mL/min) to room temperature. Then, the gas was switched to 10% H₂ in Ar and purged for 30 min. The temperature reduction profile was performed using 10% H₂ in Ar at the heating rate of

10 °C /min, from 80 to 900 °C. The TCD signal was calibrated employing a known mass of CuO as a standard, considering that CuO is reduced stoichiometrically and completely to Cu and H₂O. The internal TCD calibration was performed after every run by pulsing 1% H₂/Ar in the fixed loop. The reduction profile of CuO and the use of hydrogen is equal to the number of moles of copper. The amount of metal loading is expressed as a mmol of H₂ consumed per mass of a catalyst (mmol H₂/g)

3.4.6 Ammonia Temperature programmed desorption (NH₃-TPD)

The acid site of the catalyst was assessed using ammonia temperature-programmed desorption (NH₃-TPD). The measurement was performed in a quartz tube connected with a thermal conductivity detector (TCD). Prior to an analysis, the sample (0.2 g approximately) and sample were pretreated by calcination at 400 °C at a heating rate 1 °C /min under air (30 mL/min) for 2 h and reduced at 250 °C at a heating rate 10 °C /min under H₂ (30 mL/min) for 2 h to reduce Cu²⁺ to Cu⁺ and Cu⁰, then NH₃ gas was introduced at a flow rate of 30 mL/min at 30 °C for 1 h. He gas was used to remove the physisorbed NH₃ gas at 30 °C for 40 min. Afterward, the NH₃-TPD profiles were obtained by a heating sample at a rate of 10 °C/min in a flow of He gas (30 mL/min) from 50 to 900 °C.

3.4.7 Pyridine-adsorbed infrared spectroscopy (Py-IR)

The Brønsted and Lewis acid sites were analyzed using pyridine-adsorbed infrared spectroscopy (Py-IR, Thermo Scientific Nicolet iS50 spectrometer with an in-situ quartz cell). Briefly, the sample was reduced at 250 °C for 2 h under 10% H₂/Ar (50 mL/min). Once it was cooled down to 150 °C, the sample was purged by pyridine vapor for 1 h. After that, excess pyridine was removed under a vacuum (1.2×10^{-3} Pa) for 1 h. Finally, the sample was heated to 200 °C (10 °C/min) and the FTIR spectra were recorded.³¹

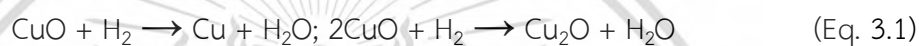
3.4.8 Dissociative N₂O adsorption using H₂-TPR

The copper dispersion (D_{Cu}) can be determined by the hydrogen consumption from copper metallic on the surface. The measurement was performed in a quartz tube connected with a thermal conductivity detector (TCD). Prior to an analysis, the approximately 0.0015 g of sample was activated with 30 mL/min of airflow from room temperature to 400 °C at the heating rate of 10 °C/min. The system was automatically

This material is reserved for educational use only, not allowed for commercial use.

Forbidden to modify the content, and cite the document when use.

cooled down in the nitrogen atmosphere with a flow rate of 30 mL/min to room temperature. Then, the gas was switched to 10% H₂/Ar and purged for 30 min. The temperature reduction profile was carried out by using 10% H₂/Ar at the heating rate of 10 °C/min from 35 °C to 250 °C hold 2 h (Eq. 3.1). The sample was cooled down to room temperature under nitrogen. Afterward, the sample was reoxidized using nitrous oxide (99.00 %) at 60 °C for 1 h (Eq. 3.2). Then, the gas was switched to N₂ for 30 min and cooled down to 40 °C. The sample was performed the second H₂-TPR, in which the reduction took place only at the surface (Eq. 3.3). The dispersion of copper on the surface could be calculated by the hydrogen consumption of primary and secondary H₂-TPR.²²



The dispersion of metallic copper was calculated by the following equation:

$$\text{Cu dispersion } (D_{\text{Cu}}) = \frac{2 \times A_2}{A_1} \times 100 \quad (\text{Eq. 3.4})$$

3.4.9 Transmission electron microscopy (TEM)

Transmission electron microscope (TEM) was carried out to study metal particle size, morphology and crystallographic structure. For sample preparation, 5 mg sample powder was grinded by agate mortar. The fined powder was dispersed in the ethanol under an ultrasonic condition. The suspension was dropped onto copper coated Formvar grid and left to dry at a room temperature overnight. The copper grid was loaded into the TEM instrument. The microscope performed using LaB₆ electron source with high tension electron of 200 kV (100,000–300,000x magnification). The particle size distribution was measured using the Image J software.

3.4.10 *In situ* X-ray absorption near-edge structure spectroscopy.

In situ time-resolved X-ray adsorption near-edge structure (*in situ* TR-XANES) spectroscopy experiments were performed at BL2.2: TRXAS, Synchrotron Light Research Institute (SLRI), Thailand. An energy dispersive monochromator and position

sensitive detector was employed to perform XANES measurement.⁶¹ The Cu K-edge XANES was collected using the integration time of 2000 ms with an average of 10 scans. For preparation, the sample powder was mixed with boron nitride and pelletized. The sample concentration needs to be optimized to find the best ratio for edge jump energy. To determine Cu^{2+} species, the sample was *in situ* calcinated in 20% O_2 in N_2 at 400 °C (5 °C/min) for 2 h. The data was recorded at every 30 minutes during calcination. The characteristic adsorption of Cu K-edge and molecular geometry of the samples were comparable with Cu^{2+} standard (i.e. CuO and CuSO_4). After calcination, the samples were cooled down in N_2 to room temperature and then reduced under 10% H_2/N_2 from 30 °C to 250 °C for 2 h. The data was recorded at every 1 minutes during the ramping step to 250 °C. The data was processed using the Athena software. Cu foil, Cu_2O , CuO and CuSO_4 as standards were used to determine the composition of Cu^0 , Cu^+ , square planar Cu^{2+} and octahedral Cu^{2+} species at different reduction temperature by linear combination fitting (LCF) of normalized XANES spectra samples.

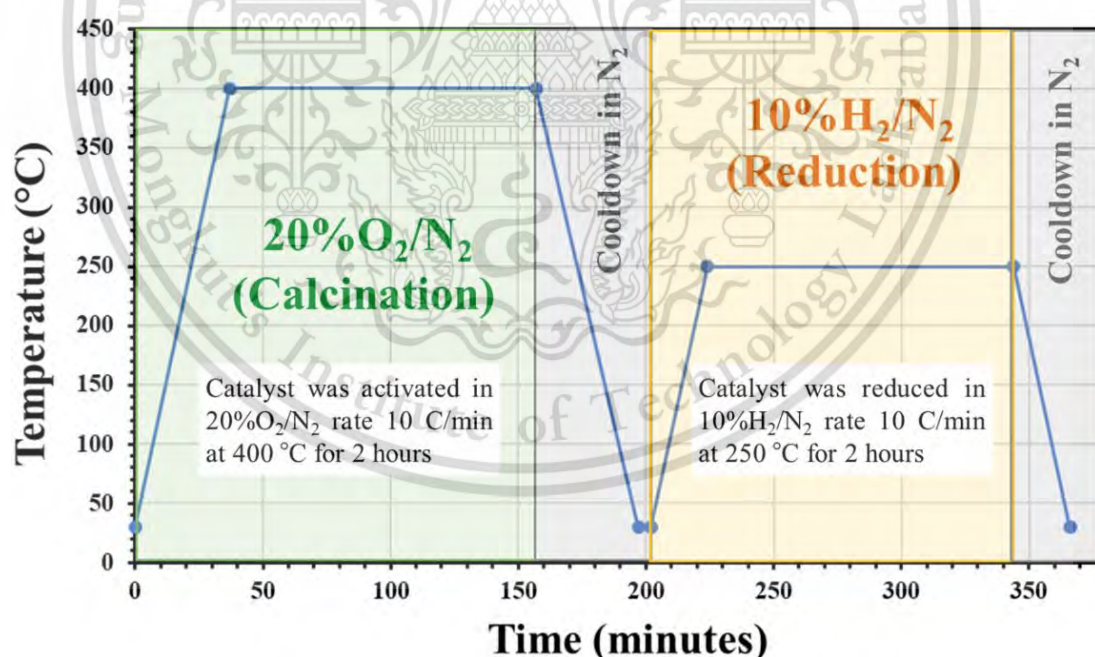


Figure 3.1 Temperature program of *in situ* XANES experiments.

3.5 Catalytic activity

The gas phase hydrogenation of methyl palmitate was carried out in a fixed bed reactor, and the schematic diagram is shown in Figure 3.2.

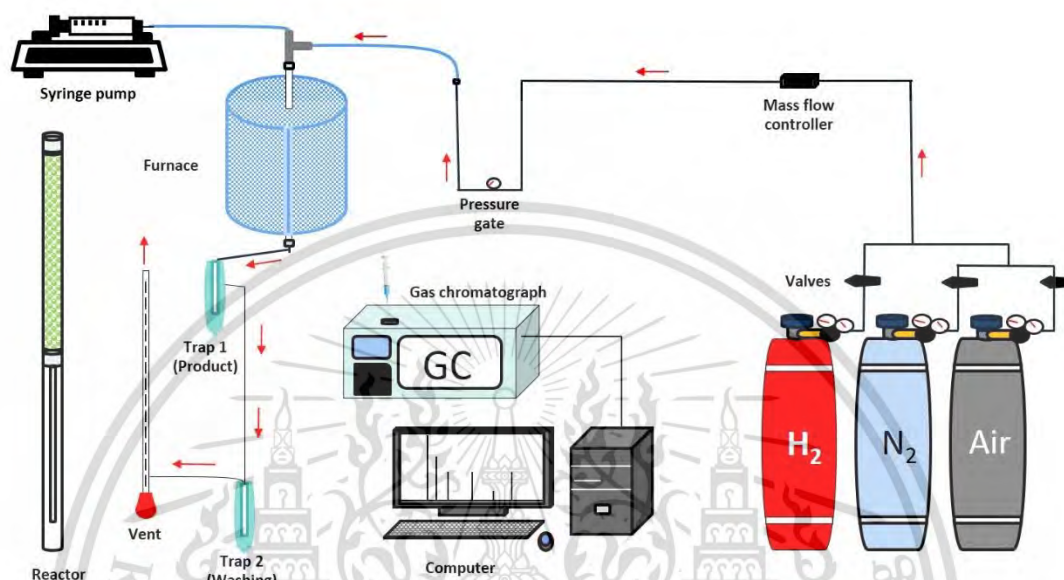


Figure 3.2 Catalytic system of methyl palmitate conversion.

The methyl palmitate conversion was investigated in a continuous fixed-bed reactor made with a glass tube (8 mm O.D.) under the atmospheric pressure of H_2 . Before the catalytic testing, the catalyst was calcined under air (60 mL/min) at 400 °C with a heating rate of 10 °C/min for 2 h. It was then naturally cooled down to 50 °C under N_2 . Next, the catalyst was reduced under H_2 (60 mL/min) at 250 °C (10 °C/min) for 2 h. Finally, the reaction was performed using 10wt.% methyl palmitate in dodecane (2.4 mL/h) under the stream of H_2 (180 mL/min). The liquid products were trapped with *iso*-propanol and collected to analyze by gas chromatography equipped with a flame ionization detector (GC-FID) using an MXT-1 capillary column.

Table 3.2 Operating condition of gas chromatography.

GC parameter	Conditions
Carrier gas	N ₂
Carrier gas flow rate (mL/min)	25.15 mL/min
Inlet temperature	250 °C
Detector temperature	280 °C (FID)
Column temperature program	50 °C to 280 °C (ramping rate 12 °C/min)



This material is reserved for educational use only, not allowed for commercial use.

Forbidden to modify the content, and cite the document when use.

Chapter 4

Linear long-chain α -olefins from Hydrodeoxygenation of Methyl palmitate over Copper phyllosilicate catalysts

In this chapter, we reported the hydrodeoxygenation (HDO) of FAMES to produce linear long-chain α -olefins using CuPS catalysts in a gas-phase reactor under atmospheric H₂ pressure. Methyl palmitate (MP) was selected as a feed model for FAMES. The effect of Cu loading on the reducibility and Cu dispersion were evaluated by the dissociative N₂O adsorption followed by a subsequent H₂-temperature-programmed reduction (H₂-TPR) test, and transmission electron microscopy (TEM). The existence and transformation of Cu species in the CuPS upon calcination and reduction were investigated using *in situ* time-resolved X-ray adsorption near-edge structure spectroscopy (*in situ* TR-XANES) and X-ray diffraction spectroscopy (XRD). The influence of Cu loading on the nature of Cu species and its relationships with Brønsted/Lewis acid sites were investigated. The structure-activity relation of active Cu surface area, acid sites, and the selectivity of linear long-chain α -olefin was thereby revealed.

4.1 Results and discussion

4.1.1 Characterization of catalysts

Cu contents of the prepared catalysts are shown in Table 4.1. The observed metal loadings are in agreement with the desired catalyst preparation. All calcined CuPS samples provide weak XRD peaks at 30.8°, 35.0°, 57.5° and 62.4°, corresponding to the chrysocolla characteristics ($\text{Cu}_2\text{Si}_2\text{O}_5(\text{OH})_2$) of the copper phyllosilicate²⁹, as display in Figure 4.1a, ii-iv. The characteristic peak of copper phyllosilicate was more obvious when copper loading was increased, particularly at ≥ 20 wt.% Cu. This is because the formation of the chrysocolla structure requires Cu^{2+} in the octahedral layers.³⁰ In a supportive manner, a broad signal of amorphous SiO_2 at 2θ 20-30° becomes flatter, especially in 30CuPS.²² The surface area of the samples is also increased upon the increment of copper content (152 to 400 m^2/g for 8 to 30wt.% CuPS), as in Table 4.1 entry 1-3. Furthermore, all samples reveal a type IV N_2 adsorption-desorption isotherm (Appendix A, Figure A1), indicating the mesoporous character of phyllosilicates with pore diameters in the range of 3-50 nm, similar to those reported in the literature.²²

Table 4.1 Metal loading, surface area, pore size, pore volume, H_2 -consumption, Cu surface area and Cu dispersion of CuPS and Cu/ SiO_2 samples.

Entry	Catalysts	Metal content Cu (wt.%) ^a	N_2 - adsorption						H_2 -TPR			
			Before reduced			After reduced			H_2 consumption (mmol/g) ^b	Cu content (wt.%) ^b	S_{Cu}^0 (m^2/g) ^c	D_{Cu} (%) ^c
			S_{BET} (m^2/g)	D_{pore} (Å)	V_{pore} (cm^3/g)	S_{BET} (m^2/g)	D_{pore} (Å)	V_{pore} (cm^3/g)				
1	8CuPS	7.6	152	290	1.10	115	280	0.80	0.88	5.6	34.4	79.8
2	20CuPS	20.8	344	158	1.35	183	126	0.58	3.02	19.2	92.3	72.9
3	30CuPS	28.0	400	121	1.21	230	98.2	0.56	4.34	27.0	106.3	60.7
4	20Cu/ SiO_2	18.5	198	207	1.03	178	181	0.79	2.96	18.6	12.7	10.1

^(a)Determined by XRF, ^(b)Estimated by H_2 -TPR, ^(c)Calculated by dissociative N_2O adsorption.

It is important to emphasize that the CuO phase was not identified in all calcined CuPS samples, even at 30wt.% loading. However, the characteristic peaks of CuO were clearly obtained in 20Cu/SiO₂ with a crystalline size of 26 nm, as depicted in Figure 1a, i. These observations lead to the suggestion that the Cu²⁺ species is highly dispersed as well-defined Cu²⁺ ions strongly interact with the SiO₂ layers in octahedral sites in the chrysocolla structure of the phyllosilicates.⁶² Conversely, a much weaker interaction between Cu²⁺ and SiO₂ could lead to an agglomeration of CuO particles upon calcination for the impregnated sample. This also results in a significant drop in surface area (from 331 to 198 m²/g) compared with the parent SiO₂ support, presumably due to the pore blocking (from 1.33 to 1.03 cm³/g). It is worth noting that the observed mesopores in 20Cu/SiO₂ are attributable to the silica support (Davisil).

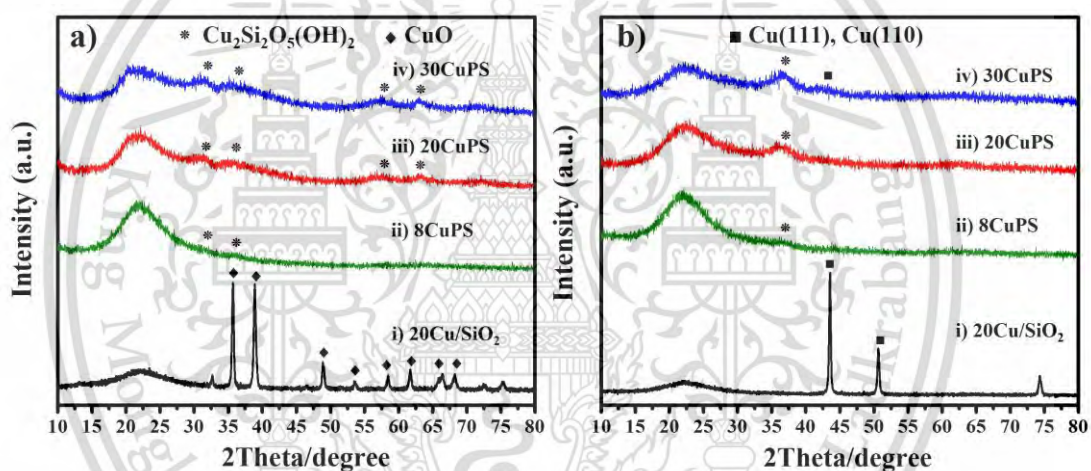


Figure 4.1 XRD patterns of a) calcined and b) reduced CuPS and Cu/SiO₂ samples.

To understand the Cu species in the calcined CuPS samples, the *in situ* time-resolved X-ray absorption near-edge spectroscopy (*in situ* TR-XANES) was performed, as depicted in Figure 4.2. The Cu edges energy for Cu foil, Cu₂O, CuO (square planar geometry, Cu²⁺(Sq)) and CuSO₄ (octahedral geometry, Cu²⁺(O_h)) are 8979.1, 8980.5, 8990.2, and 8992.3 eV, respectively (Table A1). As compared to the Cu standards, it is evident that all calcined CuPS samples present characteristic edge energy absorption for Cu²⁺ at ~8991 eV. It is essential to highlight that the values fall between the Cu edge energy of CuSO₄ (8992.3 eV) and CuO (8890.2 eV). Therefore, it is likely that a mixture of octahedral Cu²⁺(O_h) and square planar Cu²⁺(Sq) is present in the calcined CuPS samples. Nevertheless, the line-shape spectra of the samples more resemble

that of CuSO_4 , without a pre-edge feature at ~ 8984 eV that represents the square planar $\text{Cu}^{2+}(\text{Sq})$ species (Figure 4.2b). This suggests that the majority of the Cu^{2+} species in the CuPS samples exist in the octahedral geometry, presumably within the chrysocolla structure.

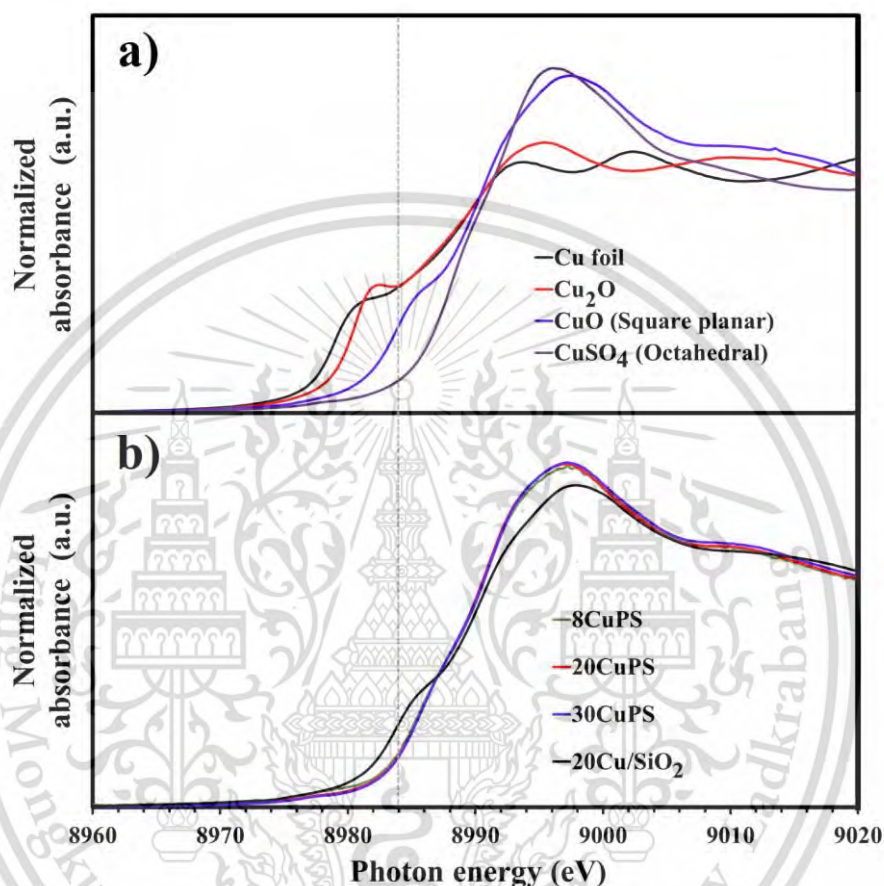


Figure 4.2 Cu K edge XANES spectra of a) Cu standards and b) CuPS samples and $20\text{Cu}/\text{SiO}_2$ after calcination at 400°C for 2 h.

To evaluate the octahedral $\text{Cu}^{2+}(\text{O}_h)$ and square planar $\text{Cu}^{2+}(\text{Sq})$ species, the linear combination fitting (LCF) of *in situ* TR-XANES spectra was performed on the calcined samples, as demonstrated in Figure A2. The composition from the LCF as a function of temperature is depicted in Figure 4.3. At 50°C , the 8CuPS exhibits relatively higher fraction of octahedral $\text{Cu}^{2+}(\text{O}_h)$ (76 %), as compared to 20CuPS (66%) and 30CuPS (62%). In accordance with this finding, the Cu edge energy slightly shifts to a lower value for the samples with higher Cu loadings. This could indicate a relatively lower electron density of Cu^{2+} in 8CuPS, as compared to 20CuPS and 30CuPS.

This material is reserved for educational use only, not allowed for commercial use.

Forbidden to modify the content, and cite the document when use.

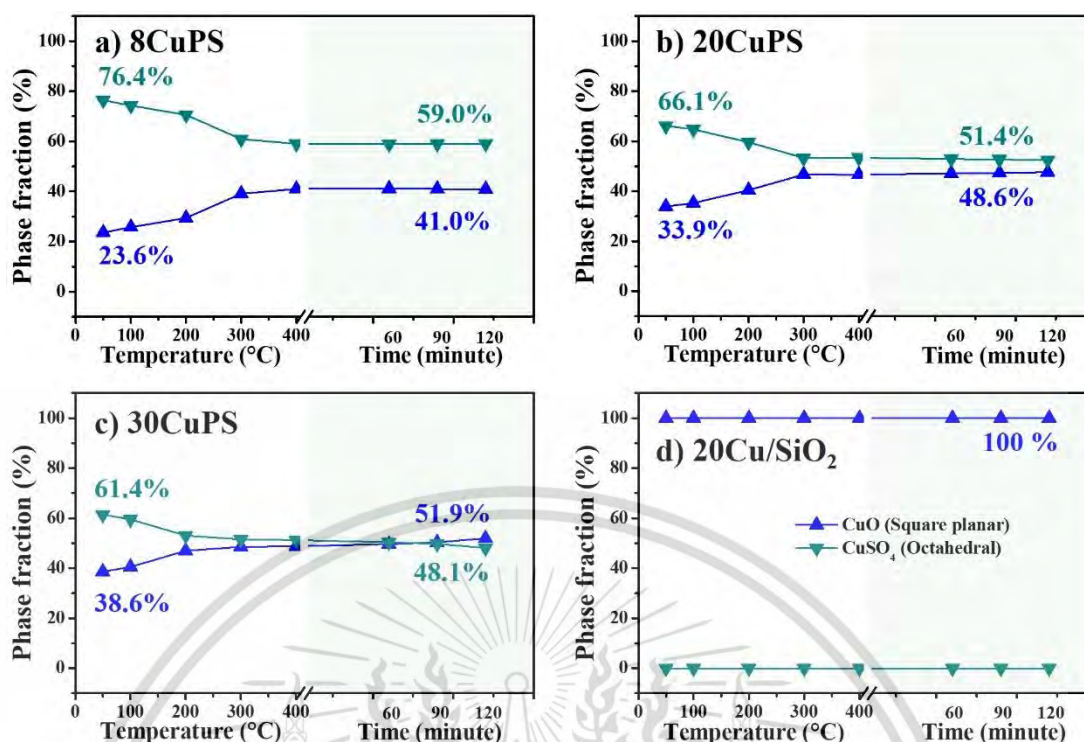
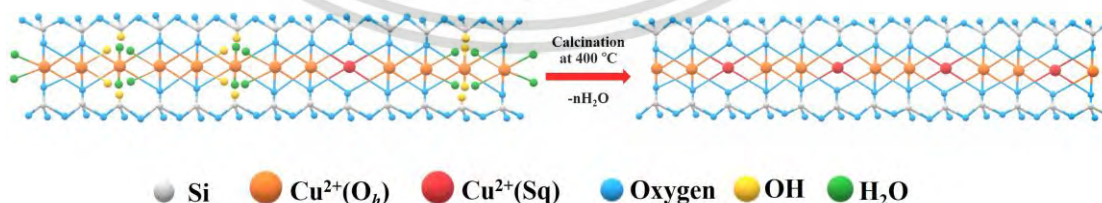


Figure 4.3 Fractions of Cu²⁺ species from LCF of a) 8CuPS, b) 20CuPS, c) 30CuPS and d) 20Cu/SiO₂ upon calcination.

The in-situ TR-XANES also revealed that the Cu²⁺(O_h) species are converted into Cu²⁺(Sq) species, upon heating from 50 °C to 400 °C (Figure 4.3, a-c). This is presumably due to (i) the dehydration of adsorbed water at the layer edge and (ii) the dehydroxylation of the interlayered Si-O-Cu-(OH)₂, as previously reported by Heller-Kallai, et al.⁶³ The dehydroxylation could proceed via protonation of the adjacent hydroxyls, forming a highly dispersed Cu²⁺(Sq) species, as illustrated in Scheme 4.1.



Scheme 4.1 The demonstration of Cu²⁺(O_h) transformation to Cu²⁺(Sq) under the calcination at 400 °C.

On the other hand, the Cu edge energy of calcined 20Cu/SiO₂ (8990.2 eV) precisely matches that of the CuO standard (8990.2 eV). Additionally, the presence of a pre-edge feature at approximately 8984 eV (as illustrated in Figure 4.2b) strongly suggests that the Cu²⁺ species would virtually exist in 4-coordinate square planar geometry.⁶⁴ In line with this perspective, the LCF results indicate only Cu²⁺(Sq) species in 20Cu/SiO₂ (Figure 4.3d). This result also corresponds with the XRD results where the high crystalline CuO particles are observed.

Accordingly, the 20Cu/SiO₂ displays a relatively broad reduction peak (~220 °C) for large and ununiform CuO particles (Figure 4.4a, i).³⁰ While CuPS samples show a sharp reduction peak at lower temperatures (~181-186 °C, Figure 4.4a, ii-iv). Together with an absence of CuO peak in the XRD, these features suggest the existence of highly dispersed Cu²⁺ species in CuPS samples. Furthermore, the reduction peak of CuPS samples was decreased from 186 °C (8CuPS) to 181 °C (30CuPS). Consistent with *in situ* TR-XANES, the higher fraction of Cu²⁺(O_h) species could provide higher Cu edge energy. This is because the higher number of Cu-O bonds in an octahedral environment results in an electron deficiency of the Cu²⁺. Consequently, the Cu²⁺(O_h) species would exhibit strong interactions with the SiO₂ layer, resulting in a higher reduction temperature, especially for 8CuPS.

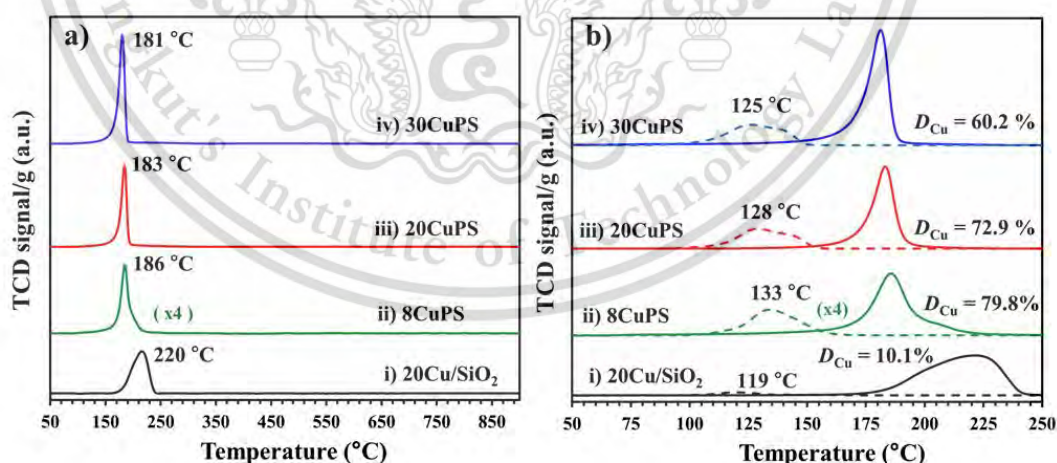


Figure 4.4 a) H₂-TPR profiles (from 50-900 °C) and b) first H₂-TPR (solid line) and second H₂-TPR (dash line) (from 50-250 °C) after dissociative N₂O adsorption for i) 20Cu/SiO₂, ii) 8CuPS, iii) 20CuPS and iv) 30CuPS.

It is noteworthy that Cu content, as calculated from the H₂ consumption of all CuPS samples, is lower than the values determined by the XRF (Table 4.1), while XRF and H₂-TPR estimated Cu contents for 20Cu/SiO₂ were nearly identical (18.5 and 18.6 wt.%). This observation suggests that Cu²⁺ species in CuPS samples might not be completely reduced to metallic Cu, particularly at lower Cu loading. Table A2 reveals approximately 26%, 8%, and 4% lower Cu content were observed for 8CuPS, 20CuPS, and 30CuPS, respectively. This is in line with a report by Jiang et al. that Cu⁺ species were observed in the CuPS, even after the samples were reduced at 300 °C.²² As discussed earlier, the existence of Cu⁺ species could be attributed to the strong interaction between Cuⁿ⁺ and SiO₂ in the phyllosilicate structure. Since 8CuPS exhibits a notable loss of H₂ consumption (Table A2) and relatively higher reduction temperature (Figure 4.4a, ii), it is reasonable to assume that this sample presumably contains a higher fraction of Cu⁺ after the reduction.

To investigate the transformation of Cu species during the reduction process, the in-situ TR-XANES under 10%H₂/N₂ was consecutively performed after heating at 400 °C for 2 h, as shown in Figure 4.5. Within the temperature range of 50-210°C, a further decrease in Cu²⁺(O_h) species in all CuPS samples was observed, even though the fraction of this species remains constant under heating in air at 400 °C (Figure 4.3). In response to such a decrease, Cu²⁺(Sq) species gradually increased, suggesting that the dehydroxylation of Cu²⁺(O_h) species to Cu²⁺(Sq) species was facilitated under hydrogen.

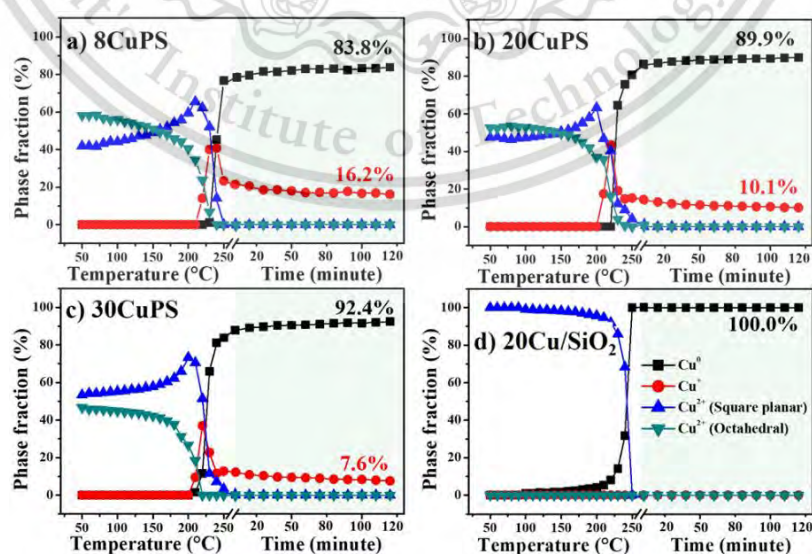


Figure 4.5 Fractions of Cu species from the LCF of a) 8CuPS, b) 20CuPS, c) 30CuPS and d) 20Cu/SiO₂ under upon the reduction.

This material is reserved for educational use only, not allowed for commercial use.

Forbidden to modify the content, and cite the document when use.

It is plausible that, the hydrogen might undergo reversibly dissociate Si-O-Cu-O-Si, forming internal Si-OH and H-Cu-O-Si. The latter species could potentially react with the neighboring HO-Cu-O-Si, resulting in the release of H₂ and the formation of Cu-O-Cu bonds.⁶⁵ As H₂ is equally consumed and released in this process, no change in the TPR signal was observed. Nevertheless, *in situ* TR-XANES experiment has suggested that the coordination of Cu²⁺ has been modified under hydrogen without change in the oxidation state.

The reduction of Cu²⁺ to Cu⁺ species could be initially observed at 220 °C, followed by the formation of Cu⁰ at 230 °C as displayed in Figure 4.5, a-c. These two species were evolved along with the decreases in Cu²⁺(O_h) and Cu²⁺(Sq) species. While the Cu²⁺(Sq) was remained predominant, the increase in Cu⁺ seemed to correspond with the decrease in Cu²⁺(O_h). Above 210 °C, the decrease in Cu²⁺(Sq) and the increase in Cu⁰ species were significant, showing similar rates of phase transformation. This observation suggests that the Cu²⁺(O_h) species undergo partial reduced to Cu⁺ at below 210°C, presumably due to a strong interaction of Cu⁺ in octahedral geometry with the SiO₂ layers. However, some Cu⁺ could be further reduced to Cu⁰, as observed by a decrease in Cu⁺ fraction at >225°C. In contrast, the Cu⁺ is less stabilized in the square planar geometry, resulting in a complete reduction of the Cu²⁺(Sq) species to Cu⁰. In comparison, the impregnated sample (20Cu/SiO₂), which contained only Cu²⁺(Sq) species, was completely reduced to Cu⁰, without Cu⁺ intermediate species, during H₂ reduction as shown in Figure 4.5, d. Consequently, the samples with a higher fraction of Cu²⁺(O_h) species, such as 8CuPS, would yield a greater Cu⁺ composition. After holding at 250 °C for 2 h under 10%H₂/N₂, the Cu⁺ fraction retained in the samples are in order of 16.2%(8CuPS) > 10.1%(20CuPS) > 7.6%(30CuPS). This trend is consistent with the increase in H₂ consumption of respective samples, as discussed in H₂-TPR.

Although H₂-TPR and *in situ* TR-XANES suggest that CuPS can be readily reduced to Cu metal, no diffraction peak corresponding to Cu⁰ ($2\theta = 43.2^\circ$, 50.4° and 74.2°) was observed in the XRD pattern of the reduced samples as seen in Figure 4.1b, ii-iv. This suggests that very fine Cu⁰ particles were generated in the reduced CuPS. In accordance with this perspective, TEM shows average Cu particle sizes of the CuPS samples in the 1.9-4.9 nm as depicted in Figure 4.6, a-c, much smaller than that of Cu/SiO₂ (~11 nm, Figure 4.6, d). Since the lamellar structure of CuPS can undergo partial collapse during reduction, a notable decrease in surface area of all CuPS samples was observed. This material is reserved for educational use only, not allowed for commercial use.

Forbidden to modify the content, and cite the document when use.

obtained as detailed in Table 4.1. Nevertheless, as previously discussed, the remaining lamellar structure of reduced catalysts (as observed by TEM, Figure A3) would retain Cu^+ species. These Cu^+/SiO_2 layers would strong interactions with the metallic Cu particles, preventing the agglomeration, as reported in literatures.^{62, 66}

Consequently, a high dispersion of Cu particles could be observe for all CuPS samples (~60-80%), depending on the Cu^+ fraction in the samples, as indicated in Figures 4.4b and 5. Hence, an increase in Cu loadings (from 8% to 30%), a decrease in Cu^+ fraction, results in a proportional increase in Cu particle size (from 1.9 to 4.9 nm), a decrease in Cu dispersion (from ~80% to 60%), as illustrated in Figure A4. In contrast, the large Cu^0 particles of $20\text{Cu}/\text{SiO}_2$ could be attributed to the low interaction of the bulk CuO with the silica support. This leads to completely reducing $\text{Cu}^{2+}(\text{Sq})$ species to Cu^0 without Cu^+ species, as evident in Figure 4.5d. Consequently, the metallic Cu particles on the $20\text{Cu}/\text{SiO}_2$ catalyst are more prone to agglomeration after reduction, resulting in a lower Cu dispersion of approximately 10% (as detailed in Table 1 and illustrated in Figure 4.4b, iv).

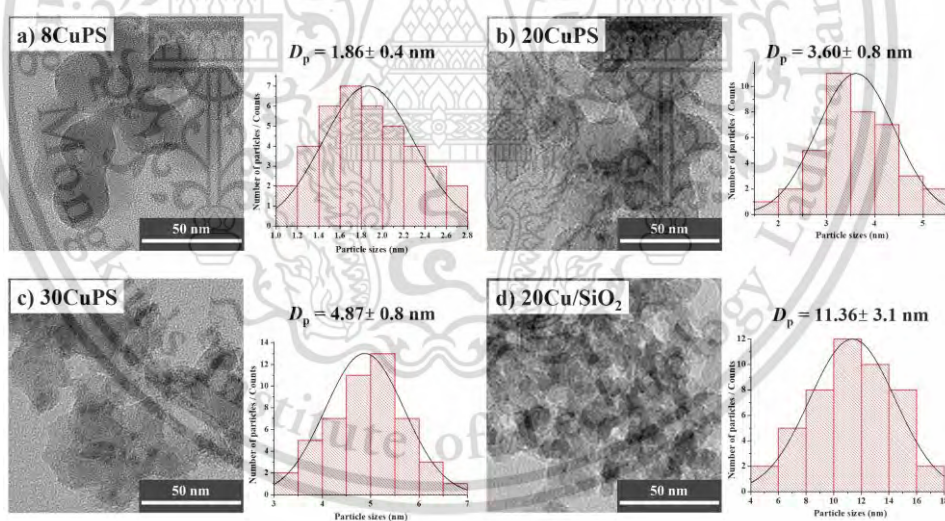


Figure 4.6 TEM images and particle size distribution histograms of a) 8CuPS, b) 20CuPS, c) 30CuPS and d) $20\text{Cu}/\text{SiO}_2$.

The acid sites of all Cu-based catalysts were investigated by the NH_3 -TPD, as depicted in Figure 4.7a. The desorption peaks were deconvoluted into three distinct peaks via the Gaussian deconvolution method. All Cu-based catalysts exhibited three desorption peaks. The peaks at 120 °C corresponded to weak acid sites derived from

surface silanol⁶⁷, whereas a broad peak at 250 °C could be attributed to the NH₃ adsorbed on the internal silanol located in the micropores or interlayers.⁶⁸ Furthermore, the peak at 160 °C can be attributed to medium acid sites derived from the Cu species.⁶⁹ The acidity, calibrated with standard 1% NH₃ in He, is listed in Table 4.2 for each peak. It can be seen that the medium acid sites of CuPS increased proportionally with the Cu loading, from 9 μmol/g (8CuPS) to 16 μmol/g (30CuPS), while sites derived from the silanol groups (Si-OH) remained relatively consistent. Furthermore, the 20Cu/SiO₂ exhibited a much lower medium acid site (5 μmol/g) than the phyllosilicate counterpart (20CuPS, 12 μmol/g). This could be attributed to the lower Cu surface area of the impregnated samples, as previously discussed.

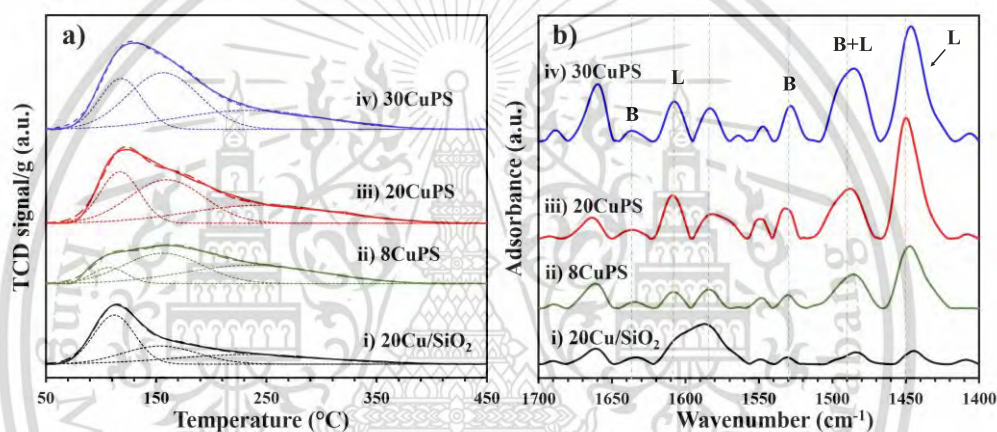


Figure 4.7 a) NH₃-TPD desorption profiles and b) pyridine-adsorbed IR spectra of i) 20Cu/SiO₂, ii) 8CuPS, iii) 20CuPS and iv) 30CuPS (B – Brønsted acid sites, L – Lewis acid sites).

To gain more details of the specific acid sites over the reduced catalysts, the Py-IR was performed. As demonstrated in Figure 4.7b, the CuPS catalysts displayed adsorption bands at 1450 and 1606 cm⁻¹, associated with the pyridine adsorbed on Lewis acid sites (LAS)⁷⁰, and the bands at 1530 and 1633 cm⁻¹, evidenced for pyridine bonded with Brønsted acid sites (BAS).⁷¹ The band at 1490 cm⁻¹, for both BAS and LAS⁷² was also observed. The acidity of the samples was calibrated using the HZSM-5 standard (Si/Al ~ 21), a reference with known acidity, and is detailed in Table 4.2. In contrast to the CuPS catalysts, the 20Cu/SiO₂ catalyst exhibited a sole adsorption band at 1580 cm⁻¹, which could be attributed to pyridine adsorbed on the silanol group (Si-OH).

This material is reserved for educational use only, not allowed for commercial use.

Forbidden to modify the content, and cite the document when use.

Table 4.2 Acidity and type of acid sites of all reduced catalysts.

Entry	Catalyst	Acidity ($\mu\text{mol/g}$) ^a			Type of acid site ($\mu\text{mol/g}$) ^b		LAS/Cu ⁺ ($\times 10^{-2}$)	BAS/Cu _s ⁰ ($\times 10^{-4}$)
		Weak acid sites- External silanol (120 C)	Medium acid sites- Cu surface (160 C)	Strong acid sites- Internal silanol (250 C)	Lewis acid (LAS)	Brønsted acid (BAS)		
1	8CuPS	2.1	9.0	9.4	2.35	0.37	1.21	4.3
2	20CuPS	7.1	11.4	9.3	4.08	0.82	1.23	3.8
3	30CuPS	8.2	15.4	10.3	4.28	0.91	1.28	3.6
4	20Cu/SiO ₂	7.4	5.0	5.3	-	-	-	-

^(a)Evaluated by NH₃-TPD. ^(b)Calculated from FTIR of adsorbed pyridine (Py-IR).

The Lewis acid sites (LAS) in CuPS samples can be attributed to the remaining Cu⁺ species, as confirmed by *in situ* TR-XANES. In support of this view, the LAS was increased linearly with the remaining Cu⁺ content in the samples, as depicted in Figure 4.8a. However, the amount of LAS is lower than the overall Cu⁺ content (LAS/Cu⁺ < 1, Table 4.2), indicating that only some Cu⁺ species were exposed to the surface, while the remainder remained embedded within the layered structure. In the case of 20Cu/SiO₂, the Cu⁺ species was not present in the sample after the reduction. Therefore, the LAS adsorption band was barely detected on the impregnated catalyst.

The number of BAS was increased with the Cu loading, particularly in relation to the Cu⁰ content, as illustrated in Figure 4.8b. The relatively lower BAS, as compared to the Cu content, suggests that BAS could be derived from the silanol (Si-OH) group at the interface of Cu particles.⁷³ The perturbation of d-band electrons of Cu metal on the interface Si-OH results in an electron deficiency of hydrogen at the perimeter.⁶⁹ Consequently, 30CuPS, characterized by a higher proportion of metallic Cu phase (as observed in Figure 4.5), would exhibit a greater number of BAS. However, the number of BAS at the perimeter depends on the Cu metal particle size. The smaller the particle size, the higher the number of BAS at the perimeter. In other words, the sample with high Cu dispersion would possess a higher BAS at the perimeter. Consequently, a higher ratio of BAS/Cu on the surface (Cu⁰) was attained for 8CuPS, characterized by a higher Cu metal dispersion, as detailed in Table 4.2.

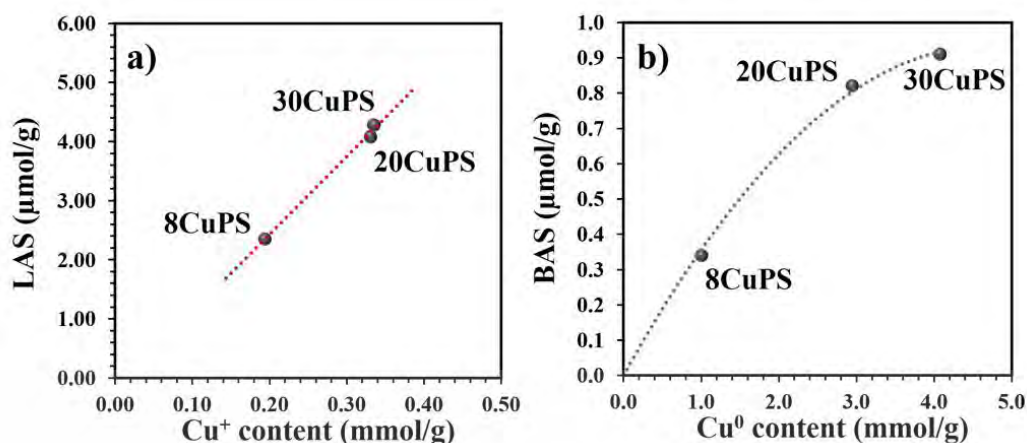


Figure 4.8 The relationship between a) Lewis acid sites (LAS) vs Cu^+ content and b) Brønsted acid sites (BAS) vs Cu^0 content.

4.1.2 Catalytic activity

The gas-phase hydrodeoxygenation of methyl palmitate (MP) was conducted at 250 °C under atmospheric H_2 pressure. The 20CuPS catalyst exhibited ~5-fold conversion higher than 20Cu/SiO₂ catalyst (73% vs. 13%), as presented in Table 4.3, entries 1 and 2. Such high activity of the 20CuPS catalyst could mainly derive from a higher Cu dispersion (73%) compared to that of 20Cu/SiO₂ (10%). In other words, the 20CuPS possesses an active Cu surface area (92.3 m²/g), higher than that of 20Cu/SiO₂ (12.7 m²/g, Table 4.1). This could be attributed to the presence of well-defined Cu^{2+} species ($\text{Cu}^{2+}(\text{O}_h)$, $\text{Cu}^{2+}(\text{Sq})$) in the 20CuPS structure, as elucidated by *in situ* TR-XANES. These Cu^{2+} species can be reduced to Cu^0 and Cu^+ species, and the latter could prevent the agglomeration of metallic Cu particles after the reduction leading to the formation of very fine metallic Cu particles, as illustrated in Figure 4.6b.

Table 4.3 Catalytic activity, product yields and selectivity in hydrodeoxygenation of methyl palmitate over CuPS catalysts.

Entry	Catalyst	W/F (g,h/mol)	Conversion (%)	Product yields, % (Product selectivity, %)					
				Hexadecene	Hexadecane	Hexadecanal	Hexadecanol	Pentadecene	Pentadecane
1	20Cu/SiO ₂	374	13.0	0.7 (5.3)	0.3 (2.3)	2.6 (20.0)	7.8 (60.1)	0.2 (1.3)	0.1 (0.7)
2	20CuPS	374	73.2	30.5(41.7)	17.8 (24.3)	3.3 (4.5)	14.1 (19.2)	-	-
3	8CuPS	374	19.9	1.6 (8.2)	1.2 (5.9)	3.3 (16.3)	12.2 (61.6)	-	-
4	30CuPS	374	77.3	32.0 (41.3)	27.0 (35.2)	3.0(3.9)	7.8 (10.1)	-	-
5	20CuPS	94	21.8	4.2 (19.3)	2.2 (10.1)	3.0 (13.8)	11.9 (54.6)	-	-
6	30CuPS	63	20.1	5.9 (29.3)	3.1 (15.2)	2.1 (10.6)	9.0 (44.5)	-	-

This material is reserved for educational use only, not allowed for commercial use.

Forbidden to modify the content, and cite the document when use.

The products obtained from both 20CuPS and 20Cu/SiO₂ catalysts include hexadecanal, hexadecanol, hexadecene, and hexadecane. Among the C₁₆-olefins, 1-hexadecene is mainly obtained, with a trace amount of inner- and iso-olefins. Nevertheless, minimal traces of pentadecene and pentadecane, corresponding to C₁₅-products, were observed for the 20Cu/SiO₂ catalyst, resulting from the decarbonylation of methyl palmitate. These products were absent in the case of the CuPS catalysts, even at a higher conversion. This could emphasize the ability of the Cu-based catalyst to suppress decarbonylation reactions, which are typically enhanced by oxophilic metals (Co⁷⁴, Ni⁷⁵, and Fe¹⁹) and noble metal catalysts (Pd⁷⁶ and Pt⁴⁷).

To examine the evolution of these products, the correlation of conversion and product yields with the contact time was investigated for 20CuPS, as depicted in Figure 4.9. At the initial (< 94 g/h/mol), small amounts of methanol and increased methyl palmitate conversion could be obtained. It is noteworthy that most of the methanol produced was in the gas phase and cannot be efficiently trapped during analysis. The observed increase in methanol with the conversion suggests that the hydrogenolysis at the C-O bond of the palmitate ester was primarily promoted, presumably via the adsorbed C=O η^1 species on the Cu surface.⁹ In support of the C-O hydrogenolysis, neither methane nor palmitic acid was observed. Instead, hexadecanal and hexadecanol were primarily obtained. The lower yield of hexadecanal in comparison to hexadecanol indicate that hexadecanal serves as an intermediate, subsequently hydrogenation to form hexadecanol.

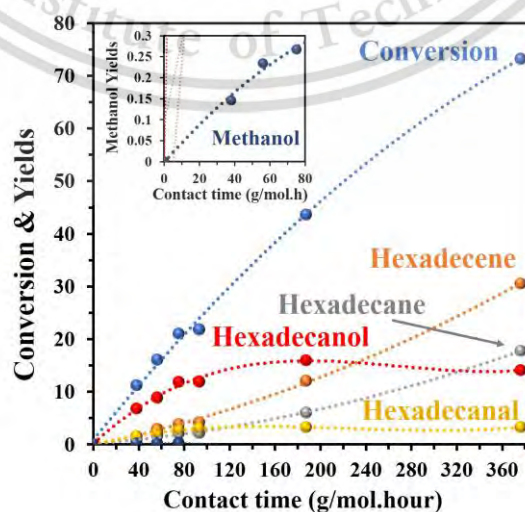


Figure 4.9 Methyl palmitate conversion and yields vs. contact time of 20CuPS catalyst.

This material is reserved for educational use only, not allowed for commercial use.

Forbidden to modify the content, and cite the document when use.

Hexadecene and hexadecane exhibit a substantial increase with conversion, while hexadecanal and hexadecanol remain relatively stable. This indicates that the primarily produced hexadecanal may undergo dehydration to form 1-hexadecene. The dehydration activity of these CuPS catalysts could be related to their acid sites, as discussed earlier. One could expect that 1-hexadecene can be further hydrogenated to hexadecane, as observed in Figure A5a. Alternatively, the hexadecane could also be produced in parallel with 1-hexadecene, as seen by a coherent increase in their selectivity (Figure 4.10). This is because the acidity also facilitates a reaction step known as "hydro-dehydration," in which protonated hexadecanol undergoes a transformation into hexadecane.¹⁵ At a high conversion (73.2%), 1-hexadecene and hexadecane were major products. In a supportive experiment, when hexadecanol is employed as the feed, only 1-hexadecene and hexadecane are generated, as shown in Figure A5b. Consequently, this could suggest that hydrodeoxygenation of methyl palmitate over CuPS catalysts is a series reaction that yields primarily hexadecanal and then hexadecanol. The hexadecanol is dehydrated to 1-hexadecene, which can be further hydrogenated to hexadecane. In parallel, the hexadecanol can also be hydro-dehydrated to hexadecane. The proposed reaction pathway is displayed in Scheme 4.2.

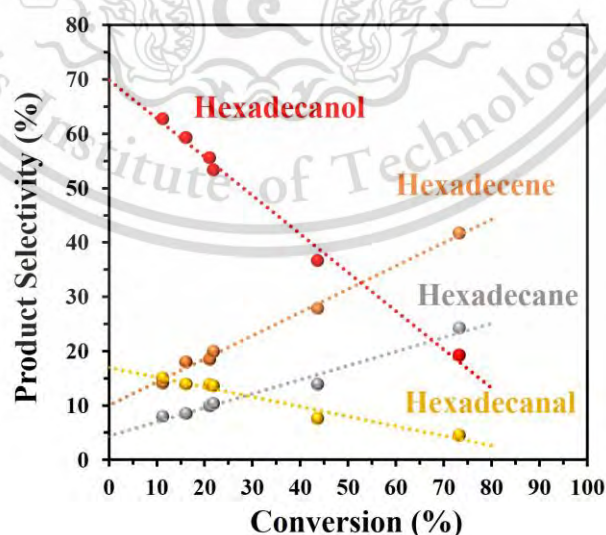
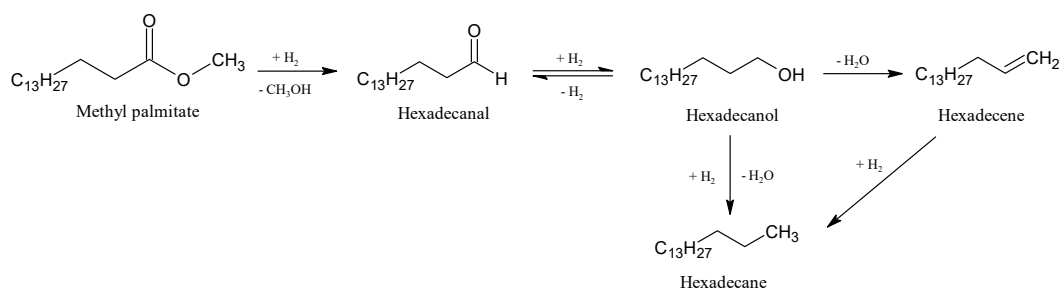


Figure 4.10 Products selectivity vs. conversion of 20CuPS catalyst; (●) Hexadecanal; (●) Hexadecanol; (●) Hexadecene; (●) Hexadecane.

This material is reserved for educational use only, not allowed for commercial use.

Forbidden to modify the content, and cite the document when use.



Scheme 4.2 Propose reaction pathway of methyl palmitate conversion over CuPS catalysts.

As the Cu content increased from 8 to 30wt.%, the conversion proportionally increased from ~20% to 77% as presented in Table 4.3, entries 2-4. The catalytic activity correlates with the active Cu surface area, as demonstrated in Figure 4.11a. This trend is also evident in the case of 20Cu/SiO₂, suggesting that the dissociation of hydrogen on the Cu surface serves as the rate-determining step for this reaction.⁶² Particularly at relatively low temperatures (~250°C), the adsorption of methyl palmitate, a polar molecule with a high molecular weight, would be facilitated, especially at the interface. The dissociation of H₂ and the subsequent spillover of hydrogen to the adsorbed methyl palmitate could be enhanced, particularly by catalysts possess a high Cu surface area, such as 30CuPS.

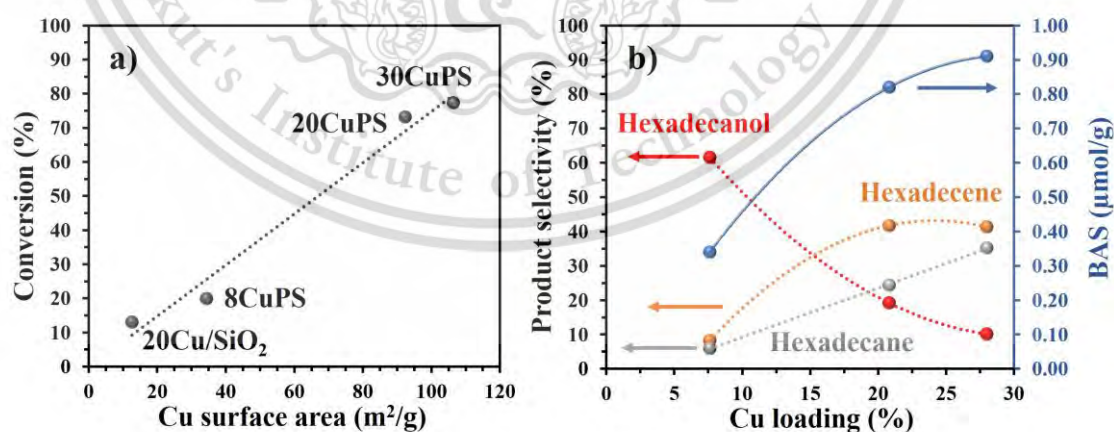


Figure 4.11 The relationship between a) conversion vs Cu surface area and b) Products selectivity and Brønsted acid sites vs Cu loadings.

Furthermore, the selectivity of 1-hexadecene and hexadecane proportionally increases with the Cu loading, as evident in Table 4.3, entries 2-4. Meanwhile, the hexadecanol selectivity was sharply decreased. This indicates that the dehydration and hydro-dehydration of hexadecanol are significantly enhanced at higher Cu loading, especially at 30wt.%. This is clearly due to the increase in Brønsted acidity of CuPS catalysts, as indicated by the inverse trend observed for hexadecanol selectivity (Figure 4.11b). As BAS at the perimeter increases, the primarily produced hexadecanol would be readily protonated and dehydrated or hydro-dehydrated to hydrocarbons, as discussed previously.

However, when the Cu loading increased from 20wt.% to 30wt.%, the hexadecene selectivity remains stable. Simultaneously, hexadecane selectivity experiences a steady increase with the 30CuPS catalyst. This could be attributed to the higher Cu surface area on the 30CuPS catalyst, resulting in a higher hydro-dehydration ability. It is important to note that the Lewis acidic Cu^+ species do not mainly play a role in alcohol dehydration. This is deduced from higher hydrocarbon selectivity over 30CuPS (~77%), as compared to that over 20CuPS (~66%), despite a similar Cu^+ content (~0.33-0.34 mmol/g) as documented in Table A2 and Lewis acidity (~4.1-4.3 mmol/g) as presented in Table 4.2. Therefore, it is suggested that only the BAS in the CuPS catalyst promotes the dehydration and hydro-dehydration of hexadecanol into linear long-chain olefins and paraffins, respectively.

As the hydrodeoxygenation of methyl palmitate is a series reaction, the product selectivity would rely on the conversion. Consequently, the product selectivity was better when CuPS catalysts were tested at the same conversion, as illustrated in Table 4.3, entries 3, 5, and 6. Even at a similar conversion (~20%), low selectivity of hexadecene was still observed for 8CuPS. This suggests that, in addition to BAS, Cu dispersion plays the role for linear long-chain α -olefin selectivity, as evident in Figure 4.12. Since the reduced 8CuPS possesses small Cu particles (high dispersion) and a high fraction of Cu^+ species as observed in Figure 4.5, hexadecanol can be readily desorbed from the surface after its formation. This is because Cu^+ is much less effective for η^1 -coordination of alcohol but interacts strongly with the feed's carbonyl group

(C=O).⁷⁷ Consequently, the presence of Cu^+ makes the competitive adsorption by the feed more sensitive, particularly on small Cu particles.⁷⁸ This combination leads to weaker adsorption of hexadecanol on such complex Cu^+ -Cu surfaces. Hence, the dehydration and hydro-dehydration of long-chain alcohol would be less effective on the small Cu particles and a high fraction of Cu^+ species.

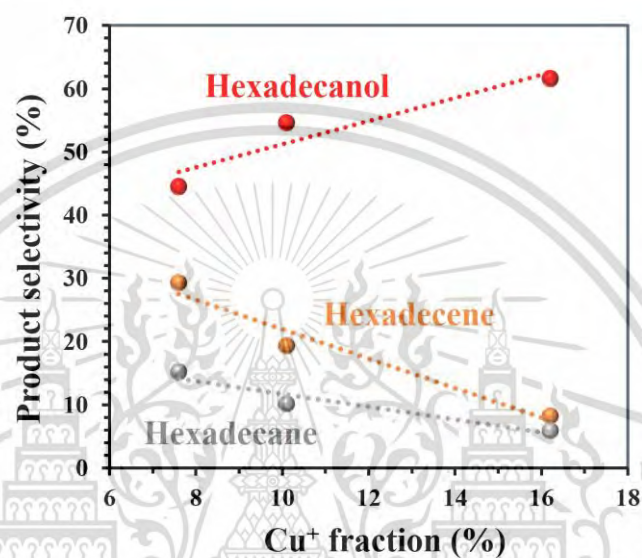


Figure 4.12 Product selectivity at 20% of conversion vs Cu^+ fractions in CuPS catalysts.

4.2 Conclusion

Copper phyllosilicate (CuPS) shows high activity for hydrodeoxygenation of methyl palmitate to linear long-chain α -olefin, i.e., 1-hexadecene. No carbon loss due to decarbonylation was observed for all CuPS catalysts. The hydrodeoxygenation activity was related to the active Cu surface area and Brønsted acid sites at the metal-support interface. *In situ* TR-XANES experiments evidence that the octahedrally coordinated $\text{Cu}^{2+}(\text{O}_h)$ species in the chrysocolla structure leads to the formation of the partially reduced Cu species (Cu^+) that exerts highly dispersed Cu particles after reduction. In addition, the co-existence of Cu^+ at the metal/support interface provides Brønsted acid sites in a closed proximity to the Cu metal particle, which promotes the dehydration of hexadecanol, primarily produced by the hydrogenation of methyl palmitate. However, the CuPS with an excessively high Cu^+ fraction was less effective

in promoting the dehydration of hexadecanol to 1-hexadecene, due to the competitive adsorption of methyl palmitate, against the hexadecanol, on the small Cu particle. Conversely, the catalyst with a low Cu^+ fraction provides larger Cu particles that promote hydro-dehydration to undesirable paraffin. The CuPS catalyst with a high number of BAS and a high Cu^0 dispersion, i.e., 20CuPS, is considered as the most effective in the hydrodeoxygenation of methyl palmitate to 1-hexadecene.



This material is reserved for educational use only, not allowed for commercial use.

Forbidden to modify the content, and cite the document when use.

Chapter 5

Tuning Cu⁺ species/Brønsted acids of Copper phyllosilicate by K⁺ doping for Selective Hydrogenation of Methyl palmitate to Hexadecanol

In this chapter, we report the study of K⁺ doped CuPS catalysts for selective hydrogenation of methyl palmitate, as a feed model, to fatty alcohols in a fixed-bed reactor under atmospheric H₂ pressure. The CuPS with 20wt.% Cu loading was doped with K⁺ (0.01-0.10 wt.%) by the impregnation method before (CuPS) and after reduction (rCuPS). The *in situ* TR-XANES, H₂-TPR, NH₃-TPD, and Py-IR were used to verify the impregnation sequence and effect of K⁺ addition on the Cu⁺/Cu⁰ species, Cu reducibility, Cu dispersion, acid sites, and BAS of the K⁺ doped CuPS catalysts. The balance of Cu⁰ and Cu⁺ species in the K⁺ doped CuPS catalyst for the hydrogenation activity was demonstrated, also the dependence of alcohol selectivity on the BAS and Cu⁺ species was highlighted. In addition, the catalytic stability of CuPS and K⁺ doped CuPS catalysts was comparatively demonstrated.

5.1 Results and discussion

5.1.1 Characterization of catalysts

The K and Cu contents in the K⁺ doped CuPS samples are listed in Table 5.1, as compared to their parent. The K⁺ loadings (0.01-0.10 wt.%) over CuPS and reduced CuPS (rCuPS) are close to the anticipated values. Due to the addition of the K⁺, the Cu content in the K⁺ doped CuPS samples (~18.7 – 18.9 wt.%) is slightly lower than their parent (CuPS and rCuPS, 19.2 wt.% Cu loading).

Table 5.1 Cu and K⁺ loading, surface area, pore size, pore volume, H₂-consumption, specific Cu surface area and Cu dispersion of all catalysts

Entry	Catalysts	Metal content		N ₂ adsorption*			H ₂ -TPR			S_{Cu}^0 (m ² /g) ^e	D_{Cu} (%) ^e
		Cu (wt.%) ^a	K (wt.%) ^b	S_{BET} (m ² /g)	D_{pore} (Å)	V_{pore} (cm ³ /g)	H ₂ consumption (mmol/g) ^c	Cu content (wt.%) ^c	Reducible Cu ²⁺ (%) ^d		
1	CuPS	19.2	-	183	126	0.58	2.80	17.8	92.7	85.2	72.9
2	0.05K-CuPS	18.8	0.046	217	117	0.64	2.70	17.1	91.0	84.7	75.2
3	0.05K-rCuPS	18.8	0.047	126	128	0.44	2.48	15.8	84.0	66.2	60.5
4	0.01K-rCuPS	18.9	0.012	159	132	0.53	2.66	16.9	89.4	74.4	64.6
5	0.10K-rCuPS	18.7	0.085	112	127	0.37	2.39	15.2	81.3	55.8	52.6

^aDetermined by XRF and ^bICP-OES, ^cEstimated by H₂-TPR, ^dEstimated by ((Cu content from XRF - Cu content from H₂-TPR)/ (Cu content from XRF)) x 100, ^eCalculated by dissociative N₂O adsorption, * Samples were reduced under H₂ at 250 °C for 2 h.

The XRD pattern of CuPS exhibited weak diffraction peaks at 30.8°, 35.0°, 57.5° and 62.4°, corresponding to the characteristic chrysocolla (Cu₂Si₂O₅(OH)₂) structure of copper phyllosilicate (Figure 5.1a, i).²² Consequently, a relatively high surface area, pore volume, and pore size of as-prepared CuPS (344 m²/g, 1.35 cm³/g, and 158 Å) can be observed (Appendix B, Table B1), as compared to conventional Cu/SiO₂ (198 m²/g, 1.03 cm³/g and 207 Å).⁷⁹ No CuO diffraction peaks could be obtained, indicating the complete formation of octahedral Cu²⁺ in the lamellar structure.⁶² Accordingly, the H₂-TPR profile of CuPS also provide a narrow distribution of the reduction peak at 233 °C (Figure 5.1b, i). This could indicate that the well-defined Cu²⁺ in the octahedral site strongly interacts with tetrahedral SiO₂ in the chrysocolla structure.²⁹ After reducing

CuPS at 250 °C for 2 h, the characteristic chrysocolla peaks were not detected on reduced CuPS (rCuPS), as depicted in Figure 5.1a. The disappearance of the chrysocolla peaks after the reduction could be ascribed to the partial deconstruction of lamellar structures, similar to those reported in the literature.²² Consequently, the surface area, pore volume, and pore size of rCuPS were decreased (183 m²/g, 0.58 cm³/g, 126 Å, Table 5.1) compared with the CuPS. Despite the high Cu loading (20 wt.%), no bulk Cu metallic phases were identified on rCuPS. This again indicates that the metallic Cu particles are highly dispersed on partially deconstructed lamellar structures of SiO₂. In a supportive manner, 73% Cu dispersion (D_{Cu}) with average Cu particle sizes \sim 3.56 nm could be observed (Table 5.1 and Figure 5.1c, Figure B1). Fine Cu particles are formed due to the strong interaction between Cu²⁺ and SiO₂ in the chrysocolla structure, as mentioned in the literature.⁸⁰

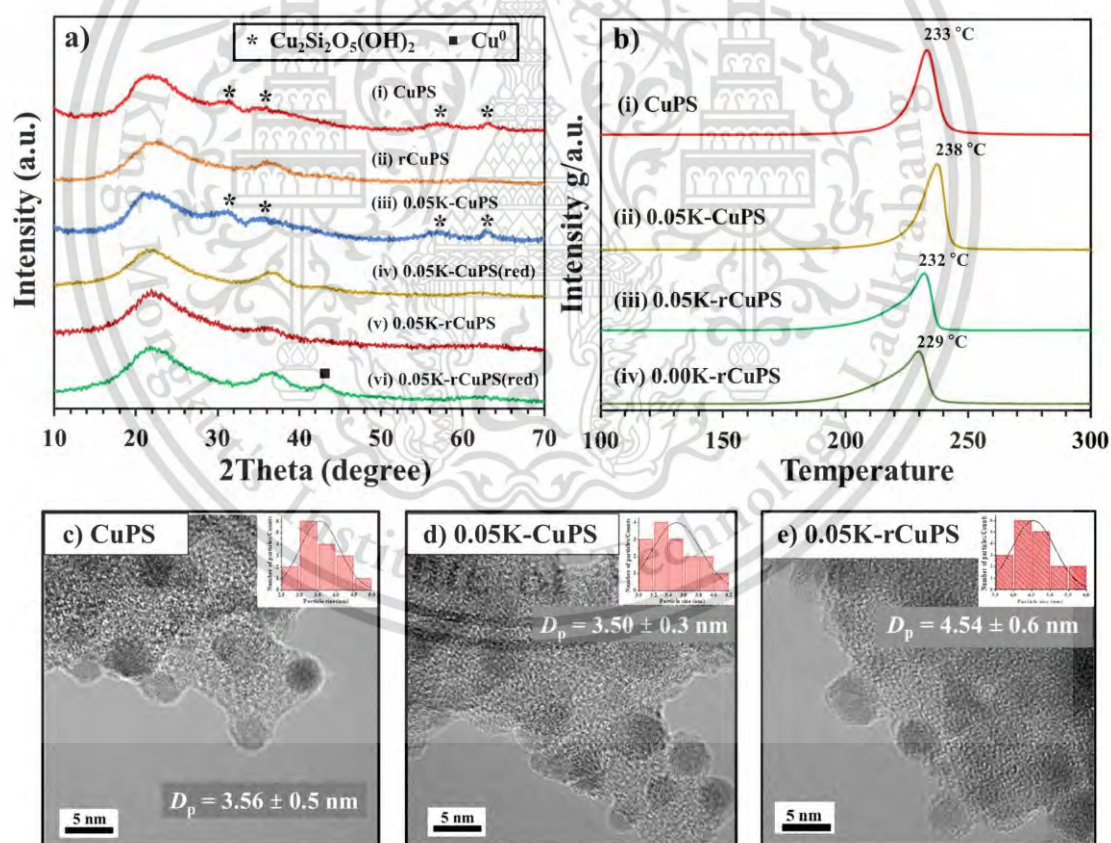
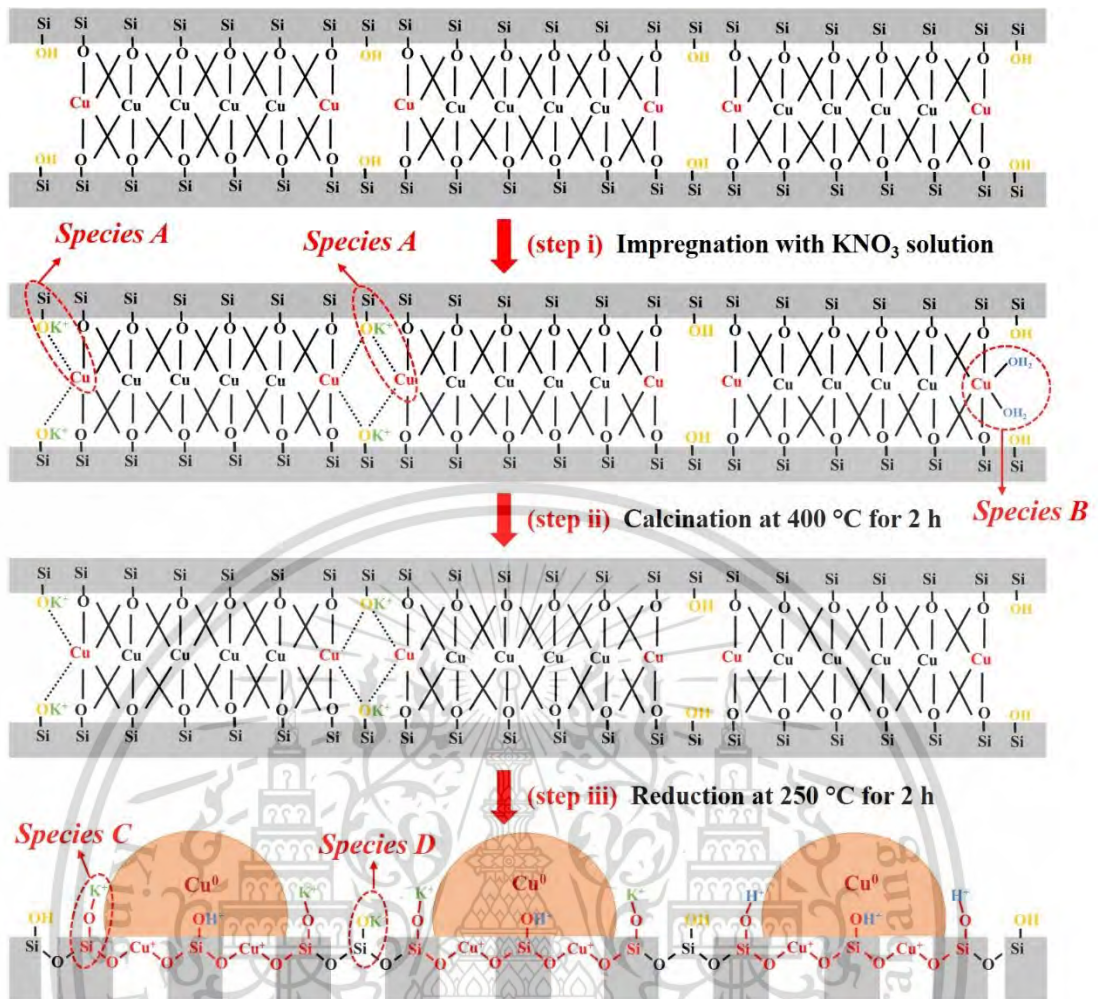


Figure 5.1 a) The XRD pattern, b) the H₂-TPR profiles, and c-e) TEM images of the CuPS samples.

After impregnation of K^+ (0.05 wt.%) into parent CuPS, no significant change in the XRD pattern was obtained after calcination (Figure 5.1a, iii). This suggests that adding K^+ on parent CuPS does not modify the chrysocolla structure. Accordingly, a similar surface area, pore volume, and pore size of 0.05K-CuPS (346 m^2/g , 1.07 cm^3/g , and 124 Å) could be obtained, as shown in Table B1. After reduction, the chrysocolla characteristic peak and Cu metallic phase were not obtained (Figure 5.1a, iv), suggesting highly dispersed Cu particles on 0.05K-CuPS, as also evidenced by 75% Cu dispersion (Table 5.1, Figure B1) with average Cu particles sizes (~3.50 nm, Figure 5.1d). In addition, the surface area, pore volume, and pore size of 0.05K-CuPS (217 m^2/g , 0.64 cm^3/g , and 117 Å) are in the same range as rCuPS (Table 5.1).

Although the H_2 -TPR profile of 0.05K-CuPS (Figure 5.1b, ii) provide a narrow distribution similar to the parent CuPS, the 0.05K-CuPS has a higher reduction temperature (238 °C). This could imply that the K^+ might affect the reducibility of Cu^{2+} species in the lamellar structure. Interestingly, adding the K^+ into CuPS also causes lower H_2 consumption (Table 5.1), inferring the lower reducibility of the Cu^{2+} species. According to Table 5.1, only 91% of Cu^{2+} in 0.05K-CuPS could be reduced. It is known in the literature that after reduction, Cu^+ species are retained in the CuPS due to the strong interaction between Cu^{2+} in the octahedral hole and the SiO_2 lamella network.²⁷ It is possible that the doped K^+ could react with the Si-OH network, forming highly polarizable silicate species (Si-O- K^+) that interact more strongly with Cu^{2+} (Scheme 5.1, species A). The silicate of these species would have a greater anionic character, leading to a higher cationic character of Cu^{2+} . Hence, the lower electron density at the Cu^{2+} would be expected. In addition, the slightly higher Cu edge energies of 0.05K-CuPS after impregnation (8991.44 eV) and calcination (8991.16 eV) were obtained by XANES, as compared to its parent without K^+ (8990.95 eV, Figure 5.2). This indicates the lower electron density of Cu^{2+} in the 0.05K-CuPS than CuPS.⁸¹ Consequently, a higher reduction temperature and a higher fraction of Cu^+ species would be expected after K^+ doping.



Scheme 5.1 The demonstration of K^+ doping on CuPS forming 0.05K-CuPS.

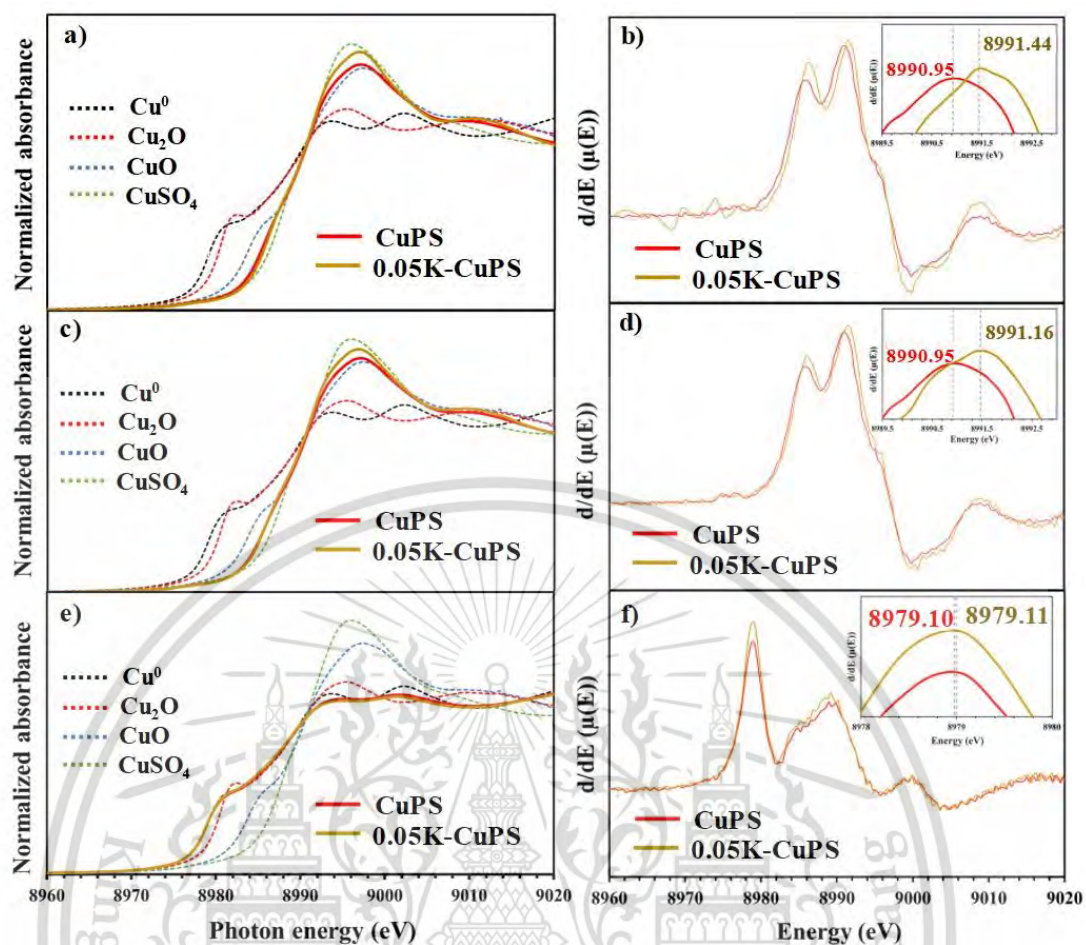


Figure 5.2 XANES spectra of CuPS and 0.05K-CuPS after a) impregnation c) calcination and e) reduction, The first derivative of CuPS and 0.05K-CuPS after b) impregnation d) calcination and f) reduction.

To understand the role of K^+ on electron density and reducibility of Cu^{2+} in 0.05K-CuPS, the Cu edge energy was further verified by the *in situ* XANES. According to the LCF of *in situ* TR-XANES spectra in Figure 5.3, the parent CuPS is initially composed of 51.4% (Figure 5.4a) of octahedral Cu^{2+} species ($Cu^{2+}(O_h)$).⁷⁹ After impregnation with K^+ , $Cu^{2+}(O_h)$ fraction increases to 64.6%, presumably due to the formation of $Si-O(K)\cdots Cu$ species (scheme 5.1, species A) and the coordination of water with $Cu^{2+}(Sq)$ to form species B in scheme 5.1. During the calcination from 50 °C to 400 °C of 0.05K-CuPS, the $Cu^{2+}(O_h)$ fraction was gradually decreased with an increase of $Cu^{2+}(Sq)$ fraction, suggesting the transformation of $Cu^{2+}(O_h)$ to $Cu^{2+}(Sq)$.⁷⁹ It is probably due to the coordinated H_2O in species (Species B) is removed upon calcination, resulting in a lower

$\text{Cu}^{2+}(\text{O}_h)$ fraction. Nevertheless, the remaining $\text{Cu}^{2+}(\text{O}_h)$ in 0.05K-CuPS (58.3%, Figure 5.3) is higher than those of parent CuPS (51.4%), emphasizing the interaction between K^+ and Cu^{2+} (species A) in this sample.

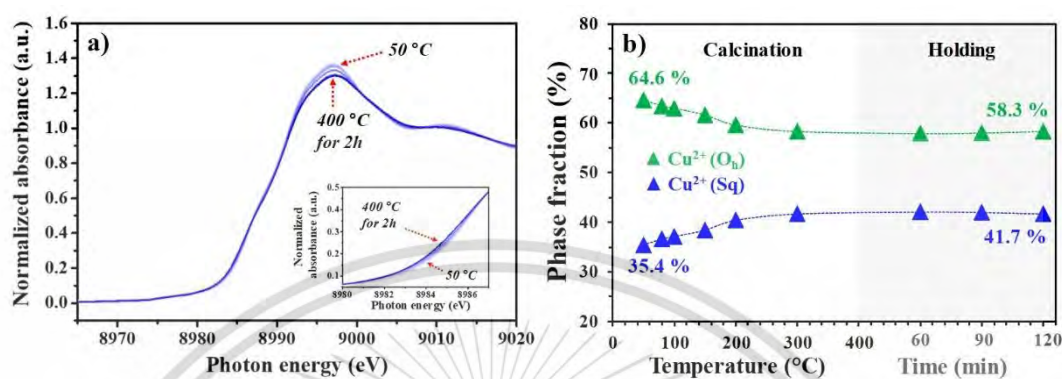


Figure 5.3 a) *in situ* TR-XANES spectra of 0.05K-CuPS during the calcination and b) linear combination fitting (LCF); (\blacktriangle) $\text{Cu}^{2+}(\text{O}_h)$; (\blacktriangle) $\text{Cu}^{2+}(\text{Sq})$.

The transformation of $\text{Cu}^{2+}(\text{O}_h)$ to $\text{Cu}^{2+}(\text{Sq})$ species in 0.05K-CuPS was continuous under the reduction condition, similar to those of parent CuPS (Figure 4a and b). This behavior was ascribed to the hydrogen dissociation over Si-O-Cu-O-Si in $\text{Cu}^{2+}(\text{O}_h)$ species, forming internal Si-OH and H-Cu-O-Si (Scheme 5.2). The latter species may react with the adjacent HO-Cu-O-Si, liberating H_2 and Cu-O-Cu, which is the component of $\text{Cu}^{2+}(\text{Sq})$ species.^{65, 79} The hydrogen-assisted transformation of $\text{Cu}^{2+}(\text{O}_h)$ to $\text{Cu}^{2+}(\text{Sq})$ over 0.05K-CuPS (Figure 5.4b) also motivates the initial reduction of Cu^{2+} to Cu^+ in 0.05K-CuPS (180 °C) as compared to those of CuPS (210 °C). This observation is also in line with the H_2 -TPR results in Figure 5.1b and Figure B2, showing the lower initial reduction temperature of 0.05K-CuPS compared to CuPS. Due to the fluxing ability of K^+ , the CuO ($\text{Cu}^{2+}(\text{Sq})$) layers would be easily reduced to Cu^+ species.⁸² Though, the Cu^+ fraction in 0.05K-CuPS (11.5%, Figure 5.4) is higher than those of CuPS (10.1%), indicating that the doped K^+ could stabilize the Cu^+ species.⁸³ This observation is consistent with the lower H_2 consumption of 0.05K-CuPS, as discussed earlier. It is possible that after the reduction, the doped K^+ would be at the perimeter (species C, D), leading to the stronger interaction of Cu-SiO₂ due to the higher polarizable of Si-O(K)··Cu species. Therefore, the doped K^+ over CuPS does not only promote the reduction of Cu^{2+} to Cu^+ , but it also stabilizes the Cu^+ species. Accordingly, the

reduction of Cu^+ to Cu^0 occurs at a higher temperature, as shown in H_2 -TPR (Figure 5.1b). The higher Cu^+ remaining in the support (Table B2) also strongly interacts with the metallic Cu, resulting in the higher Cu dispersion in 0.05K-CuPS, as discussed above.

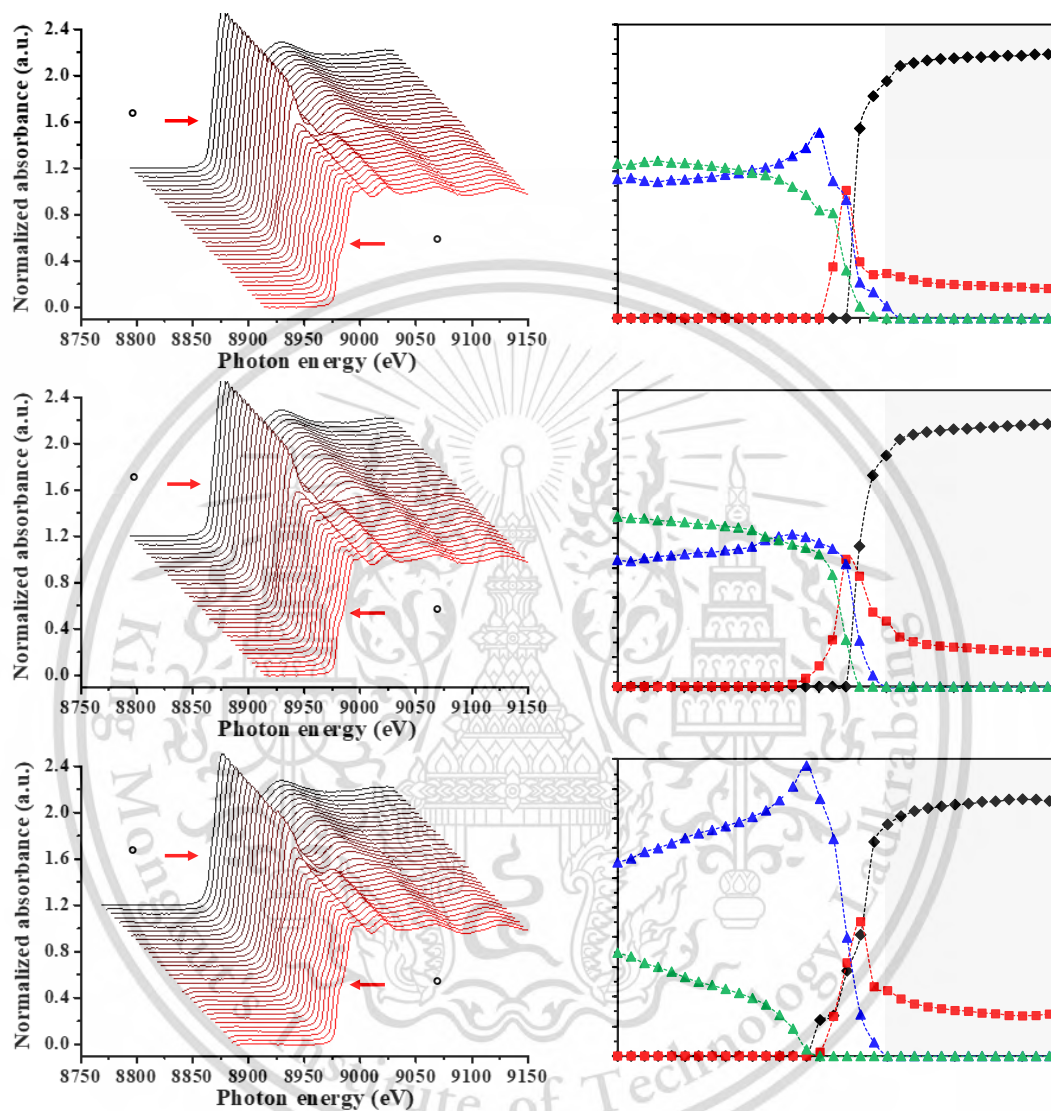
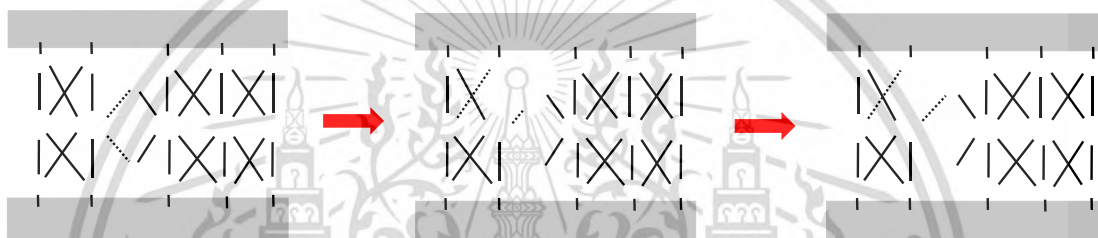


Figure 5.4 The *in situ* TR-XANES spectra during reduction of a) CuPS b) 0.05K-CuPS c) 0.05K-rCuPS and the linear combination fitting of a) CuPS and b) 0.05K-CuPS and c) 0.05K-rCuPS; (◆) Cu^0 ; (■) Cu^+ ; (▲) Cu^{2+} (Square planar); (▲) Cu^{2+} (Octahedral).

Conversely, the impregnation of K^+ over reduced CuPS (0.05K-rCuPS) yielded a larger Cu particle. The metallic Cu phase was detected in the XRD of 0.05K-rCuPS (Figure 5.1a, vi), while it was not obtained in the parent rCuPS (Figure 5.1a, ii). The

reoxidation and agglomeration of Cu particles after the impregnation of K^+ leads to larger Cu particles. The vivid color change from dark black to dark green was observed after K^+ impregnation, hinting at the reoxidation of Cu^0 . Additionally, a broad reduction peak at 232 °C with H_2 consumption of ~15.8 wt.% Cu could be observed for 0.05K-rCuPS (Figure 5.1b, iii), even though the sample was reduced before the impregnation. The reoxidation of rCuPS could be observed even using only distilled water (0.00K-rCuPS) for the impregnation (Figure 5.1b, iv). This is presumably because exposing the fine Cu particle (< 3.5 nm) with electrolyte/water in the air could readily oxidize metallic Cu^0 to CuO aggregates.⁸⁴

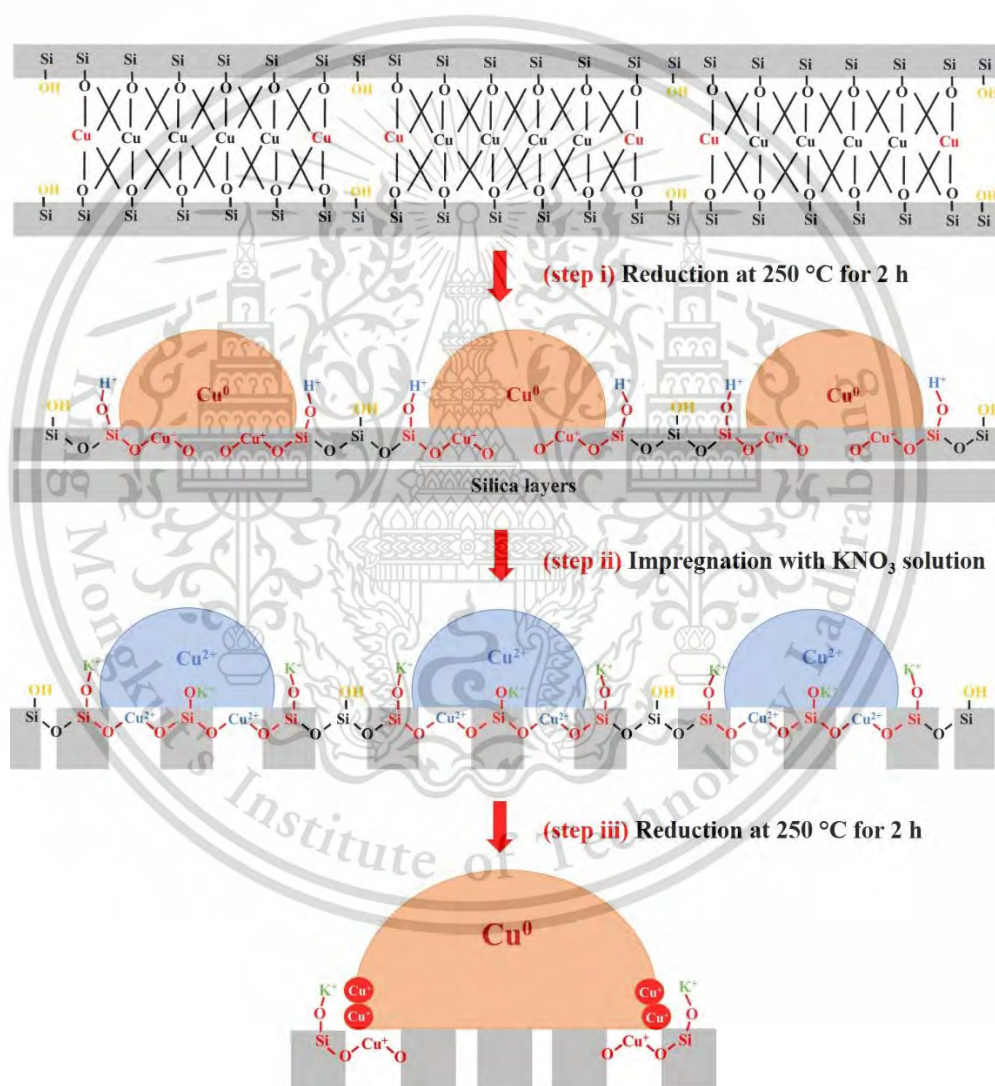


Scheme 5.2 The change of coordination on $Cu^{2+}(O_h)$ to $Cu^{2+}(Sq)$ during reduction under H_2 atmospheres.

The formation of CuO ($Cu^{2+}(Sq)$) in 0.05K-rCuPS was also evidenced by the *in situ* XANES in Figure 5.4c and Figure B3. After the impregnation of K^+ into rCuPS, the Cu edge energy of 0.05K-rCuPS is 8991.25 eV (Figure B3), corresponding to only Cu^{2+} . Unlike 0.05K-CuPS and CuPS, the higher fraction of $Cu^{2+}(Sq)$ species (67.7 %, Figure 5.4c) were initially presented in this sample (noted $Cu^{2+}(Sq)$ species for 0.05K-CuPS (41.6%), and CuPS (48.6%)). The complete formation of $Cu^{2+}(Sq)$ was observed at 190 °C. This supports the reoxidation of metallic Cu to CuO aggregates ($Cu^{2+}(Sq)$), as shown in Scheme 5.3, step ii. Interestingly, upon increasing the temperature under H_2 , the metallic Cu^0 was initially observed at a relatively lower temperature (200 °C, Figure 4c) than others (230 °C for 0.05K-CuPS and CuPS). This could be attributed to the ready reduction of $Cu^{2+}(Sq)$ on the surface of CuO aggregates. In line with this view, the lower initial reduction temperature (~170 °C) was detected in the H_2 -TPR profiles of 0.05K-rCuPS and 0.00K-rCuPS (Figure 5.1b), clearly indicating the surface reduction. Moreover, the facile reduction of CuO aggregates may be promoted by the doped K^+ as a fluxing agent (Scheme 5.3, step iii). In a supportive manner, the TEM image of 0.05K-rCuPS

This material is reserved for educational use only, not allowed for commercial use.

showed larger Cu particle sizes of ~ 4.54 nm, as compared to 0.05K-CuPS and CuPS (Figure 1). Thus, a lower Cu dispersion (D_{Cu} , ~ 60.5 %) was obtained (Table 5.1, Figure 5.1e and Figure B1), together with a much lower surface area, pore volume and pore size (126 m²/g, 0.44 cm³/g and 128 Å, Table 5.1). It is worth noting that the Cu particles of 0.05K-rCuPS (4.54 nm, Figure 5.1e) are larger than those of 0.00K-rCuPS (~ 4.04 nm, Figure B4). This could imply that the doped K^+ over the reduced CuPS (rCuPS) may additionally promote the agglomeration of the Cu particles due to the fluxing ability of the doped K^+ .



Scheme 5.3 The demonstration of K^+ doping on rCuPS forming 0.05K-rCuPS.

Despite the larger Cu particle size of 0.05K-rCuPS, the higher fraction of Cu^+ (14.1%, Figure 5.4c) was observed over this sample after the reduction at 250 °C for 2 h, as compared to 0.05K-CuPS (11.5%) and CuPS (10.1%). Even though K^+ , especially

This material is reserved for educational use only, not allowed for commercial use.

at the CuO perimeter (Scheme 5.3, step iii), could facilitate Cu reduction by providing more electron density at the CuO-SiO₂ interface, an increased electron density would also stabilize the Cu⁺ species at the perimeter of large Cu metal particles formed (Table B2). Therefore, a lower H₂ consumption from H₂-TPR of 0.05K-rCuPS (2.48 mmol/g, Table 5.1) was obtained compared with 0.05K-CuPS (2.70 mmol/g).

As the higher Cu⁺ remained in 0.05K-rCuPS, the higher Lewis acid was obtained in the *in situ* pyridine-adsorbed infrared spectroscopy (*in situ* Py-IR, Figure 5.5a and Table 5.2), as compared to 0.05K-CuPS and CuPS. In fact, the Lewis acid (deriving from Cu⁺ species) evaluated by the peak at 1450 cm⁻¹ of *in situ* Py-IR is in the order of 0.05K-rCuPS < 0.05K-CuPS < CuPS (Figure 5.5a). In line with this view, the Brønsted acid at the Cu perimeter (1530 cm⁻¹) significantly decreases upon doped K⁺, especially over the rCuPS (CuPS < 0.05K-CuPS < 0.05K-rCuPS) since the Cu⁺ was stabilized by the K⁺ at the perimeter of metallic Cu particles forming Si-OK (Scheme 5.3 step iii). This results in the relatively low Brønsted acid sites (BAS), as compared to the doped K⁺ over CuPS and CuPS in which the BAS are mainly promoted after the reduction (Scheme 5.1 step iii and Scheme 5.3 step i).³¹ Indeed, the NH₃-TPD profiles evidenced a decrease in total acidity, especially the weak acid sites (Figure 5.5b and Table 5.2) in the order of CuPS > 0.05K-CuPS > 0.05K-rCuPS.

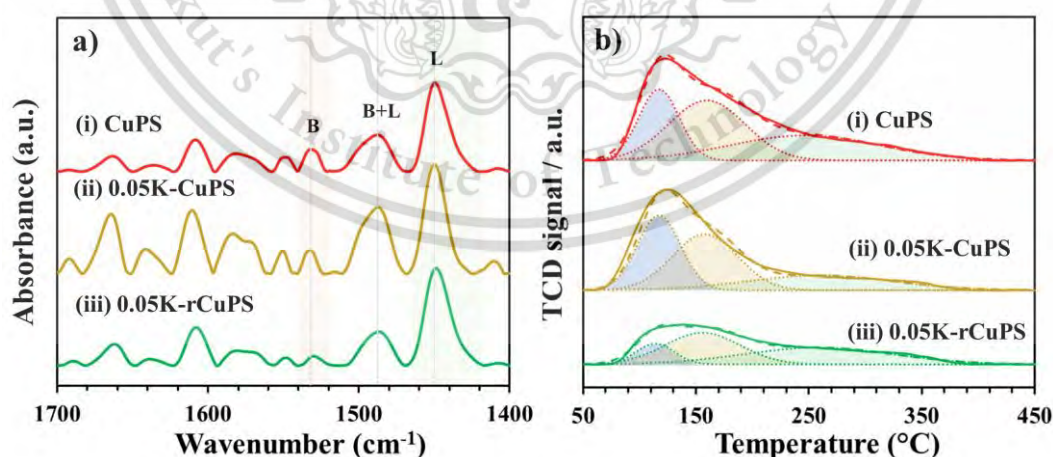


Figure 5.5 Acidity of CuPS, 0.05K-CuPS and 0.05K-rCuPS, a) the *in situ* pyridine-adsorbed infrared spectra (Py-IR) and b) NH₃ temperature-programmed desorption (NH₃-TPD).

Table 5.2 Acidity and type of acid sites of all catalysts.

Entry	Catalyst	Acidity ($\mu\text{mol/g}$) ^a				Type of acid site ($\mu\text{mol/g}$) ^b		LAS/Cu ⁺ ($\times 10^{-2}$)	BAS/Cu ₂ ⁰ ($\times 10^{-4}$)
		Weak acid sites- External silanol (120 °C)	Medium acid sites- Cu surface (175 °C)	Strong acid sites- Internal silanol (250 °C)	Total acidity	Lewis acid (LAS)	Brønsted acid (BAS)		
1	CuPS	7.1	11.4	9.3	27.8	4.08	0.82	1.34	4.1
2	0.05K-CuPS	6.8	9.1	6.6	22.5	4.69	0.71	1.38	3.6
3	0.05K-rCuPS	1.7	5.2	5.4	12.3	4.89	0.33	1.17	2.1

^a The acidity was evaluated by NH₃-TPD. ^b The Brønsted and Lewis acid was calculated via *in situ* infrared spectroscopy of pyridine adsorption (Py-IR).

5.1.2 Catalytic activity

The activity of methyl palmitate hydrogenation over the K⁺ doped CuPS catalysts was evaluated in the continuous fixed-bed reactor at 250 °C under atmospheric H₂, compared to the parent CuPS. At the contact time of 374 g.h/mol, the CuPS catalyst shows a conversion of 73%, yielding mainly hexadecene (30%) and hexadecane (18%) with hexadecanol (14%) and hexadecanal (3%) as minor products (Figure 5.6). None of the decarbonylation and decarboxylation products were obtained over this catalyst. As reported previously,⁷⁹ CuPS provides the series hydrogenation-dehydration of methyl palmitate to hexadecanol and C16 hydrocarbons, as shown in Scheme 5.4. The hydrogenation of methyl palmitate first takes place at C=O ester to form hexadecanal, which is then hydrogenated to hexadecanol. Due to the presence of Brønsted acid over CuPS, hexadecanol can undergo dehydration, yielding hexadecene as a main product. Also, CuPS can further hydrogenate hexadecene to hexadecane.

with the higher Cu^+ species retained in the samples, as shown in Figure 5.7a and 5.7b. The presence of Cu^+ species has been reported to interact preferentially with the $\text{C}=\text{O}$ of an ester,⁸⁵ acting as a Lewis acid site for better methyl palmitate adsorption. Consequently, the conversion clearly depends on the amount of Cu^+ species shown in Figure 5.7b.

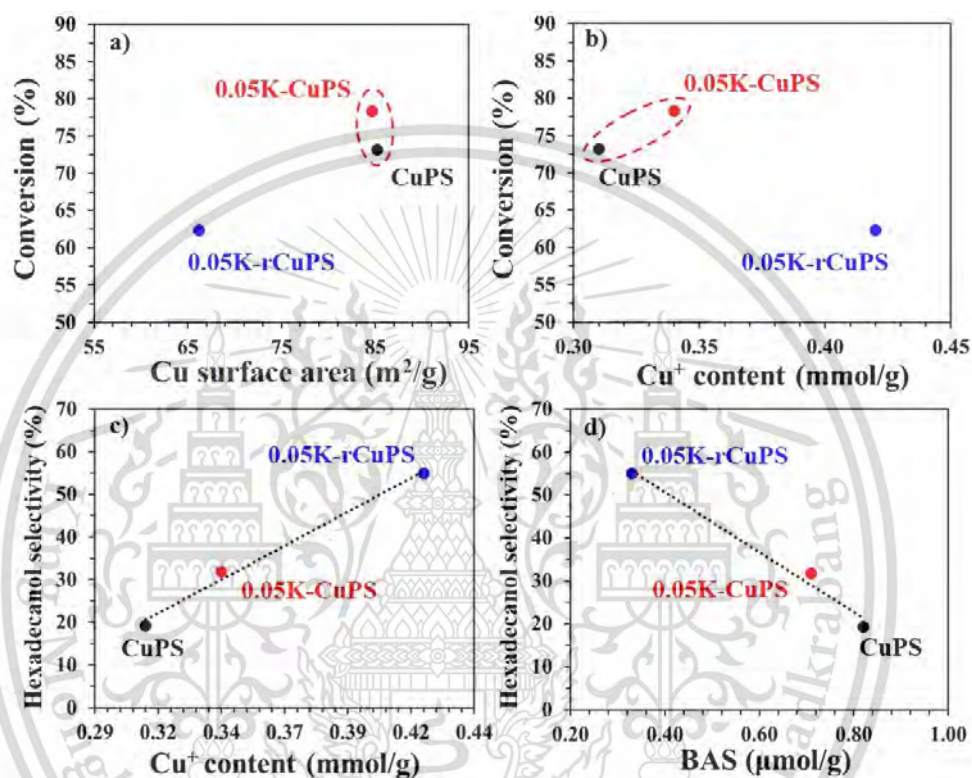


Figure 5.7 The relationship between conversion Vs. a) specific Cu surface area and b) Cu^+ content and the relationship between hexadecanol selectivity Vs. c) Cu^+ content and d) BAS.

However, the methyl palmitate conversion over 0.05K-rCuPS (62.3%, Figure 5.7a) is lower than those of 0.05K-CuPS and CuPS (Figure 5.6 and Figure 5.7b), despite a higher Cu^+ content. This is mainly derived from the lower specific Cu surface area (66.2 m²/g) due to the agglomeration of Cu particles, as discussed earlier. Fewer metallic Cu active sites would limit the H_2 -dissociation and H_2 -spillover, leading to a lower hydrogenation activity. Consequently, the balance between Cu^0 and Cu^+ species in the CuPS-based catalyst plays a crucial role in hydrogenation activity, similar to those reported in the literature.⁸⁶

This material is reserved for educational use only, not allowed for commercial use.

Forbidden to modify the content, and cite the document when use.

A significant increase in hexadecanol selectivity was observed over 0.05K-rCuPS (55%, Figure 5.6), as compared to 0.05K-CuPS (32%) and CuPS (19%). This could be attributed to the higher Cu^+ content in this catalyst, as obtained by the linear relationship between the hexadecanol selectivity and Cu^+ content (Figure 5.7c). As the Cu^+ content increased, the re-adsorption and dehydration of hexadecanol, primarily produced by the hydrogenation of methyl palmitate, was suppressed. This observation is similar to our previous publication, showing that the hexadecanol selectivity depends on the amount of Cu^+ retained in the CuPS catalysts.⁷⁹ Furthermore, the re-adsorption and dehydration of hexadecanol are discouraged due to the limited number of BAS in 0.05K-rCuPS, as seen by the proportional increase in hexadecanol selectivity with the decrease in BAS (Figure 5.7d). In line with this view, the yields of products produced from hexadecanol conversion (hexadecene and hexadecane) over 0.05K-rCuPS are lower than those of 0.05K-CuPS and CuPS (Figure 5.6).

One could expect that higher hexadecanol selectivity over 0.05K-rCuPS may result from a lower MP conversion. However, at relatively the same conversion (~80%), 0.05K-rCuPS still provided higher hexadecanol selectivity (~40%) than 0.05K-CuPS (~30%) and other SiO_2 -supported Cu catalysts, as seen in Table 5.3. This again suggests that the K^+ doping over rCuPS (0.05K-rCuPS) causes the reoxidation of Cu particles, leading to a higher Cu^+ content (Figure 5.4, Table B2) with the lower number of BAS (Figure 5.5, Table 5.2) at Cu perimeter after reduction as discussed earlier. The critical role of Cu^+ and BAS content determining hexadecanol selectivity was also observed in CuPS with the difference of Cu loading over a range of conversion (from 30CuPS to 20CuPS and 8CuPS, Table 5.3 and Figure 5.8).⁷⁹ As the catalysts with the lower Cu loading contained higher Cu^+ content with lower BAS, the hexadecanol selectivity was improved. Since hexadecanol is an intermediate in a series reaction, as discussed earlier (Scheme 5.4), its selectivity would be decreased at higher conversion for all catalysts. Nevertheless, the K^+ doping on rCuPS (0.05K-rCuPS) provides a higher hexadecanol selectivity at high conversion compared with others, especially 20CuPS (Figure B5).

Table 5.3 Fatty alcohol selectivity from ester hydrogenation over various Cu-based catalysts.

Entry	Catalyst	W/F	Conversion	Fatty alcohol	Ref.
		(g.h/mol)	(%)	Selectivity (%)	
1	0.05K-rCuPS	582	81.0	40.0	This work
2	0.05K-CuPS	374	78.3	31.8	This work
3	20CuPS	374	73.2	19.2	[2]
4	30CuPS	374	77.3	10.1	[2]
5	20Cu/SiO ₂	4478	74.0	22.6	This work

Note: Feed methyl palmitate, fixed-bed reactor at 250 °C, atmospheric H₂ pressure, initial data at 1 h on stream.

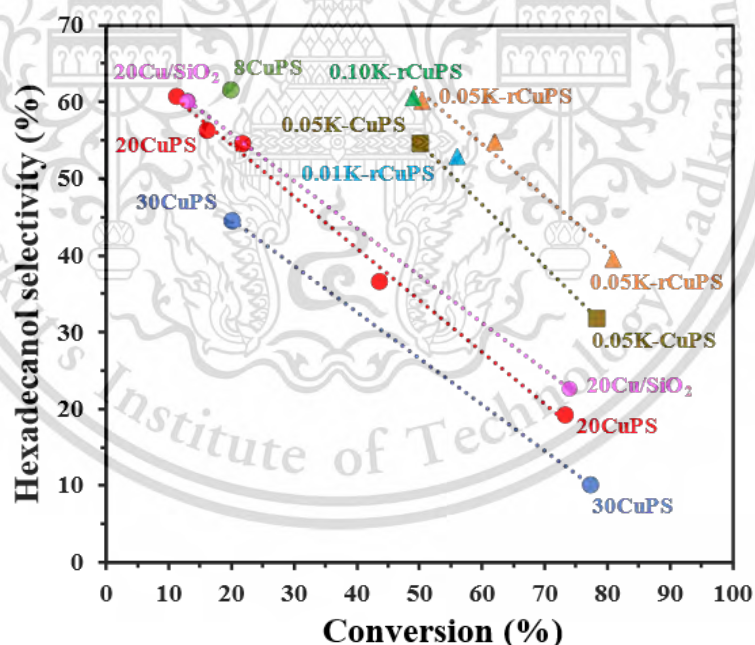


Figure 5.8 Conversion and hexadecanol selectivity over various CuPS based catalysts and impregnated Cu/SiO₂ catalyst.

The effect of K⁺ loading (0.01 to 0.10 wt.%) over the reduced CuPS was further verified, as displayed in Table 5.4. At 0.01 wt.% K⁺ loading, 0.01K-rCuPS showed a lower conversion than 0.05K-rCuPS (Figure 5.9a). The observed decrease in hydrogenation

activity of 0.01K-rCuPS could be attributed to the lower Cu⁺ species (10%, Figure 5.10a) compared to 0.05K-rCuPS (14.1%, Figure 5.4c). This is due to the lower number of K⁺ to stabilize the Cu⁺ species after the reduction. Even though the Cu dispersion and specific Cu surface area of 0.01K-rCuPS are higher than those of 0.05K-rCuPS (Table 5.1 entries 3 and 4, Figure 5.9a), presumably due to the lower redispersion of CuO. The addition of only 0.01wt.% K ineffectively reduces acidity and the number of BAS, as shown in Figure 5.11a, 5.11b, and Table B3. Accordingly, the lower Cu⁺ content and the higher BAS in 0.01K-rCuPS also lead to lower hexadecanol selectivity despite the lower conversion (Figure 5.9b).

Table 5.4 Catalytic activity and product yields in hydrogenation of methyl palmitate over K⁺ doped catalyst

Entry	Catalyst	W/F (g,h/mol)	Conversion (%)	Product yields, % (Product selectivity, %)			
				Hexadecene	Hexadecane	Hexadecanal	Hexadecanol
1	0.01K-rCuPS	374	56.0	7.5 (13.4)	4.5 (8.0)	7.6 (13.6)	29.6 (52.9)
2	0.05K-rCuPS	374	62.3	8.2 (13.2)	4.3 (7.0)	7.2 (11.6)	34.2 (54.9)
3	0.10K-rCuPS	374	49.0	4.6 (9.4)	2.6 (5.3)	6.6 (13.5)	29.7 (60.6)
4	0.05K-rCuPS	278	50.4	4.3 (8.5)	2.3 (4.6)	6.2 (12.3)	30.3 (60.1)

Note: 10 wt. % Methyl palmitate in dodecane, reaction temperature at 250 °C, activation temperature at 400 °C, reduction temperature at 250 °C, H₂ 1 atm (180 mL/min). The activity is at 1 h on stream.

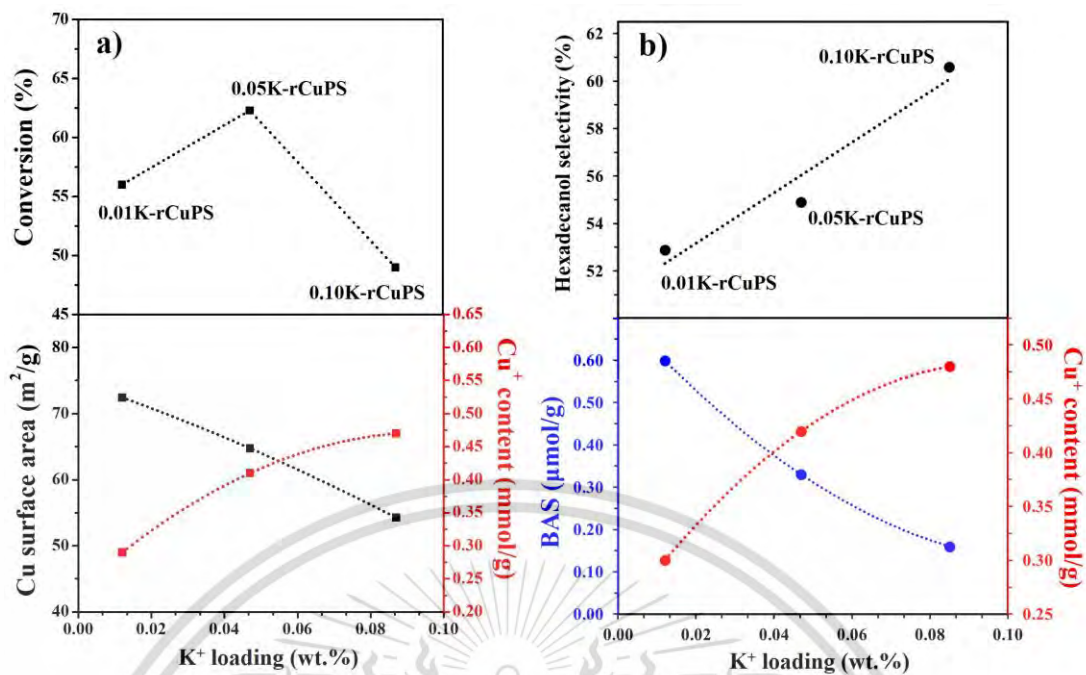


Figure 5.9 Relationship between K⁺ loading with a) conversion, specific Cu surface area and Cu⁺ content b) hexadecanol selectivity, BAS and Cu⁺ content.

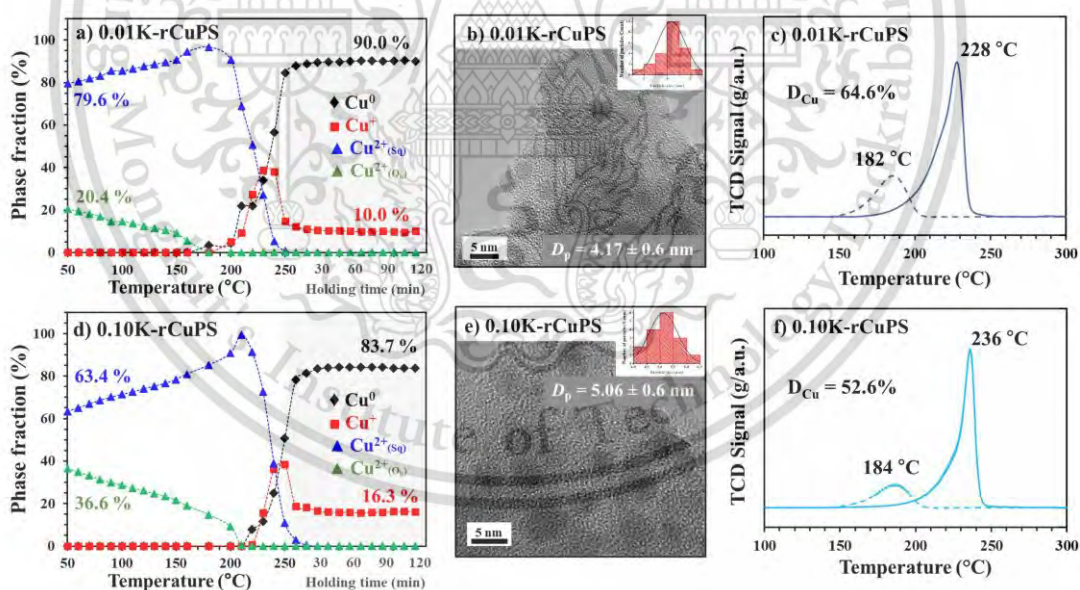


Figure 5.10 The LCF of *in situ* TR-XANES spectra of a) 0.01K-rCuPS d) 0.10K-rCuPS, TEM of b) 0.01K-rCuPS and e) 0.10K-rCuPS, the H₂-TPR profiles of c) 0.01K-rCuPS and f) 0.10K-rCuPS.

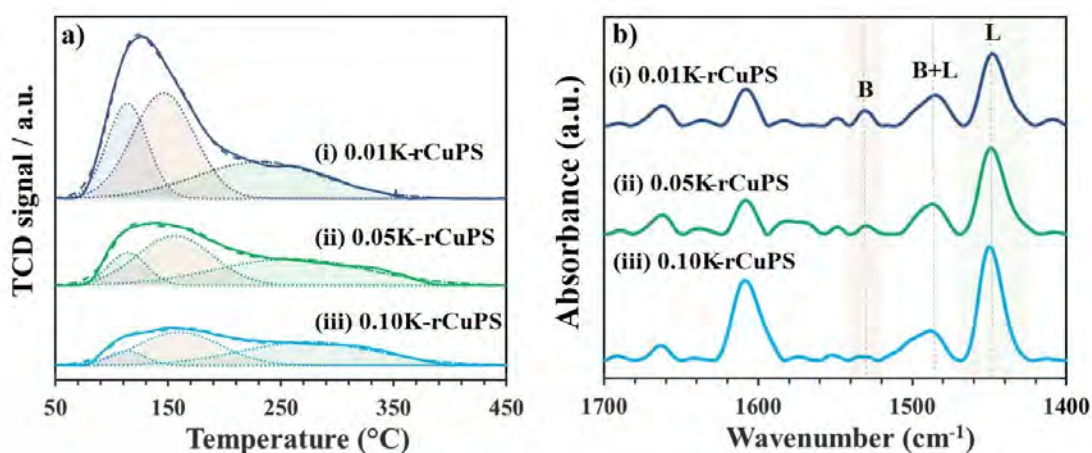


Figure 5.11 The total acidity from a) NH_3 -TPD and b) *in situ* pyridine-adsorbed infrared spectra (Py-IR) of 0.01K-rCuPS, 0.05K-rCuPS and 0.10K-rCuPS.

Even though the increase of K^+ loading to 0.10 wt.% resulted in the higher Cu^+ species (~16.3%, Figure 5.10d), the conversion of 0.10K-rCuPS (49.0%) is significantly dropped compared with 0.05K-rCuPS (62.3%). This is derived from the fact that the Cu dispersion and specific Cu surface area of 0.10K-rCuPS (Figure 5.10) are lower than those of 0.05K-rCuPS and 0.01K-rCuPS (Table 5.1, Figure 5.9a). The K^+ loading at 0.10 wt.% could lead to the agglomeration of CuO particles during the reoxidation, leading to larger Cu particle size, as exhibited in Figure 5.10e. In a supportive manner, a higher reduction temperature was detected in the H_2 -TPR (Figure 5.10f). Due to the decrease in the conversion of 0.10K-rCuPS, the hexadecanol selectivity is increased, as shown in Figure 5.9b. However, at the same level of conversion (Table 5.4, entries 3 and 4), the hexadecanol selectivity over 0.10K-rCuPS is similar to that over 0.05K-rCuPS. This suggests that when the K loading is ≥ 0.05 wt.%, the observed change in the hexadecanol selectivity entirely depends on the conversion. Manipulated by K^+ doping over rCuPS, the balance between the specific Cu surface area and Cu^+ content can be tuned for the optimal hydrogenation activity, while the hexadecanol selectivity can be regulated by the Cu^+ and BAS, as displayed in Figure 5.9.

The addition of K^+ does improve not only the hexadecanol selectivity but also the stability of the catalyst. As obtained in Figure 5.12, 0.05K-rCuPS shows a steady yield of hexadecanol up to 5 h on stream. While the CuPS catalyst initially gives a lower yield of hexadecanol that gradually increases with time on stream. This could

This material is reserved for educational use only, not allowed for commercial use.

be attributed to the higher BAS of the CuPS, which initially promoted the formation of C_{16} hydrocarbons. However, these acid sites are prone to be deactivated, not by the coke formation but rather by the adsorption of such hydrocarbon products. This is deduced from a weight loss at a low temperature (~ 270 °C) of the spent catalyst, as shown in Figure B6. Therefore, the adsorption of products on the acid sites could result in a lower dehydration activity,⁸⁷ and the C_{16} hydrocarbon yield is decreased with time on stream (Figure 12a). For 0.05K-rCuPS, on the other hand, this catalyst possesses a lower BAS, as discussed earlier (Figure 5.5a, Table 5.2). Therefore, lower C_{16} hydrocarbons can be obtained, leading to better stability with more selective hexadecanol production from methyl palmitate compared to those reported in the literature (Table 5.5).⁸⁸⁻⁹¹

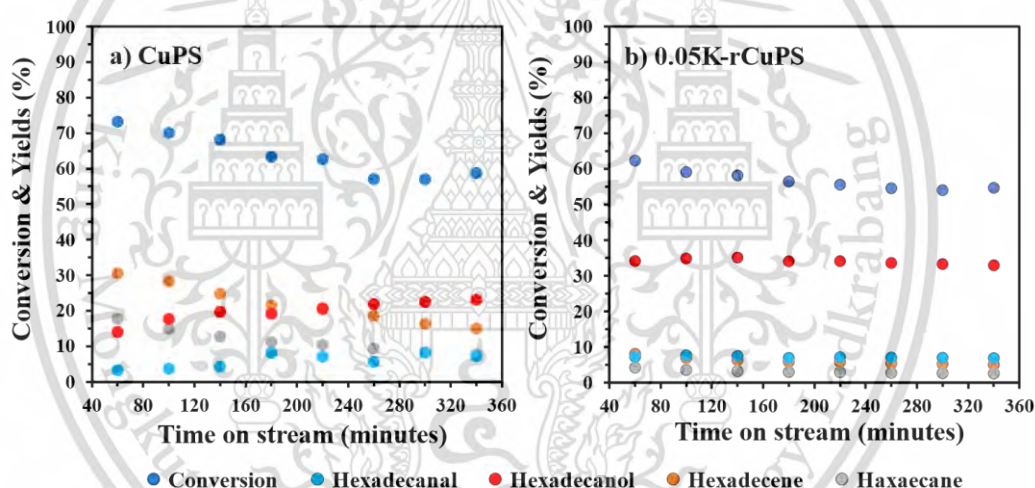


Figure 5.12 The catalytic stability of a) CuPS and b) 0.05K-rCuPS over 5 hours of time on steam at $374 \text{ g} \cdot \text{h}/\text{mol}$ of contact time.

Table 5.5 Fatty alcohol selectivity from gas phase conversion of methyl palmitate in the fixed-bed reactor over various catalysts

Entry	Catalyst	WHSV (h^{-1})	Temp. (°C)	H_2 Pressure (atm)	Conversion (%)	Fatty alcohol Selectivity (%)	Hydrocarbon Selectivity (%)	Ref.
1	0.05K-rCuPS	1	250	1	62.3	54.9	20.0	This work
2	$\text{Ni}_2\text{Mo}_3\text{N}$	1.4	270	40	78.0	25.6	67.9	[16]
3	Pt/SAPO-11	5	300	30	24.2	6.2	41.0	[17]
4	$\text{Ni}_2\text{P}/\text{MCM-41}$	3	290	30	84.0	< 2.0	94.0	[18]
5	$\text{Ni}_3\text{Sn}_2/\text{Al}_2\text{O}_3$	3	340	30	99.9	< 1.0	99.5	[19]

This material is reserved for educational use only, not allowed for commercial use.

Forbidden to modify the content, and cite the document when use.

5.2 Conclusion

Doping K^+ on copper phyllosilicate (CuPS) catalysts can significantly increase hexadecanol selectivity for the hydrogenation of methyl palmitate under atmospheric H_2 pressure, as compared to CuPS. The *in situ* TR-XANEs and Py-IR suggest that the K^+ facilitates the formation of Cu^+ species and a decrease in Brønsted acid sites (BAS) after the reduction. This could presumably be due to the formation of highly polarizable silicate species ($Si-O-(K^+)$) interacting with the Cu^{2+} in the lamellar structure. While doping K^+ on the reduced sample (rCuPS) leads to the reoxidation of metallic Cu to CuO aggregate that could be stabilized by the K^+ at the interface. This resulted in a higher Cu^+/Cu^0 ratio with a significant decrease in BAS after the secondary reduction. The increase in the K^+ loading (0.01 to 0.10wt.%) over rCuPS results in a lower reducibility, higher Cu^+ species (10% to 16%), lower BAS (0.60 to 0.16 $\mu\text{mol/g}$) and larger Cu particle (4 to 5 nm). The hydrogenation activity of K^+ -doped CuPS depends on the balance between the Cu^0 surface and Cu^+ species. An increase in Cu^+ species (up to 14%) could facilitate methyl palmitate adsorption by a preferential interaction between the C=O of an ester and the Lewis acid site (LAS). This could lead to an increase in the activity for 0.05K-rCuPS. However, further increase in Cu^+ species leads to the decreases in Cu^0 surface and hence hydrogenation activity for 0.10K-rCuPS. In a different manner, an increase in Cu^+ species, together with a decrease in BAS, could improve hexadecanol selectivity even at a similar conversion. This is because the re-adsorption and dehydration of hexadecanol, primarily produced, were suppressed over the catalyst with high Cu^+ species and low BAS. Moreover, higher stability can be obtained due to lower production of C_{16} hydrocarbon from hexadecanol dehydration.

Chapter 6

Conclusions and Suggestions

6.1 Conclusions

As the global consumption of biodiesel is relatively steady and tends to decrease in the future, this thesis has accomplished the utilization of biodiesel as a feedstock to produce key intermediate chemicals for industries by using copper phyllosilicate (CuPS) based catalyst at mild condition (250 °C and atmospheric H₂ pressure). The production of linear long-chain α -olefin from hydrodeoxygenation of methyl palmitate over CuPS as a bifunctional catalyst via hydrogenation-dehydration. While, the fatty alcohol was produced via selective hydrogenation of methyl palmitate over K⁺ modified CuPS to tune the Brønsted acid sites (BAS) and Cu⁺ species on CuPS.

High activity on the hydrodeoxygenation of methyl palmitate to 1-hexadecene was observed over CuPS catalyst without the production of C₁₅ hydrocarbon from decarbonylation. This could be attributed to a high active Cu surface area and BAS at the metal-support interface due to the highly dispersed Cu particle. The *in situ* TR-XANES results upon the reduction evidence the presence of Cu⁺ species in CuPS (8-30 wt.%), presumably due to strong interaction between Cu-SiO₂ in octahedrally coordinated Cu²⁺ (O_h) species. In addition, the remaining of Cu⁺ species especially at the metal-support interface provide BAS in a closed proximity to the Cu metal particle. The BAS acts as an active site for dehydration of hexadecanol which primarily produced by the hydrogenation of methyl palmitate. Furthermore, hexadecanol dehydration also depends on the Cu⁺ fraction since Cu⁺ would suppress the adsorption of alcohols. In addition, the CuPS which contain a low Cu⁺ fraction (i.e. 30CuPS) provides a larger Cu particles size and tend to promote the over hydro-dehydration of hexadecanol to hexadecane. Therefore, the 20CuPS has the balance between Cu⁰, Cu⁺ and BAS, leading to the most effective catalyst for the hydrodeoxygenation of methyl palmitate to 1-hexadecene.

The BAS and Cu⁺ species over 20CuPS can be tuned by K⁺ doping. This K⁺ modified 20CuPS can suppress the dehydration of hexadecanol providing a significantly

This material is reserved for educational use only, not allowed for commercial use.

Forbidden to modify the content, and cite the document when use.

increase of hexadecanol selectivity for the hydrogenation of methyl palmitate. The doped K^+ on CuPS could presumably interact with Cu^{2+} in the lamellar structure forming a highly polarizable silicate species ($Si-O-(K^+)$). This species could facilitate to formation of Cu^+ species and decrease the BAS after reduction, as evidence by the *in situ* TR-XANEs and Py-IR, respectively. With a similar of K loading (0.05 wt.%) on reduced sample (rCuPS) leads to the reoxidation of metallic Cu to CuO aggregate that could be stabilized by the K^+ at the interface. This resulted in a higher Cu^+ fraction with a significant decrease in BAS after the secondary reduction. When the amount of K loading was increased from 0.01 wt.% to 0.10 wt.%, a lower reducibility, higher Cu^+ species (10% to 16%), lower BAS (0.60 to 0.16 $\mu\text{mol/g}$) and larger Cu particle (4 to 5 nm) were obtained. The balance between the Cu^0 surface and Cu^+ species were play a role for the hydrogenation activity on K^+ doped CuPS. The highest on the activity ($\sim 60\%$) could be obtained on 0.05K-rCuPS. This could attribute to an increase of Cu^+ fraction (up to 14%) together with high Cu^0 surface which the former could facilitate methyl palmitate adsorption by a preferential interaction between the C=O of an ester while the later motivates the H_2 dissociation and spillover to the adsorbed molecule. However, the further increase in Cu^+ species could be obtained on 0.10K-rCuPS, however, hydrogenation activity was decreased. This could due to decreases in Cu^0 surface on this catalyst. In a different manner, the hexadecanol selectivity could be improved by an increase in Cu^+ species, together with a decrease in BAS. This is because the re-adsorption and dehydration of hexadecanol, primarily produced, were suppressed over the catalyst with high Cu^+ species and low BAS. Furthermore, higher stability can be obtained due to lower production of C_{16} hydrocarbon from hexadecanol dehydration.

6.2 Suggestions

6.2.1 As the production of 1-hexadecene from hydrodeoxygenation of methyl palmitate depends on the dehydration ability of hexadecanol without over hydrogenation or hydro-dehydration to hexadecane. This reaction step could be controlled by the active Cu surface, Cu^+ and BAS which is generated after the reduction under H_2 gas. However, in this work, the CuPS catalysts were reduced only at $250\text{ }^\circ\text{C}$ under pure H_2 gas. This work would be more complete if the effect of reduction temperature and partial H_2 pressure were investigated. These studies would be beneficial for optimizing the Cu surface, Cu^+ and BAS in order to improve the 1-hexadecene selectivity.

6.2.2 The incorporation of acidic support such as Al_2O_3 and Zeolite (HY, HZSM-5) into the CuPS catalyst may increase the dehydration of hexadecanol to hexadecene without the hydro-dehydration to hexadecane.

6.2.3 As the production of hexadecanol from the hydrogenation of methyl palmitate could be promoted on the CuPS catalyst that contains a low BAS with a higher Cu^+ fraction or LAS. The tuning of Cu^+ and BAS on CuPS with the different types of basic alkali doping (i.e. Li, Na, Cs, Ca) might be an alternative. In addition, the incorporation with a high LAS metal oxide such as ZnO or Fe_2O_3 would prevent the re-adsorption of hexadecanol and suppress the dehydration of alcohol.

6.2.4 To commercialize the CuPS-based catalyst for industries, the study on the catalytic design for the conversion of pure feed as well as mixed feed biodiesel (i.e. B100) is necessary. Furthermore, the study on catalytic stability and catalyst regeneration must be validated to compare with the commercial ones.

References

- (1) Issariyakul, T.; Dalai, A. K., Biodiesel from vegetable oils. *Renewable and Sustainable Energy Reviews* **2014**, *31*, 446-471.
- (2) Suresh, M.; Jawahar, C.; Richard, A., A review on biodiesel production, combustion, performance, and emission characteristics of non-edible oils in variable compression ratio diesel engine using biodiesel and its blends. *Renewable and Sustainable Energy Reviews* **2018**, *92*, 38-49.
- (3) Edem, D., Palm oil: Biochemical, physiological, nutritional, hematological and toxicological aspects: A review. *Plant Foods for Human Nutrition* **2002**, *57*, 319-341.
- (4) Nurulain, S.; Aziz, N.; Najib, M.; Salim, M.; Manap, H. In *A review of free fatty acid determination methods for palm cooking oil*, Journal of Physics: Conference Series, IOP Publishing: **2021**; p 012055.
- (5) Domínguez, I. P.; Fellmann, T.; Chatzopoulos, T.; Pieralli, S.; Jensen, H.; Barreiro-Hurle, J.; Micale, F. In *EU commodity market development: Medium-term agricultural outlook*, Proceedings of the October 2017 workshop, **2018**; p 133.
- (6) Tunpaiboon, N. <https://www.krungsri.com/en/research/industry/industry-outlook/Energy-Utilities/Biodiesel/IO/io-biodiesel-21>.
- (7) Belousov, A. S.; Esipovich, A.; Kanakov, E.; Otopkova, K. V., Recent advances in sustainable production and catalytic transformations of fatty acid methyl esters. *Sustainable Energy & Fuels* **2021**.
- (8) Chen, J.; Xu, Q., Hydrodeoxygenation of biodiesel-related fatty acid methyl esters to diesel-range alkanes over zeolite-supported ruthenium catalysts. *Catalysis Science & Technology* **2016**, *6* (19), 7239-7251.
- (9) Han, F.; Guan, Q.; Li, W., Deoxygenation of methyl palmitate over SiO₂-supported nickel phosphide catalysts: effects of pressure and kinetic investigation. *RSC advances* **2015**, *5* (130), 107533-107539.
- (10) Sánchez, M. A.; Mazzieri, V. A.; Vicerich, M. A.; Vera, C. R.; Pieck, C. L., Ru-Sn-B/Al₂O₃ catalysts for selective hydrogenation of methyl oleate: Influence of the Ru/Sn Ratio. *Journal of Chemistry* **2015**, *2015*.
- (11) Lappin, G., *Alpha olefins applications handbook*. CRC press: 2014.

- (12) Mudge, S. M., Fatty alcohols—a review of their natural synthesis and environmental distribution. *The Soap and Detergent Association* **2005**, *132*, 1-141.
- (13) Lu, H.; Yu, T.-Y.; Xu, P.-F.; Wei, H., Selective decarbonylation via transition-metal-catalyzed carbon–carbon bond cleavage. *Chemical Reviews* **2020**, *121* (1), 365-411.
- (14) Santillan-Jimenez, E.; Crocker, M., Catalytic deoxygenation of fatty acids and their derivatives to hydrocarbon fuels via decarboxylation/decarbonylation. *Journal of Chemical Technology & Biotechnology* **2012**, *87* (8), 1041-1050.
- (15) Li, J.; Zhang, J.; Wang, S.; Xu, G.; Wang, H.; Vlachos, D. G., Chemoselective hydrodeoxygenation of carboxylic acids to hydrocarbons over nitrogen-doped carbon–alumina hybrid supported iron catalysts. *ACS catalysis* **2019**, *9* (2), 1564-1577.
- (16) Yan, L.; Liu, X.; Deng, J.; Fu, Y., Molybdenum modified nickel phyllosilicates as a high performance bifunctional catalyst for deoxygenation of methyl palmitate to alkanes under mild conditions. *Green Chemistry* **2017**, *19* (19), 4600-4609.
- (17) Snåre, M.; Kubic̃kova, I.; Mäki-Arvela, P.; Eränen, K.; Murzin, D. Y., Heterogeneous catalytic deoxygenation of stearic acid for production of biodiesel. *Industrial & engineering chemistry research* **2006**, *45* (16), 5708-5715.
- (18) Krishnapriya, R.; Gupta, U.; Soni, V. K.; Sharma, R. K., Catalytic conversion of methyl oleate to hydrocarbons: impact of cobalt oxide species integration in SiO₂–Al₂O₃. *Sustainable Energy & Fuels* **2020**, *4* (7), 3308-3317.
- (19) Phichitsurathaworn, P.; Choojun, K.; Poo-arporn, Y.; Sooknoi, T., Deoxygenation of heptanoic acid to hexene over cobalt-based catalysts: A model study for α -olefin production from renewable fatty acid. *Applied Catalysis A: General* **2020**, *602*, 117644.
- (20) Gawande, M. B.; Goswami, A.; Felpin, F.-X.; Asefa, T.; Huang, X.; Silva, R.; Zou, X.; Zboril, R.; Varma, R. S., Cu and Cu-based nanoparticles: synthesis and applications in catalysis. *Chemical reviews* **2016**, *116* (6), 3722-3811.
- (21) Pestman, R.; Koster, R.; Pieterse, J.; Ponec, V., Reactions of carboxylic acids on oxides: 1. Selective hydrogenation of acetic acid to acetaldehyde. *Journal of catalysis* **1997**, *168* (2), 255-264.

- (22) Jiang, J. W.; Tu, C. C.; Chen, C. H.; Lin, Y. C., Highly Selective Silica-supported Copper Catalysts Derived from Copper Phyllosilicates in the Hydrogenation of Adipic Acid to 1, 6-hexanediol. *ChemCatChem* **2018**, *10* (23), 5449-5458.
- (23) Xu, C.; Chen, G.; Zhao, Y.; Liu, P.; Duan, X.; Gu, L.; Fu, G.; Yuan, Y.; Zheng, N., Interfacing with silica boosts the catalysis of copper. *Nature communications* **2018**, *9* (1), 1-10.
- (24) Kumar, R.; Strezov, V.; Kan, T.; Weldekidan, H.; He, J., Investigating the effect of Cu/zeolite on deoxygenation of bio-oil from pyrolysis of pine wood. *Energy Procedia* **2019**, *160*, 186-193.
- (25) Xu, Y.; Kong, L.; Huang, H.; Wang, H.; Wang, X.; Wang, S.; Zhao, Y.; Ma, X., Promotional effect of indium on Cu/SiO₂ catalysts for the hydrogenation of dimethyl oxalate to ethylene glycol. *Catalysis Science & Technology* **2021**, *11* (20), 6854-6865.
- (26) Zhang, Z.; Zhou, F.; Chen, K.; Fu, J.; Lu, X.; Ouyang, P., Catalytic *in situ* hydrogenation of fatty acids into fatty alcohols over Cu-based catalysts with methanol in hydrothermal media. *Energy & Fuels* **2017**, *31* (11), 12624-12632.
- (27) Gong, J.; Yue, H.; Zhao, Y.; Zhao, S.; Zhao, L.; Lv, J.; Wang, S.; Ma, X., Synthesis of ethanol via syngas on Cu/SiO₂ catalysts with balanced Cu⁰-Cu⁺ sites. *Journal of the American Chemical Society* **2012**, *134* (34), 13922-13925.
- (28) Bian, Z.; Kawi, S., Preparation, characterization and catalytic application of phyllosilicate: A review. *Catalysis Today* **2020**, *339*, 3-23.
- (29) Chen, L.-F.; Guo, P.-J.; Qiao, M.-H.; Yan, S.-R.; Li, H.-X.; Shen, W.; Xu, H.-L.; Fan, K.-N., Cu/SiO₂ catalysts prepared by the ammonia-evaporation method: Texture, structure, and catalytic performance in hydrogenation of dimethyl oxalate to ethylene glycol. *Journal of Catalysis* **2008**, *257* (1), 172-180.
- (30) Zhu, S.; Gao, X.; Zhu, Y.; Fan, W.; Wang, J.; Li, Y., A highly efficient and robust Cu/SiO₂ catalyst prepared by the ammonia evaporation hydrothermal method for glycerol hydrogenolysis to 1, 2-propanediol. *Catalysis Science & Technology* **2015**, *5* (2), 1169-1180.
- (31) Tsou, Y.-J.; To, T. D.; Chiang, Y.-C.; Lee, J.-F.; Kumar, R.; Chung, P.-W.; Lin, Y.-C., Hydrophobic copper catalysts derived from copper phyllosilicates in the hydrogenation of levulinic acid to γ -valerolactone. *ACS Applied Materials & Interfaces* **2020**, *12* (49), 54851-54861.

- (32) Che, C.; Glotch, T. D.; Bish, D. L.; Michalski, J. R.; Xu, W., Spectroscopic study of the dehydration and/or dehydroxylation of phyllosilicate and zeolite minerals. *Journal of Geophysical Research: Planets* **2011**, *116* (E5).
- (33) Li, H.; Chen, T.; Wang, G., The effect of alkali metals doping on properties of CuMgCe for isobutanol synthesis from syngas. *Applied Catalysis A: General* **2022**, *639*, 118607.
- (34) Hu, D.; Hu, H.; Zhou, H.; Li, G.; Chen, C.; Zhang, J.; Yang, Y.; Hu, Y.; Zhang, Y.; Wang, L., The effect of potassium on Cu/Al₂O₃ catalysts for the hydrogenation of 5-hydroxymethylfurfural to 2, 5-bis (hydroxymethyl) furan in a fixed-bed reactor. *Catalysis Science & Technology* **2018**, *8* (23), 6091-6099.
- (35) Besson, M. L.; Gallezot, P.; Pinel, C., Conversion of biomass into chemicals over metal catalysts. *Chemical reviews* **2014**, *114* (3), 1827-1870.
- (36) Tursi, A., A review on biomass: importance, chemistry, classification, and conversion. *Biofuel Research Journal* **2019**, *6* (2), 962.
- (37) Alonso, D. M.; Bond, J. Q.; Dumesic, J. A., Catalytic conversion of biomass to biofuels. *Green chemistry* **2010**, *12* (9), 1493-1513.
- (38) Edem, D., Palm oil: Biochemical, physiological, nutritional, hematological and toxicological aspects: A review. *Plant Foods for Human Nutrition* **2002**, *57* (3), 319-341.
- (39) Alleman, T. L.; McCormick, R. L.; Christensen, E. D.; Fioroni, G.; Moriarty, K.; Yanowitz, J. *Biodiesel handling and use guide*; National Renewable Energy Lab.(NREL), Golden, CO (United States): 2016.
- (40) Zhang, P.; Chen, X.; Leng, Y.; Dong, Y.; Jiang, P.; Fan, M., Biodiesel production from palm oil and methanol via zeolite derived catalyst as a phase boundary catalyst: An optimization study by using response surface methodology. *Fuel* **2020**, *272*, 117680.
- (41) Sarantopoulos, I.; Chatzisyneon, E.; Foteinis, S.; Tsoutsos, T., Energy for Sustainable Development Optimization of biodiesel production from waste lard by a two-step transesterification process under mild conditions. *Energy. Sustain. Dev.* **2014**, *23*, 110-114.
- (42) Belousov, A. S.; Esipovich, A. L.; Kanakov, E. A.; Otopkova, K. V., Recent advances in sustainable production and catalytic transformations of fatty acid methyl esters. *Sustainable Energy & Fuels* **2021**, *5* (18), 4512-4545.

- (43) Pratas, M. J.; Freitas, S.; Oliveira, M. B.; Monteiro, S. C.; Lima, A. S.; Coutinho, J. A., Densities and viscosities of fatty acid methyl and ethyl esters. *Journal of Chemical & Engineering Data* **2010**, *55* (9), 3983-3990.
- (44) Tembe, G. L.; Ravindranathan, M., Oligomerization of ethylene to linear. alpha-olefins by a titanium aryl oxide-alkylaluminum catalyst. *Industrial & engineering chemistry research* **1991**, *30* (10), 2247-2252.
- (45) Golub, F.; Bolotov, V.; Parmon, V., Modern Trends in the Processing of Linear Alpha Olefins into Technologically Important Products: Part I. *Catalysis in Industry* **2021**, *13* (2), 168-186.
- (46) Han, J.; Sun, H.; Ding, Y.; Lou, H.; Zheng, X., Palladium-catalyzed decarboxylation of higher aliphatic esters: Towards a new protocol to the second generation biodiesel production. *Green Chemistry* **2010**, *12* (3), 463-467.
- (47) Janampelli, S.; Darbha, S., Selective and reusable Pt-WO_x/Al₂O₃ catalyst for deoxygenation of fatty acids and their esters to diesel-range hydrocarbons. *Catalysis Today* **2018**, *309*, 219-226.
- (48) Shah, J.; Arslan, E.; Cirucci, J.; O'Brien, J.; Moss, D., Comparison of oleo-vs petro-sourcing of fatty alcohols via cradle-to-gate life cycle assessment. *Journal of surfactants and detergents* **2016**, *19* (6), 1333-1351.
- (49) Yuki, Y.; Takahashi, K.; Tanaka, Y.; Nozaki, K., Tandem isomerization/hydroformylation/hydrogenation of internal alkenes to n-alcohols using Rh/Ru dual-or ternary-catalyst systems. *Journal of the American Chemical Society* **2013**, *135* (46), 17393-17400.
- (50) Sánchez, M. A.; Torres, G. C.; Mazzieri, V. A.; Pieck, C. L., Selective hydrogenation of fatty acids and methyl esters of fatty acids to obtain fatty alcohols—a review. *Journal of Chemical Technology & Biotechnology* **2017**, *92* (1), 27-42.
- (51) Fatty alcohol. Available : <https://www.musimmas.com/product/fatty-alcohols/>.
- (52) Hark, S. v. d.; Härröd, M.; Møller, P., Hydrogenation of fatty acid methyl esters to fatty alcohols at supercritical conditions. *Journal of the American Oil Chemists' Society* **1999**, *76* (11), 1363-1370.
- (53) Adkins, H.; Folkers, K., The catalytic hydrogenation of esters to alcohols. *Journal of the American Chemical Society* **1931**, *53* (3), 1095-1097.

- (54) Pouilloux, Y.; Autin, F.; Guimon, C.; Barrault, J., Hydrogenation of fatty esters over ruthenium–tin catalysts; characterization and identification of active centers. *Journal of Catalysis* **1998**, *176* (1), 215-224.
- (55) Bergman, S. L.; Dahlin, S.; Mesilov, V. V.; Xiao, Y.; Englund, J.; Xi, S.; Tang, C.; Skoglundh, M.; Pettersson, L. J.; Bernasek, S. L., In-situ studies of oxidation/reduction of copper in Cu-CHA SCR catalysts: comparison of fresh and SO₂-poisoned catalysts. *Applied Catalysis B: Environmental* **2020**, *269*, 118722.
- (56) To, D.-T.; Lin, Y.-C., Copper Phyllosilicates-Derived Catalysts in the Production of Alcohols from Hydrogenation of Carboxylates, Carboxylic Acids, Carbonates, Formyls, and CO₂: A Review. *Catalysts* **2021**, *11* (2), 255.
- (57) Sun, Y.; Meng, F.; Ge, Q.; Sun, J., Importance of the initial oxidation state of copper for the catalytic hydrogenation of dimethyl oxalate to ethylene glycol. *ChemistryOpen* **2018**, *7* (12), 969-976.
- (58) Huang, H.; Wang, B.; Wang, Y.; Zhao, Y.; Wang, S.; Ma, X., Partial hydrogenation of dimethyl oxalate on Cu/SiO₂ catalyst modified by sodium silicate. *Catalysis Today* **2020**, *358*, 68-73.
- (59) Ai, P.; Tan, M.; Reubroycharoen, P.; Wang, Y.; Feng, X.; Liu, G.; Yang, G.; Tsubaki, N., Probing the promotional roles of cerium in the structure and performance of Cu/SiO₂ catalysts for ethanol production. *Catalysis Science & Technology* **2018**, *8* (24), 6441-6451.
- (60) Wells, A., The lanthanides and actinides. In *Structural inorganic chemistry*. 5. ed, **1984**.
- (61) Poo-arporn, Y.; Chirawatkul, P.; Saengsui, W.; Chotiwan, S.; Kityakarn, S.; Klinkhieo, S.; Hormes, J.; Songsiriritthigul, P., Time-resolved XAS (Bonn-SUT-SLRI) beamline at SLRI. *Journal of Synchrotron Radiation* **2012**, *19* (6), 937-943.
- (62) Di, W.; Cheng, J.; Tian, S.; Li, J.; Chen, J.; Sun, Q., Synthesis and characterization of supported copper phyllosilicate catalysts for acetic ester hydrogenation to ethanol. *Applied Catalysis A: General* **2016**, *510*, 244-259.
- (63) Heller-Kallai, L.; Rozenson, L., Dehydroxylation of dioctahedral phyllosilicates. *Clays and Clay Minerals* **1980**, *28*, 355-368.

- (64) Gaur, A.; Klysubun, W.; Nair, N. N.; Shrivastava, B.; Prasad, J.; Srivastava, K., XAFS study of copper(II) complexes with square planar and square pyramidal coordination geometries. *Journal of Molecular Structure* **2016**, *1118*, 212-218.
- (65) Ma, K.; Tian, Y.; Zhao, Z.-J.; Cheng, Q.; Ding, T.; Zhang, J.; Zheng, L.; Jiang, Z.; Abe, T.; Tsubaki, N., Achieving efficient and robust catalytic reforming on dual-sites of Cu species. *Chemical Science* **2019**, *10* (9), 2578-2584.
- (66) Sun, Z.; Zhang, J.; Yin, L.; Hu, G.; Fang, R.; Cheng, H.-M.; Li, F., Conductive porous vanadium nitride/graphene composite as chemical anchor of polysulfides for lithium-sulfur batteries. *Nature communications* **2017**, *8* (1), 14627.
- (67) Lezcano-Gonzalez, I.; Deka, U.; Arstad, B., A. vanYperen-De Deyne, K. Hemelsoet, M. Waroquier, V. van Speybroeck, BM Weckhuysen, AM Beale. *Phys. Chem. Chem. Phys* **2014**, *16*, 1639-1650.
- (68) Jankowska, A.; Chtopek, A.; Kowalczyk, A.; Rutkowska, M.; Michalik, M.; Liu, S.; Chmielarz, L., Catalytic performance of spherical MCM-41 modified with copper and iron as catalysts of NH₃-SCR process. *Molecules* **2020**, *25* (23), 5651.
- (69) Lomate, S.; Sultana, A.; Fujitani, T., Effect of SiO₂ support properties on the performance of Cu-SiO₂ catalysts for the hydrogenation of levulinic acid to gamma valerolactone using formic acid as a hydrogen source. *Catalysis Science & Technology* **2017**, *7* (14), 3073-3083.
- (70) Parry, E., An infrared study of pyridine adsorbed on acidic solids. Characterization of surface acidity. *Journal of Catalysis* **1963**, *2* (5), 371-379.
- (71) Zaki, M. I.; Hasan, M. A.; Al-Sagheer, F. A.; Pasupulety, L., *In situ* FTIR spectra of pyridine adsorbed on SiO₂-Al₂O₃, TiO₂, ZrO₂ and CeO₂: general considerations for the identification of acid sites on surfaces of finely divided metal oxides. *Colloids and Surfaces A: Physicochemical and Engineering Aspects* **2001**, *190* (3), 261-274.
- (72) Emeis, C., Determination of integrated molar extinction coefficients for infrared absorption bands of pyridine adsorbed on solid acid catalysts. *Journal of catalysis* **1993**, *141* (2), 347-354.
- (73) Xu, C.; Chen, G.; Zhao, Y.; Liu, P.; Duan, X.; Gu, L.; Fu, G.; Yuan, Y.; Zheng, N., Interfacing with silica boosts the catalysis of copper. *Nature communications* **2018**, *9* (1), 3367.

- (74) Deliy, I. V.; Shamanaev, I. V.; Aleksandrov, P. V.; Gerasimov, E. Y.; Pakharukova, V. P.; Kodenev, E. G.; Yakovlev, I. V.; Lapina, O. B.; Bukhtiyarova, G. A., Support effect on the performance of Ni₂P catalysts in the hydrodeoxygenation of methyl palmitate. *Catalysts* **2018**, *8* (11), 515.
- (75) Kaewmeesri, R.; Nonkumwong, J.; Kiatkittipong, W.; Laosiripojana, N.; Faungnawakij, K., Deoxygenations of palm oil-derived methyl esters over mono- and bimetallic NiCo catalysts. *Journal of Environmental Chemical Engineering* **2021**, *9* (2), 105128.
- (76) Numwong, N.; Prabnasak, P.; Prayoonpunratn, P.; Triphatthanaphong, P.; Thunyaratchatanon, C.; Mochizuki, T.; Chen, S.-Y.; Luengnaruemitchai, A.; Sooknoi, T., Effect of Pd particle size on activity and cis-trans selectivity in partial hydrogenation of soybean oil-derived FAMES over Pd/SiO₂ catalysts. *Fuel Processing Technology* **2020**, *203*, 106393.
- (77) Qin, H.; Guo, C.; Sun, C.; Zhang, J., Influence of the support composition on the hydrogenation of methyl acetate over Cu/MgO-SiO₂ catalysts. *Journal of Molecular Catalysis A: Chemical* **2015**, *409*, 79-84.
- (78) Ye, C.-L.; Guo, C.-L.; Zhang, J.-L., Highly active and stable CeO₂-SiO₂ supported Cu catalysts for the hydrogenation of methyl acetate to ethanol. *Fuel Processing Technology* **2016**, *143*, 219-224.
- (79) Prasanseang, W.; Choojun, K.; Poo-arporn, Y.; Huang, A.-L.; Lin, Y.-C.; Sooknoi, T., Linear long-chain α -olefins from hydrodeoxygenation of methyl palmitate over copper phyllosilicate catalysts. *Applied Catalysis A: General* **2022**, *635*, 118555.
- (80) Dong, X.; Ma, X.; Xu, H.; Ge, Q., Comparative study of silica-supported copper catalysts prepared by different methods: Formation and transition of copper phyllosilicate. *Catalysis Science & Technology* **2016**, *6* (12), 4151-4158.
- (81) Timoshenko, J.; Roldan Cuenya, B., *In situ/operando* electrocatalyst characterization by X-ray absorption spectroscopy. *Chemical reviews* **2020**, *121* (2), 882-961.
- (82) Wang, B.-J.; Zhang, J.-P.; Han, Y.; Gao, Y.-K.; Xiang, G.-L.; Chu, G.-W.; Luo, Y., K⁺-Modified Redox Properties of the CuO_x/CeO₂ Catalyst for Highly Efficient CO Oxidation. *ACS Engineering Au* **2022**, *2* (6), 486-495.

- (83) Fang, Y.; Sun, H.; Ma, B.; Zhao, C., K⁺-induced formation of granular and dense copper phyllosilicate precursor converts dimethyl oxalate to ethylene glycol in absence of H₂. *Journal of Catalysis* **2022**, *407*, 44-53.
- (84) Chung, K.; Bang, J.; Thacharon, A.; Song, H. Y.; Kang, S. H.; Jang, W.-S.; Dhull, N.; Thapa, D.; Ajmal, C. M.; Song, B., Non-oxidized bare copper nanoparticles with surface excess electrons in air. *Nature Nanotechnology* **2022**, *17* (3), 285-291.
- (85) Wang, Y.; Shen, Y.; Zhao, Y.; Lv, J.; Wang, S.; Ma, X., Insight into the balancing effect of active Cu species for hydrogenation of carbon–oxygen bonds. *ACS Catalysis* **2015**, *5* (10), 6200-6208.
- (86) Li, A.; Yao, D.; Yang, Y.; Yang, W.; Li, Z.; Lv, J.; Huang, S.; Wang, Y.; Ma, X., Active Cu⁰–Cu^{σ+} sites for the hydrogenation of carbon–oxygen bonds over Cu/CeO₂ catalysts. *ACS Catalysis* **2022**, *12* (2), 1315-1325.
- (87) Wang, R.; Zhao, Z.; Gao, P.; Chen, K.; Gan, Z.; Fu, Q.; Hou, G., Impact of Adsorption Configurations on Alcohol Dehydration over Alumina Catalysts. *The Journal of Physical Chemistry C* **2022**, *126* (24), 10073-10080.
- (88) Zhao, C.; Wang, J.; Chen, X.; Liang, C., Nickel Molybdenum Bimetallic Nitrides as Efficient Catalysts for the Hydrodeoxygenation of Methyl Palmitate. *European Journal of Inorganic Chemistry* **2023**, *26* (17), e202300073.
- (89) Chen, N.; Ren, Y.; Qian, E. W., Elucidation of the active phase in PtSn/SAPO-11 for hydrodeoxygenation of methyl palmitate. *Journal of Catalysis* **2016**, *334*, 79-88.
- (90) Guan, Q.; Wan, F.; Han, F.; Liu, Z.; Li, W., Hydrodeoxygenation of methyl palmitate over MCM-41 supported nickel phosphide catalysts. *Catalysis Today* **2016**, *259*, 467-473.
- (91) Shu, S.; Wang, Z.; Zhang, X.; Shi, H.; Feng, S.; Chen, J., Efficient deoxygenation of methyl esters to hydrocarbons on Al₂O₃ supported Ni-Sn intermetallic compounds. *Molecular Catalysis* **2023**, *540*, 113056.



This material is reserved for educational use only, not allowed for commercial use.

Forbidden to modify the content, and cite the document when use.

Appendix A

Supporting information in chapter 4

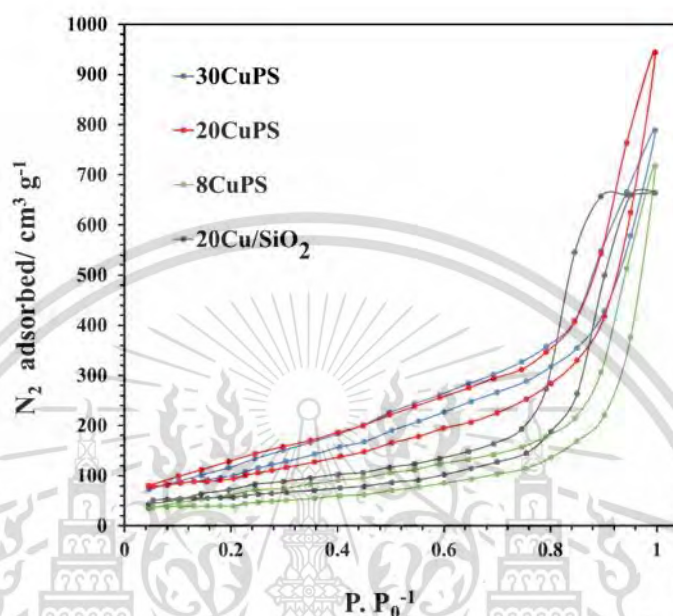


Figure A1 N_2 adsorption-desorption isotherm of calcined CuPS catalysts.

Table A1 XANEs absorption edge energy of Cu standards, CuPS and Cu/SiO₂ after calcined at 400°C and reduction at 250°C.

Samples	Cu edge energy (eV)	
	Calcination	Reduction (250 °C)
Cu standards		
Cu foil	8979.1	-
Cu ₂ O	8980.5	-
CuO	8990.2	-
CuSO ₄	8992.3	-
Samples		
8CuPS	8991.2	8979.1
20CuPS	8991.1	8979.1
30CuPS	8991.0	8979.1
20Cu/SiO ₂	8990.2	8979.1

This material is reserved for educational use only, not allowed for commercial use.

Forbidden to modify the content, and cite the document when use.

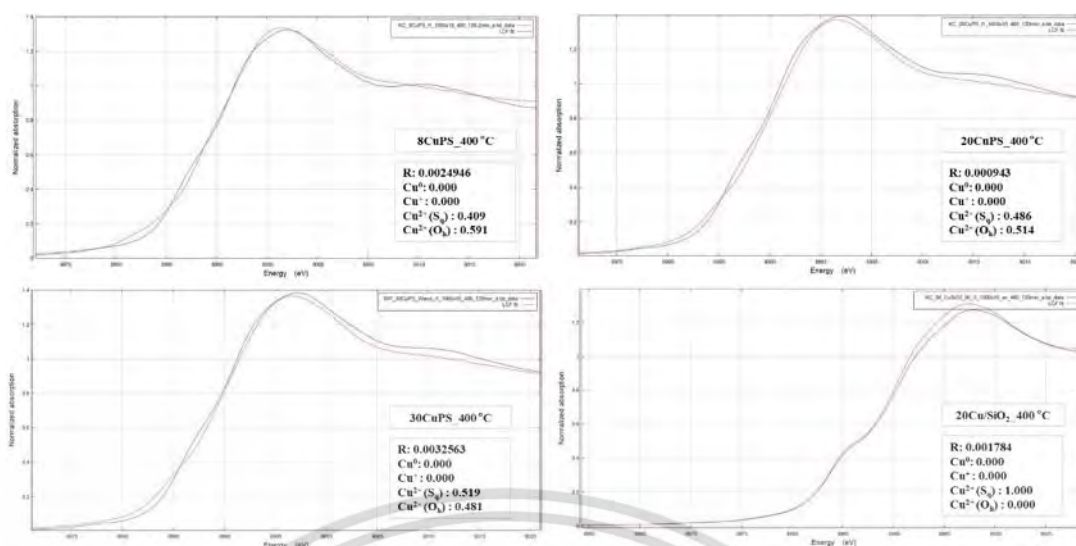


Figure A2 The examples of linear combination fitting (LCF) of CuPS and Cu/SiO₂ catalysts with R-factor at 400 °C under 10%O₂/N₂ evaluated by Athena software.

Table A2 The difference of Cu loading calculated by XRF and H₂ TPR, Cu⁰ and Cu⁺ content calculated by *in situ* TR-XANES of all catalysts.

Catalyst	Cu loading (XRF)	Cu loading (H ₂ -TPR)	Difference percentage (%)	Cu ⁰ content (mmol/g) ^a	Cu ⁺ content (mmol/g) ^b	Cu _s ⁰ (mmol/g) ^c
8CuPS	7.6	5.6	-26.3	1.03	0.20	0.80
20CuPS	20.8	19.2	-7.7	2.94	0.33	2.15
30CuPS	28.0	27.0	-3.6	4.07	0.34	2.47
20Cu/SiO ₂	18.5	18.4	-0.5	2.91	0.00	0.29

The Cu⁰ and Cu⁺ species determined by *in situ* Cu k-edge TR-XANES using linear combination fitting. ^(a)The Cu⁰ content calculated by %Cu⁰ x Cu content. ^(b)The Cu⁺ content calculated by %Cu⁺ x Cu content. ^(c)Cu⁰ on surface (Cu_s⁰) was estimated by H₂-TPR.

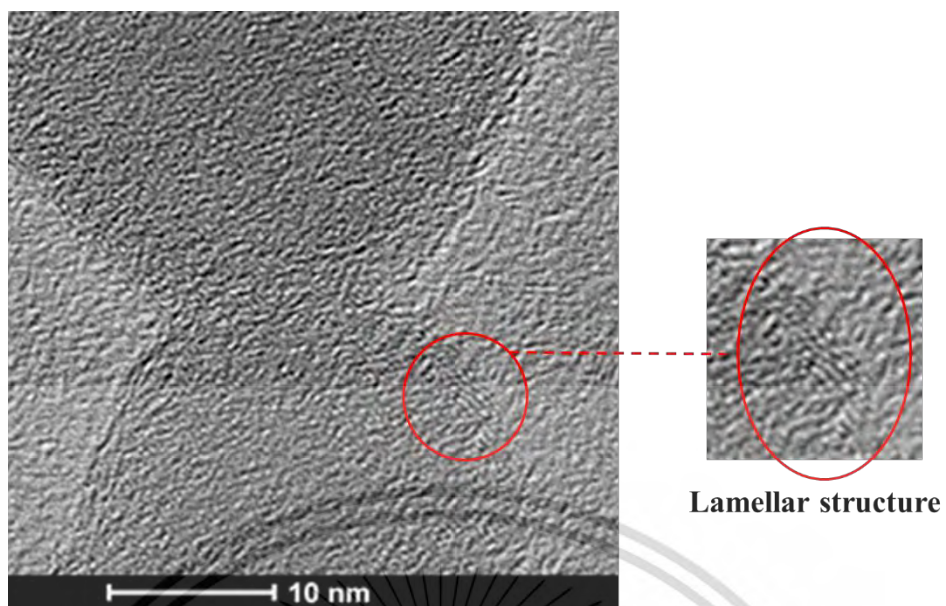


Figure A3 The TEM image of lamellar structure on CuPS-red samples.

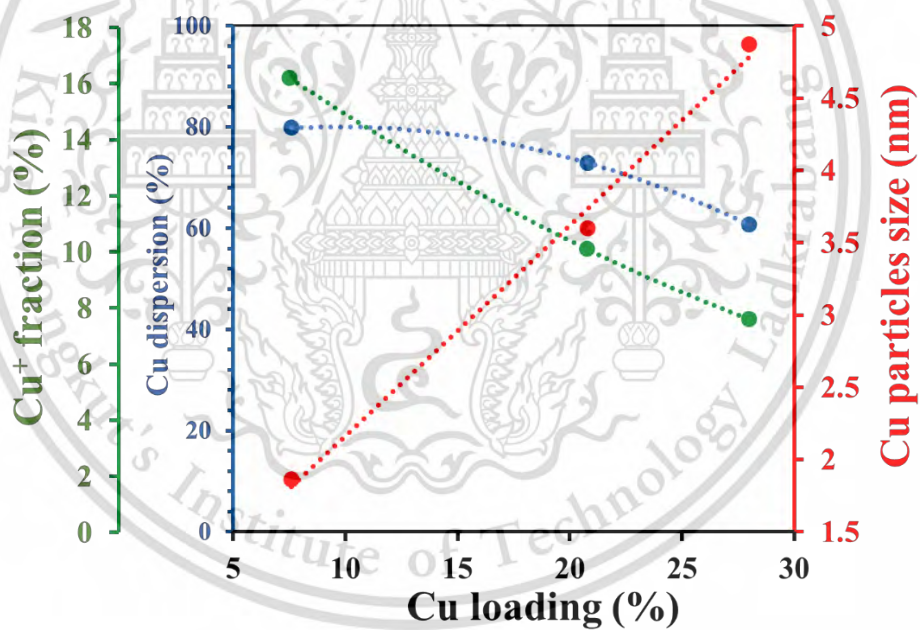


Figure A4 The relation of Cu loading vs Cu dispersion Cu⁺ fraction and Cu particles size.

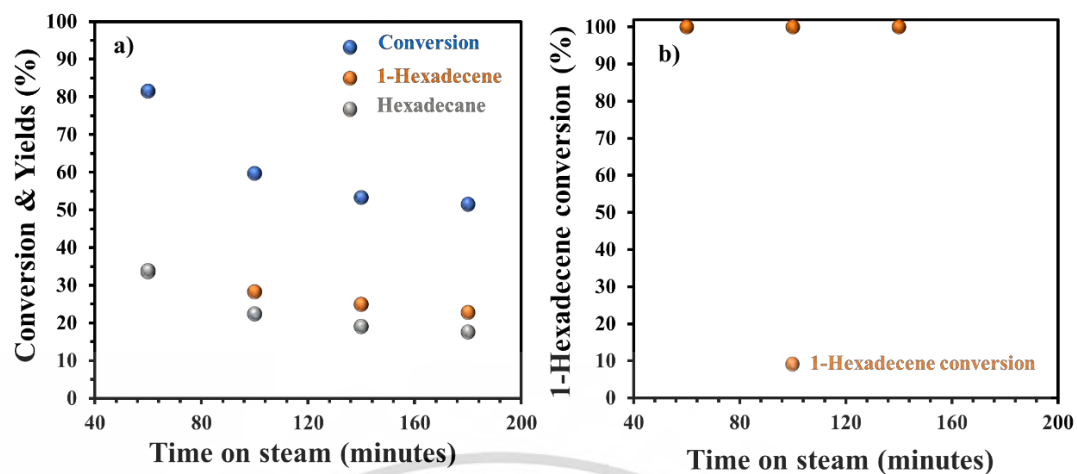


Figure A5 Catalytic conversion of hexadecanol over 30CuPS and 1-Hexadecene over 20CuPS catalyst at 374 g.h/mol of contact time. (Condition: reaction temperature 250 °C, 3 wt.% of hexadecanol and 10 wt.% of 1-hexadecene in dodecane, feed rate 7.2 and 2.4 mL/h, contact time 374 g^{*}h/mol based on catalyst, activation temperature 400 °C, reduction temperature 250 °C, 1 atm, and 180 mL/min of H₂. The activity is at 1 h on stream).

Appendix B

Supporting information in chapter 5

Table B1 The surface area, pore size and pore volume of CuPS, Cu/SiO₂ and 0.05K-CuPS before reduction.

Entry	Catalysts	N ₂ adsorption		
		S _{BET} (m ² /g)	D _{pore} (Å)	V _{pore} (cm ³ /g)
1	CuPS (as prepared)	344	158	1.35
2	Cu/SiO ₂	198	207	1.03
3	0.05K-CuPS (as prepared)	346	124	1.07

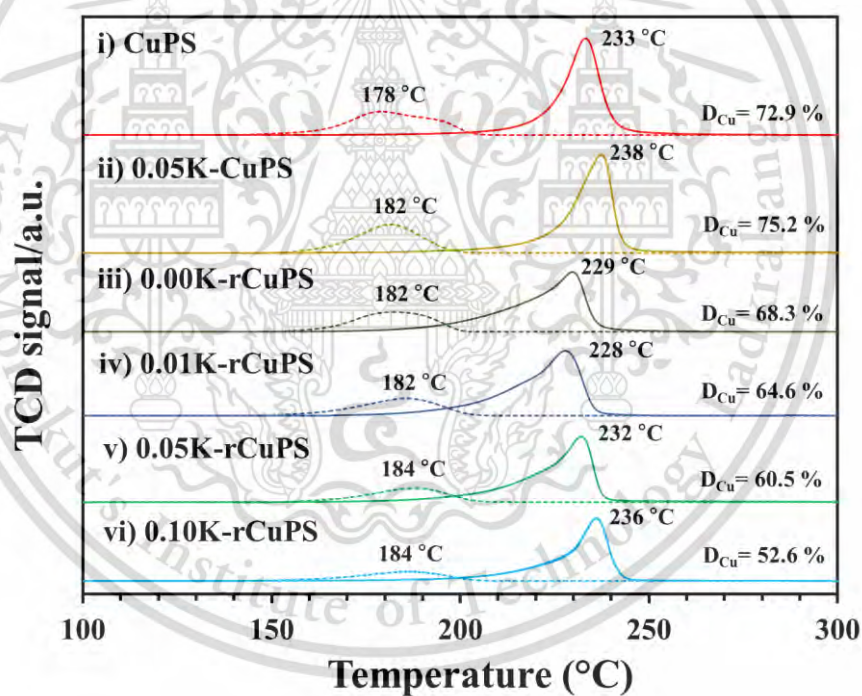


Figure B1 The dissociative N₂O adsorption using H₂-TPR of all catalysts.

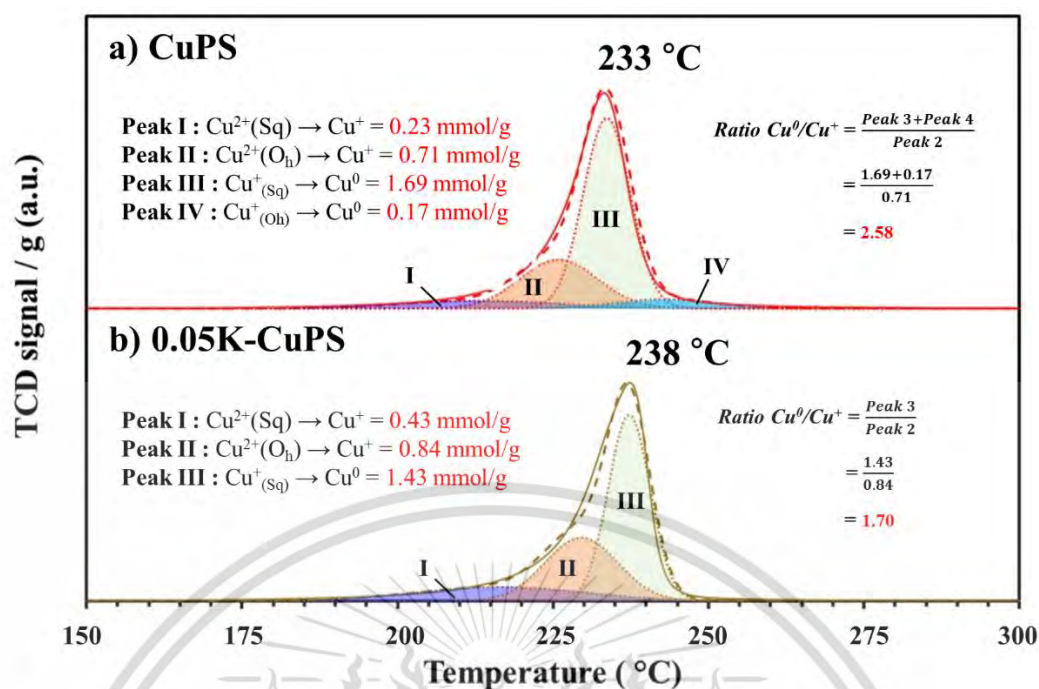


Figure B2 The deconvolution of H_2 -TPR profiles in a) CuPS and b) 0.05K-CuPS.

Table B2 The Cu^0 and Cu^+ content calculated by *in situ* XANES and mole of Cu on surface of all catalysts.

Catalyst	Cu^0 content (mmol/g)	Cu^+ content (mmol/g)	Cu_s^0 (mmol/g)
CuPS	2.72	0.31	1.98
0.01K-rCuPS	2.68	0.30	1.73
0.05K-rCuPS	2.54	0.42	1.54
0.10K-rCuPS	2.46	0.48	1.30
0.05K-CuPS	2.62	0.34	1.97

The Cu^0 and Cu^+ species determined by *in situ* Cu K-edge XANES using liner combination fitting. The Cu^0 content calculated by $\% \text{Cu}^0 \times \text{Cu}$ content. The Cu^+ content calculated by $\% \text{Cu}^+ \times \text{Cu}$ content.

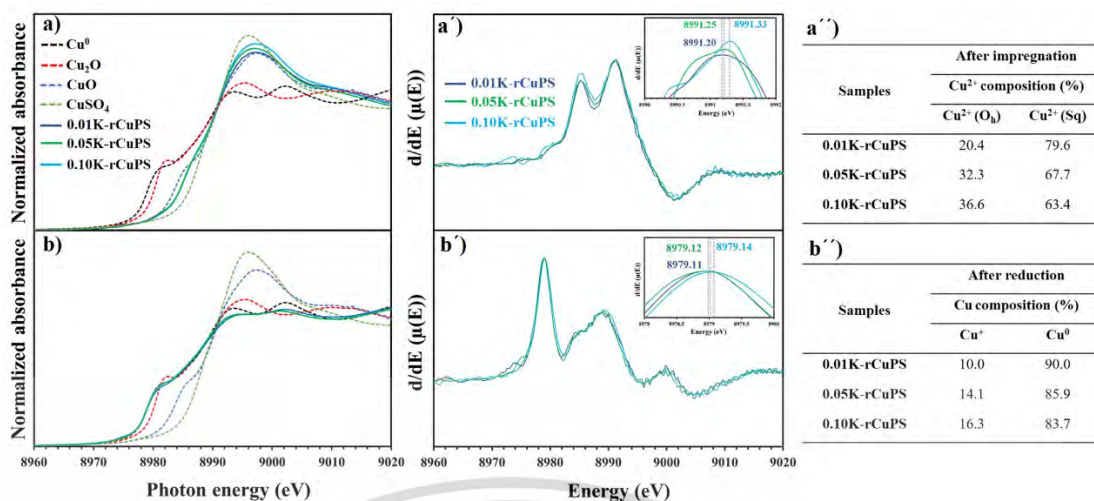


Figure B3 XANES spectra of 0.01K, 0.05K and 0.10K-rCuPS after a) impregnation b) reduction, The first derivative after a') impregnation and b') reduction, LCF of XANES spectra a'') after impregnation b'') after reduction.

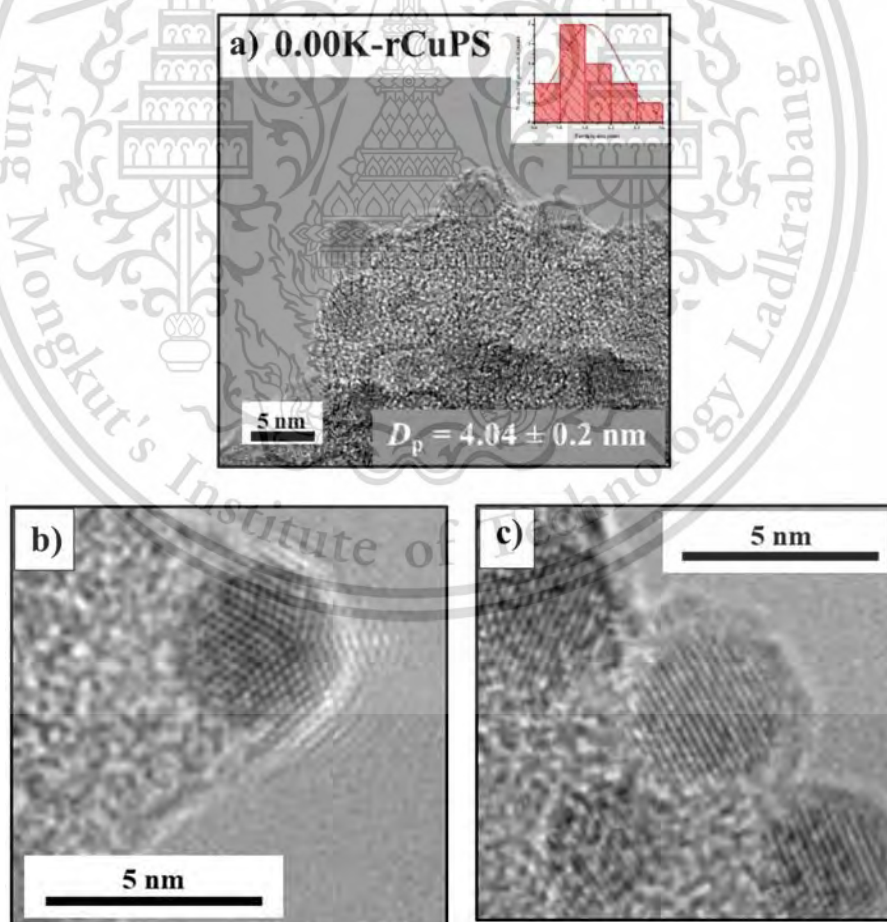


Figure B4 TEM image of Cu particles on a) 0.00K-rCuPS b) CuPS and c) 0.05K-CuPS.

Table B3 Acidity and type of acid sites of all K⁺ doped on rCuPS catalysts.

Entry	Catalyst	Acidity ($\mu\text{mol/g}$) ^a				Type of acid site ($\mu\text{mol/g}$) ^b		LAS/Cu ⁺ ($\times 10^{-2}$)	BAS/Cu ₅ ⁰ ($\times 10^{-4}$)
		Weak acid sites - External silanol (120 °C)	Medium acid sites- Cu surface (175 °C)	Strong acid sites - Internal silanol (250 °C)	Total acidity	Lewis acid (LAS)	Brønsted acid (BAS)		
1	0.01K-rCuPS	5.1	8.6	6.2	19.9	3.89	0.60	1.31	3.5
2	0.05K-rCuPS	1.7	5.2	5.4	12.3	4.89	0.33	1.17	2.1
3	0.10K-rCuPS	0.6	3.2	3.7	7.5	5.80	0.16	1.21	1.2

^aThe acidity was evaluated by NH₃-TPD. ^bThe Brønsted and Lewis acid was calculated via *in situ* infrared spectroscopy of pyridine adsorption (Py-IR).

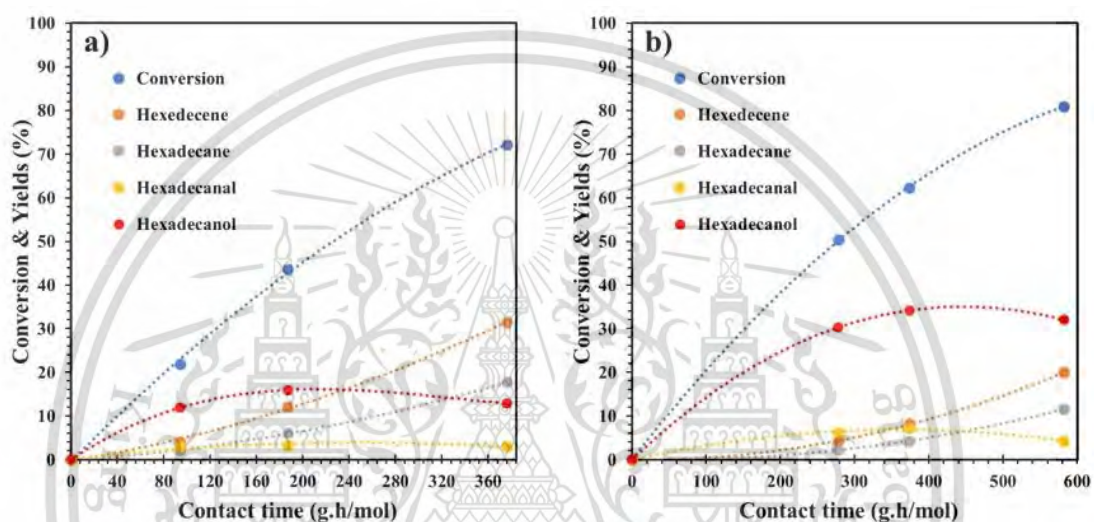


Figure B5 Effect of contact time vs conversion & product yield over a) 20CuPS and b) 0.05K-rCuPS at 60 minutes of time on stream.

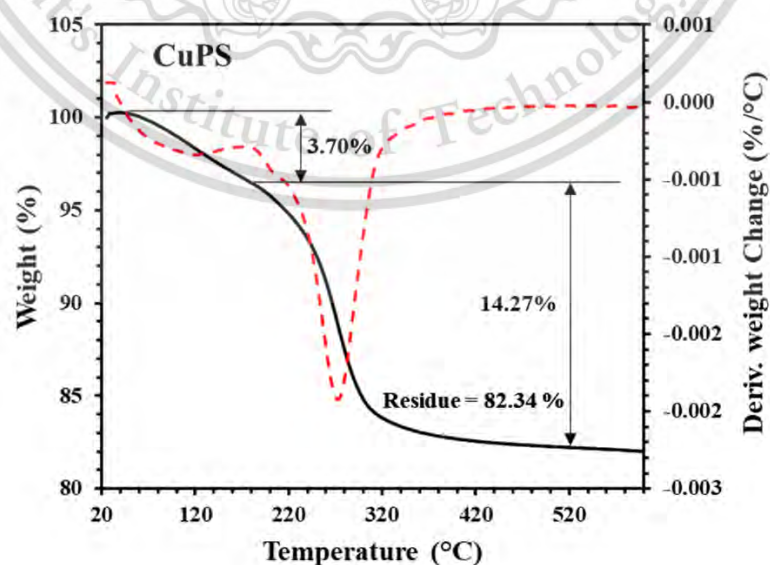


Figure B6 TGA and DTG of spent CuPS catalyst.

This material is reserved for educational use only, not allowed for commercial use.

Forbidden to modify the content, and cite the document when use.

Appendix C

Temperature program condition for all experiments

C1. Calcination of copper phyllosilicate in air zero (synthesis process).

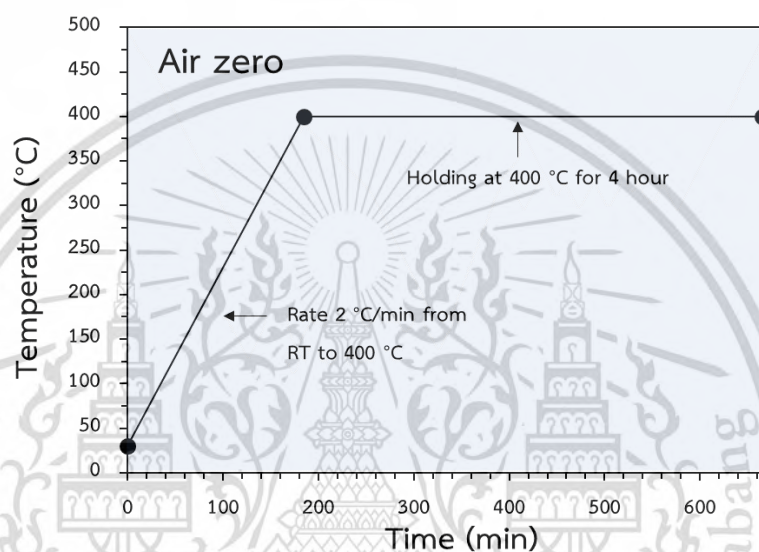


Figure C1 Temperature profile of catalysts calcination in air zero.

C2. Temperature program reduction (H_2 -TPR).

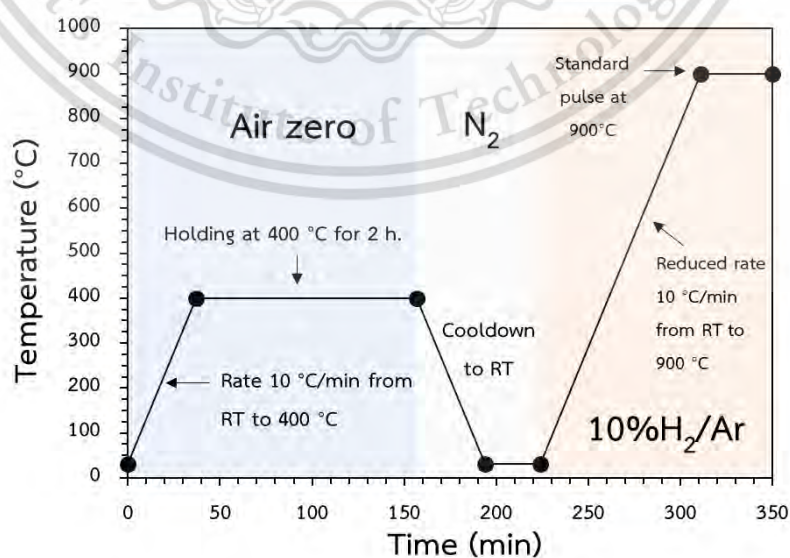


Figure C2 Temperature profile of *in situ* activation and H_2 -TPR for all catalysts.

This material is reserved for educational use only, not allowed for commercial use.

Forbidden to modify the content, and cite the document when use.

C3. Dissociative N₂O adsorption using H₂-TPR.

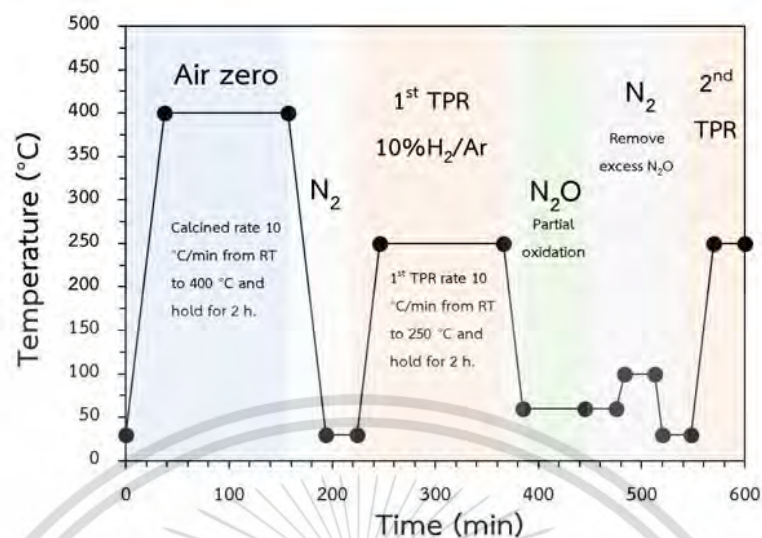


Figure C3 Temperature profile of dissociative N₂O adsorption using H₂-TPR for all catalysts (Note: Partial oxidize under N₂O at 60 °C for 1 h and flush under N₂ at 60 °C and 100 °C for 30 min then perform the 2nd TPR at the same condition as 1st TPR).

C4. Temperature program desorption (NH₃-TPD).

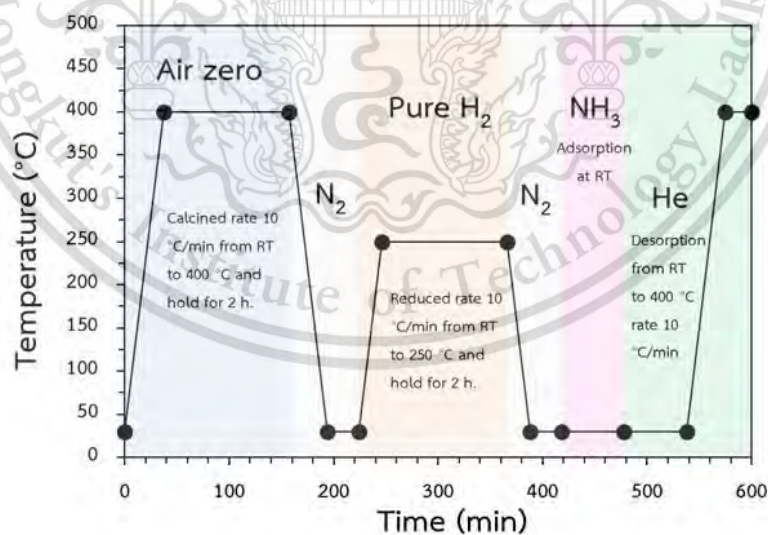


Figure C4 Temperature profile of temperature program desorption (NH₃-TPD) for all catalysts.

C5. Pyridine-adsorbed infrared spectroscopy (Py-FTIR).

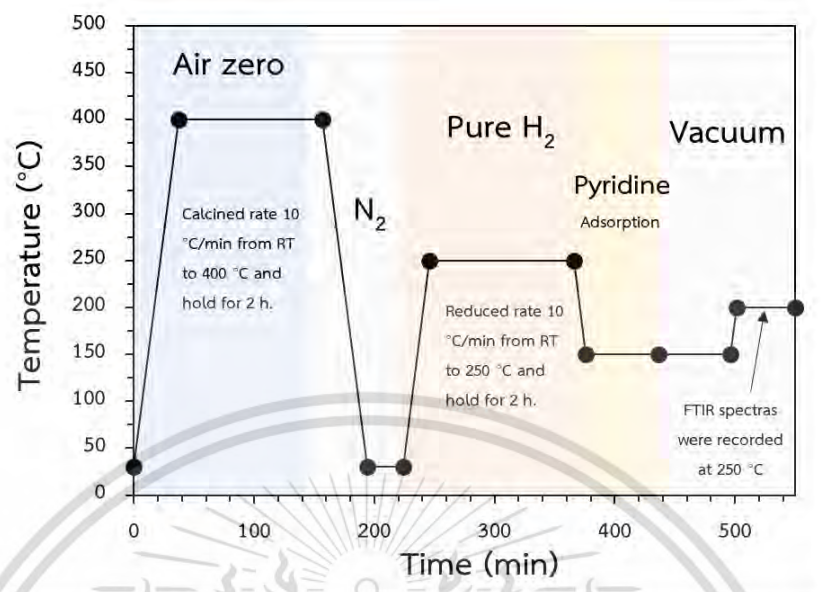


Figure C5 Temperature profile of Pyridine-adsorbed infrared spectroscopy (Py-FTIR) for all catalysts.

C6. *In situ* X-ray absorption near-edge structure (*in situ* TR-XANES)

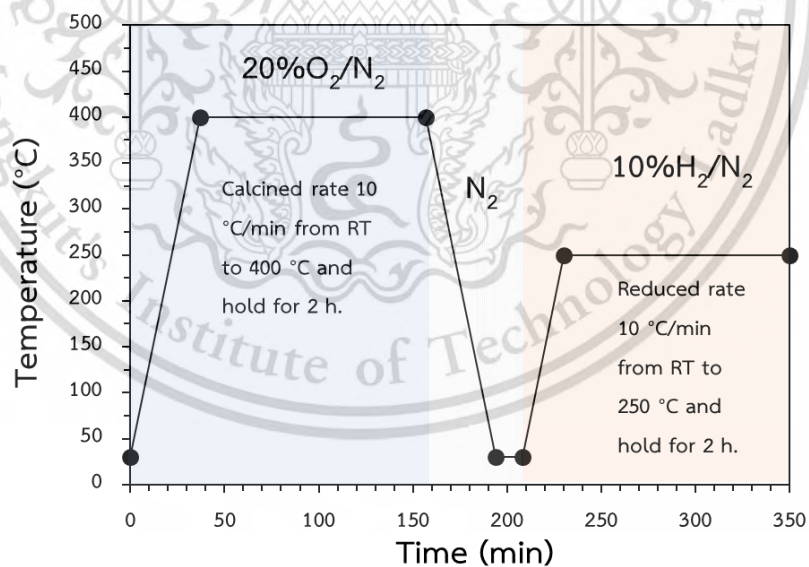


Figure C6 Temperature profile of *in situ* TR-XANES for all catalysts (Note: The spectrum was collected every 50 °C during calcination and every 2 °C during reduction).

C7. Catalytic reaction

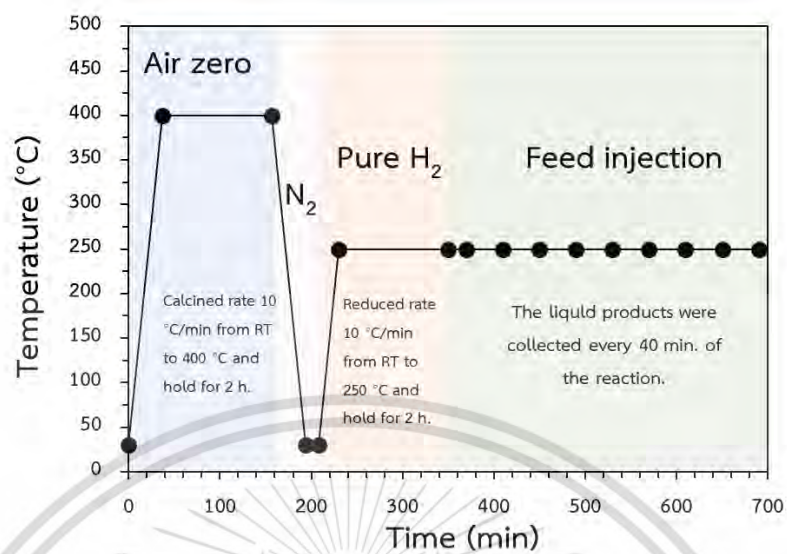


Figure C7 Temperature profile of the reaction for all catalysts.

C8. GC condition

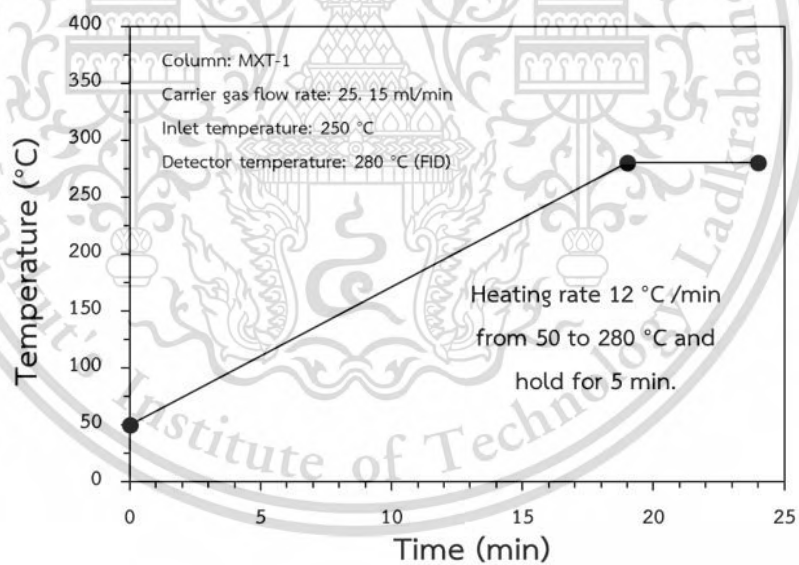


Figure C8 Temperature profile of the GC for all catalysts.

Appendix D

Calculations

D1. Quantitative analysis of H₂-TPR

H₂-TPR is a characterization technique that could provide both qualitative and quantitative results for the reduction of catalysts. Typically, the reducibility and active species of the catalyst could qualitatively be determined by the reduction temperature. In addition, the quantitative data such as H₂ consumption and metal loading on the catalyst could also be calculated by this technique.

The calculation of H₂ consumption from H₂-TPR

The H₂-consumption could be calculated by comparing between the integrated sample peak after reduction under 10%H₂/Ar and the integrated standard peak (1%H₂/Ar). Therefore, the 1%H₂/Ar standard would be pulsed at the end of each run. The amount of H₂ in 1%H₂/Ar standard would be calibrated using CuO as a standard. The reduction equation of CuO (Equation D1) and TPR profile (Figure D1) was shown as below.

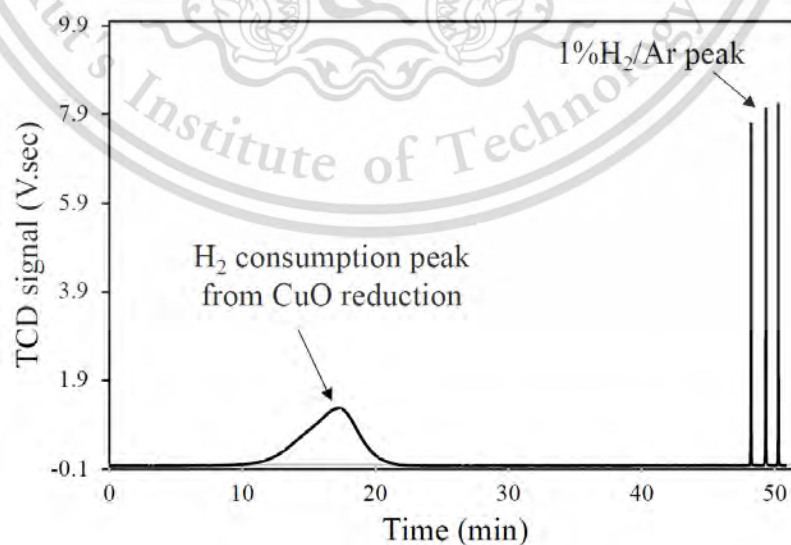
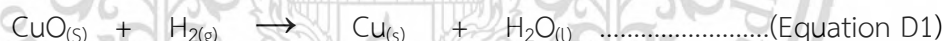


Figure D1 The TPR profiles of CuO after reduction under 10%H₂/Ar and standard pulse (1%H₂/Ar) at the end of run.

This material is reserved for educational use only, not allowed for commercial use.

Forbidden to modify the content, and cite the document when use.

Since the stoichiometric reduction of CuO requires 1 mol of H₂ (Equation D1). The 0.0045 g of CuO provide 6.2858 V.sec. of the peak area. Therefore, the amount of H₂ consumption on CuO standard could be calculated as follow;

$$\begin{aligned} \text{mol}_{\text{CuO}} &= \text{Mass}_{\text{CuO}} / M_{\text{w CuO}} \\ &= 0.0045 / 79.545 \text{ (g/g.mol}^{-1}\text{)} \\ &= 5.65718 \times 10^{-5} \text{ mol} \end{aligned}$$

According to Equation D.1

$$\begin{aligned} \text{mol}_{\text{CuO}} &= \text{mol}_{\text{H}_2} \\ \text{mol}_{\text{H}_2} &= 5.65718 \times 10^{-5} \text{ mol} \\ &= 56.57 \text{ } \mu\text{mol} \end{aligned}$$

Figure D2 shows that the relationship between CuO weight and H₂ consumption is linear as expected.

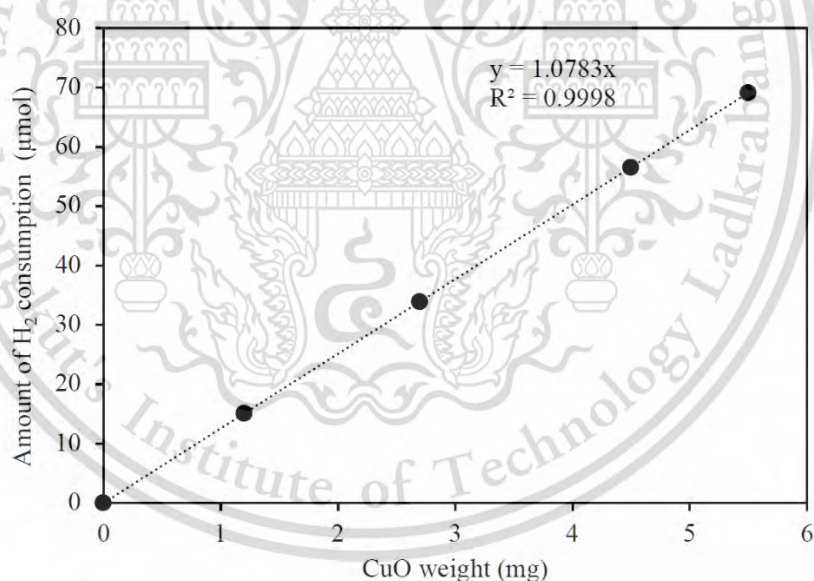


Figure D2 Relationship between CuO weight and amount of H₂ consumption.

To calculate the mol/pulse of 1%H₂/Ar, the integrated value of 6.2858 V.sec from the H₂ consumption peak of CuO reduction could equilibrate to 5.65718 × 10⁻⁵ mol. The average integrated 1%H₂/Ar peak is 0.08898 V.sec/pulse. Hence, the amount of H₂ in 1%H₂/Ar could be calculated as below.

$$\begin{aligned}
 \text{mol } 1\% \text{H}_2/\text{Ar} &= (\text{Integrated Area } 1\% \text{H}_2/\text{Ar} \times \text{mol}_{\text{CuO}}) / \text{Integrated Area}_{\text{CuO}} \\
 &= (0.008898 \times 5.65718 \times 10^{-5}) / 6.2858 \text{ mol/pulse} \\
 &= 8.0087 \times 10^{-7} \text{ mol/pulse}
 \end{aligned}$$

Since one pulse of 1% H_2 /Ar standard contain 8.0087×10^{-7} mol of H_2 . Then the H_2 consumption could be calculated from the peak area of the sample. For example, the sample area is 2.245 and the area of 1% H_2 /Ar pulse at that run is 0.0782. The H_2 -consumption could be calculated by

$$\begin{aligned}
 \text{The } \text{H}_2\text{-consumption} &= \frac{(\text{Sample area}) \times 0.00080087}{(\text{Standard area})} \\
 &= \frac{(2.245) \times 0.00080087}{(0.0782)} = 0.0230 \text{ mmol of } \text{H}_2
 \end{aligned}$$

If the sample was 0.0296 g for this run, Therefore, the H_2 -consumption in mmol/g would be $\left(\frac{0.0230 \text{ mmol}}{0.0296 \text{ g}}\right)$ equal to 0.7770 mmol/g.

The calculation of Cu loading on the catalyst from H_2 -TPR

The Cu loading (wt.%) over the catalyst could be estimated from the mole of H_2 that was consumed during the reduction. Since the CuPS contained Cu in the octahedral layer and inert support silica tetrahedral layer, it could assume that the H_2 consumption could only be obtained from the reduction of Cu in the octahedral layer with the same molar ratio of H_2 as mentioned in equation D1. For example, 0.015 g of CuPS catalyst consume 0.023 mmol of H_2 , the Cu loading (wt.%) over this catalyst could be calculated as follow;

$$\begin{aligned}
 \text{Cu loading (wt.\%)} &= \left(\frac{\text{Mole of } \text{H}_2 \text{ consumption (mmol)} \times \text{Mw of Cu (g/mol)}}{\text{Catalyst weight (mg)}} \right) \times 100 \\
 &= \left(\frac{0.0230 \text{ (mmol)} \times 63.5 \text{ (g/mol)}}{15 \text{ (mg)}} \right) \times 100 \\
 &= 9.73 \text{ wt.\%}
 \end{aligned}$$

This material is reserved for educational use only, not allowed for commercial use.

Forbidden to modify the content, and cite the document when use.

D2. Quantitative analysis of dissociative N₂O adsorption using H₂-TPR

Dissociative N₂O adsorption using H₂-TPR is a characterization technique that could evaluate the Cu dispersion (D_{Cu}) and also the specific Cu surface area (S_{Cu}^0) on the catalyst. The operation of this technique is similar with the H₂-TPR. Briefly, after the first H₂-TPR at 250 °C for 2 h, the sample was subsequently treated in a pure N₂O stream at 60 °C for 1 h. After that the N₂O was flushed with N₂ at 60 °C for 30 minute and then raised to 110 °C and hold for 30 minutes. Finally, the second H₂-TPR was then performed from room temperature to 250 °C. The example of peak profiles was shown in Figure D3.

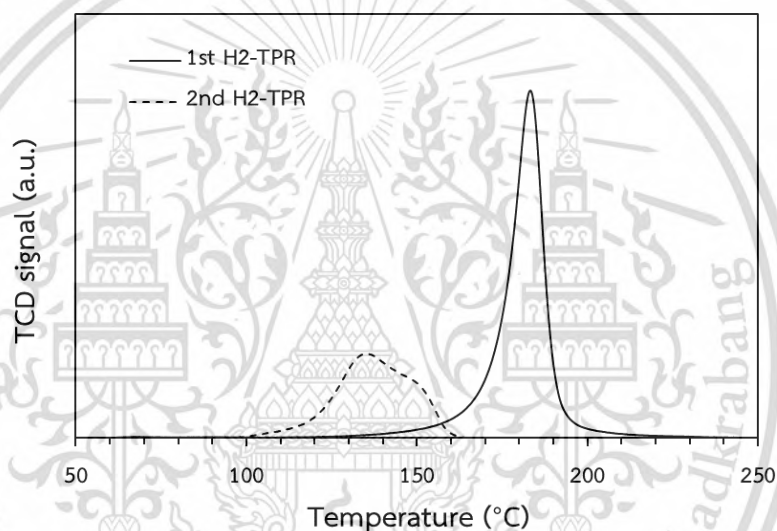
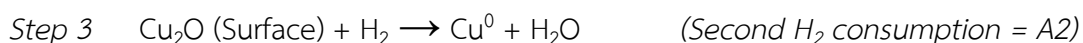
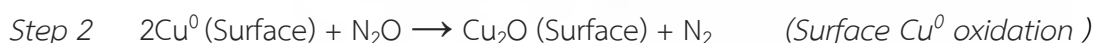


Figure D3 The TPR profiles of 20CuPS catalyst from the dissociative N₂O adsorption.

The copper dispersion (D_{Cu}) could be calculated from this following equation;



The value of copper dispersion (D_{Cu}) could be estimated as follow;

$$\text{Copper dispersion } (D_{Cu}) = \left(\frac{2 \times A2}{A1} \right) \times 100$$

This material is reserved for educational use only, not allowed for commercial use.

Forbidden to modify the content, and cite the document when use.

The specific surface area of copper (S_{Cu^0}) could also be estimated by

$$S_{Cu^0} (m^2/g) = \frac{2 \times A_2}{A_1} \times \left(\frac{\text{Avogadro's number}}{\text{Atomic weight of Cu} \times 1.4 \times 10^{19}} \right)$$

Where A_1 and A_2 are the H_2 consumption of 1st H_2 -TPR and 2nd H_2 -TPR respectively. The 1.4×10^{19} value is an average Cu atom surface area in atoms per square meter assuming that the Cu particle is spherical shape as described by Sagar, et al.

D3. Quantitative analysis of ammonia temperature program desorption (NH_3 -TPD)

The acidity on the catalysts could be calculated using ammonia temperature program desorption technique. The example of NH_3 desorption profile on 20CuPS catalyst was shown in Figure D4.

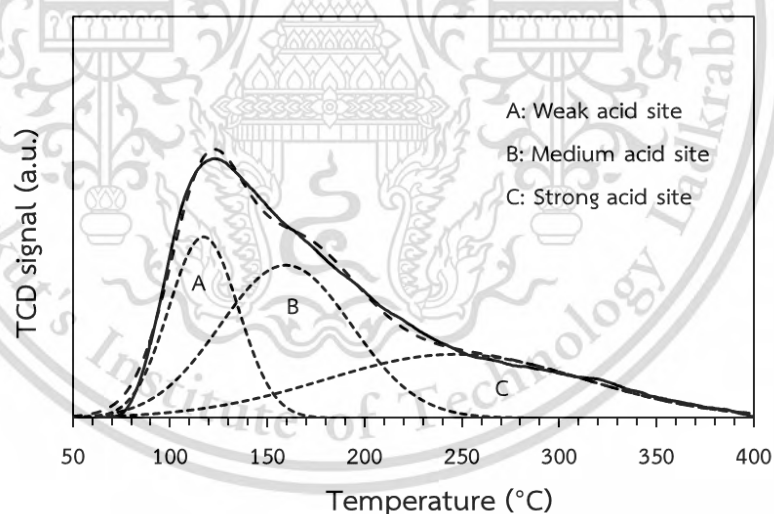


Figure D4 The TPD profiles of 20CuPS catalyst from 50 °C to 400 °C.

The NH_3 desorption profiles on 20CuPS could be divided into 3 peaks by the Gaussian deconvolution method. The low temperature NH_3 desorption (A) represents the weak acid site from surface silanol, while the medium acid site (B) and strong acid sites (C) refer to the NH_3 desorption on Cu surface and internal silanol, respectively.

The acidity of each deconvolution peak could be calculated by comparing between the integrated deconvolution peak area with the average area of standard pulse (1%NH₃/Ar) after the experiment as shown in Figure D5.

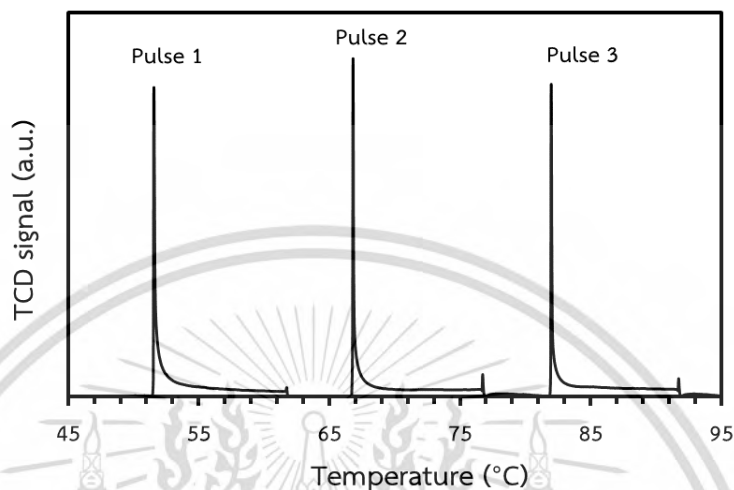


Figure D5 The peak of standard pulse (1%NH₃/Ar) at the end of run.

Since 1 pulse of 1%NH₃/Ar standard contains 1.7671×10^{-6} mmol of NH₃. Then, the acidity of each peak could be calculated by

$$\text{The acidity (mmol)} = \frac{(\text{Sample area}) \times 0.0000017671}{(\text{Average standard pulse area})}$$

For example;

The TPD profile of 20CuPS (0.04 g) contain 3 deconvolution peaks with difference integrated area including weak acid (34.36), medium acid (55.16) and strong acid (45.00). And the average standard pulse of 1%NH₃/Ar is 0.214034. The mmol of NH₃ for each peak could be calculated by

$$\begin{aligned} \text{The acidity of weak acid site (mmol)} &= \frac{(34.36) \times 0.0000017671}{(0.214034)} \\ &= 0.000283653 \text{ mmol} \\ &= 0.007091316 \text{ mmol/g} \end{aligned}$$

$$\begin{aligned} \text{The acidity of medium acid site (mmol)} &= \frac{(55.16) \times 0.0000017671}{(0.214034)} \\ &= 0.000455442 \text{ mmol} \\ &= 0.011386057 \text{ mmol/g} \end{aligned}$$

$$\begin{aligned} \text{The acidity of strong acid site (mmol)} &= \frac{(45.00) \times 0.0000017671}{(0.214034)} \\ &= 0.000371545 \text{ mmol} \\ &= 0.009288625 \text{ mmol/g} \end{aligned}$$

Therefore, the total acidity equal to

$$\begin{aligned} &= 0.007091316 + 0.011386057 + 0.009288625 \\ &= 0.027765998 \text{ mmol/g} \\ &= 27.77 \text{ } \mu\text{mol/g} \end{aligned}$$

D4. Quantitative analysis of pyridine adsorbed infrared spectroscopy (Py-IR)

The example of pyridine adsorption FT-IR spectra of 20CuPS was shown in Figure D7. The concentration ($\mu\text{mol/g}$) of lewis acid site (LAS) and brønsted acid site (BAS) on the catalyst could be calculated from the integrated peak area at 1450 cm^{-1} and 1540 cm^{-1} , respectively.

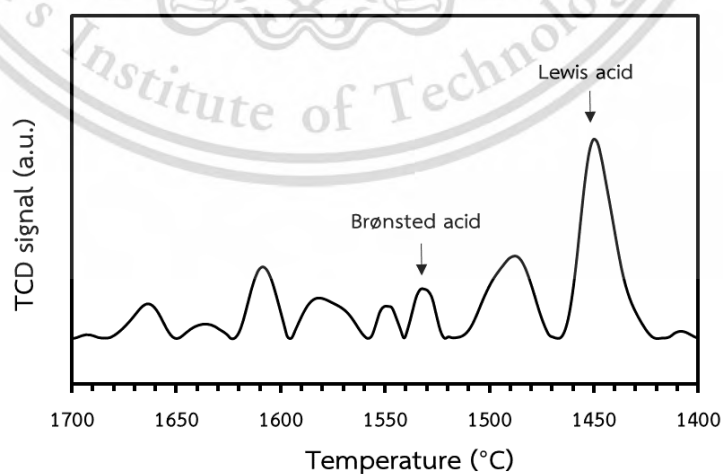


Figure D6 The pyridine-adsorbed IR spectra of 20CuPS.

The concentration of lewis acid site (LAS) at 1450 cm^{-1} and brønsted acid site (BAS) 1540 cm^{-1} on the catalyst could be calculated by R^2

$$C(L) = \text{IMEC (L)}^{-1} \times \text{IA(L)}_{1450} \times \frac{\pi R^2}{W}$$

$$C(B) = \text{IMEC (B)}^{-1} \times \text{IA(L)}_{1540} \times \frac{\pi R^2}{W}$$

Where:

$C(L)$ = The concentrations of Lewis acid sites ($\mu\text{mol/g}$)

$C(B)$ = The concentrations of Brønsted acid sites ($\mu\text{mol/g}$)

IA(L)_{1450} = The integrated areas of bands at 1450 cm^{-1}

IA(B)_{1540} = The integrated areas of bands at 1540 cm^{-1}

IMEC (L) = The integration molar extinction coefficients, $2.22\text{ cm} / \mu\text{mol}$

IMEC (B) = The integration molar extinction coefficients, $1.67\text{ cm} / \mu\text{mol}$

R = The wafer radius in cm

W = The wafer weight in g of the self-supporting catalyst disk.

D5. The calculation of Cu^0 , Cu^+ content Cu^0 at surface (Cu_s^0)

The copper metallic (Cu^0) and copper(I) oxide (Cu^+) content (mmol/g) were calculated from the Cu^0 and Cu^+ fraction based on mass of catalyst for each reaction. For example, 20CuPS contain 89.9% of Cu^0 with 10.1% of Cu^+ and the Cu content on 20CuPS is 0.7559 mmol, hence, the Cu^0 and Cu^+ content could be calculated by

$$\begin{aligned} \text{Cu}^0 \text{ content (mmol/g)} &= \frac{\text{mole of Cu} \times \text{Cu}^0 \text{ fraction}}{\text{Catalyst weight} \times 100} \\ &= \frac{0.7559 \text{ mmol} \times 89.9 \%}{0.25 \text{ g} \times 100} \\ &= 2.72 \text{ mmol/g} \end{aligned}$$

This material is reserved for educational use only, not allowed for commercial use.

Forbidden to modify the content, and cite the document when use.

$$\begin{aligned} \text{Cu}^+ \text{ content (mmol/g)} &= \frac{\text{mole of Cu} \times \text{Cu}^+ \text{ fraction}}{\text{Catalyst weight} \times 100} \\ &= \frac{0.7559 \text{ mmol} \times 10.1 \%}{0.25 \text{ g} \times 100} \\ &= 0.31 \text{ mmol/g} \end{aligned}$$

The copper metallic on surface (Cu_s^0 , mmol/g) could be calculated similar with specific Cu surface area by this equation

$$\text{Cu}_s^0 \text{ (mmol/g)} = \left(\frac{(\text{Cu dispersion}/100) \times \text{Avogadro's number}}{\text{Atomic weight of Cu} \times 1.4 \times 10^{19}} \right) \times \frac{\text{Cu}^0 \text{ (wt.\%)}}{100}$$

For example, the copper metallic on surface on 20CuPS equal to

$$\begin{aligned} \text{Cu}_s^0 \text{ (mmol/g)} &= \left(\frac{(72.9/100) \times 6.02 \times 10^{23}}{63.5 \times 1.4 \times 10^{19}} \right) \times \frac{17.26}{100} \\ &= 1.98 \text{ mmol/g} \end{aligned}$$

D6. Quantitative analysis of catalytic activity and reaction product

The quantitative analysis of catalytic activity and reaction products were carried out by gas chromatography using MXT-1 column with flame ionization detector (GC-FID). Before the analysis, 1 mL of liquid product and feed were diluted with heptane in a volumetric flask (5 mL) using 1 mL of *n*-octane as an internal standard. The chromatogram of feed and product solution were shown in Figure D8. The peak position of each product in the chromatogram was confirmed by GC-MS. The component in the solution could be ordered by the retention time as follow: *n*-Heptane (1.39), *n*-Octane (2.00), *n*-Dodecane (7.27), Hexadecene (12.77), Hexadecane (12.91), Hexadecanal (15.50), Hexadecanol (16.31) and Methyl palmitate (16.88).

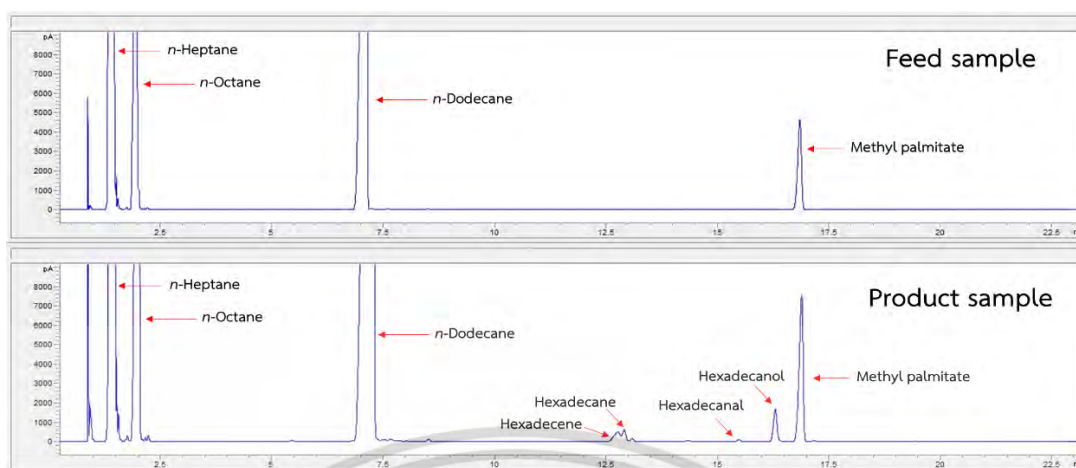


Figure D7 The chromatograms of feed and product sample.

The example of integrated peak area of components in solution with the response factor (RF) was shown in Table D1. The integrated peak area of each component was firstly corrected with the RF and then normalized with the peak area of internal standard (*n*-Octane). The equations for conversion, product yields and product selectivity calculation were shown as below.

Table D1 The example of integrated peak area, response factor (RF), corrected area with RF and normalized area with internal standard (*n*-Octane) of feed sample.

Component	Integrated peak area	RF	Corrected area with RF	Normalized area with <i>n</i> -Octane
<i>n</i> -Octane	147365.3	0.89	165578.99	1.0000
<i>n</i> -Dodecane	242996	1.09	222932.11	1.3464
Hexadecane	-	1.09	-	-
Hexadecene	-	1.09	-	-
Hexadecanal	-	1.09	-	-
Hexadecanol	-	1.05	-	-
Methyl palmitate (MP)	27297.4	1	27297.4	0.1649 (MP _{norm})

Table D2 The example of integrated peak area, response factor (RF), corrected area with RF and normalized area with internal standard (*n*-Octane) of product sample.

Component	Integrated peak area	RF	Corrected area with RF	Normalized area with <i>n</i> -Octane
<i>n</i> -Octane	95161.9	0.89	106923.48	1.0000
<i>n</i> -Dodecane	161106.8	1.09	147804.40	1.3823
Hexadecane	428.8	1.09	393.39	0.0037
Hexadecene	795.3	1.09	729.63	0.0068
Hexadecanal	425.6	1.09	405.33	0.0038
Hexadecanol	7141.7	1.05	6801.62	0.0636
Methyl palmitate (MP)	8014.7	1	8014.70	0.0750 (MP _{norm})

The conversion of methyl palmitate could be calculated as below.

$$\text{Conversion of MP (\%)} = \frac{(\text{MP}_{\text{norm}} \text{ in feed sample}) - (\text{MP}_{\text{norm}} \text{ in product sample})}{(\text{MP}_{\text{norm}} \text{ in feed sample})} \times 100$$

For example;

$$\begin{aligned} \text{Conversion of MP (\%)} &= \frac{(0.1649) - (0.075)}{(0.1649)} \times 100 \\ &= 54.52 \% \end{aligned}$$

The yield of each product could be calculated as below.

$$\text{Product yield (\%)} = \frac{(\text{Product}_{\text{norm}} \text{ in product sample})}{(\text{MP}_{\text{norm}} \text{ in feed sample})} \times 100$$

For example;

$$\begin{aligned} \text{Product yield of hexadecanol (\%)} &= \frac{(0.0636)}{(0.1649)} \times 100 \\ &= 38.57 \% \end{aligned}$$

This material is reserved for educational use only, not allowed for commercial use.

Forbidden to modify the content, and cite the document when use.

The selectivity of each product could be calculated as below.

$$\text{Product selectivity (\%)} = \frac{(\text{Yield of each product})}{(\text{Conversion})} \times 100$$

For example;

$$\begin{aligned} \text{Product selectivity of hexadecanol (\%)} &= \frac{(38.57)}{(54.52)} \times 100 \\ &= 70.74 \% \end{aligned}$$

D7. The calculation of contact time for the reaction

The catalyst contact time defined as the weight of catalysts bed divided by mole of feed that flow through the bed per hour. The contact time could be calculated as below.

$$\text{Contact time (g.h/mol)} = \frac{\text{weight of catalyst (g)}}{\text{mole of feed per h. } \left(\frac{\text{mol}}{\text{h}}\right)}$$

For example, 0.2516 g of 20CuPS were placed in the fixed-bed reactor. The 10% of methyl palmitate (MP) in dodecane were fed into the reactor with feed rate 2.4 mL/h. This mean that of MP was fed at rate 0.0007560 mol/h. Hence, the contact time could be calculate ed as following;

$$\begin{aligned} \text{Contact time (g.h/mol)} &= \frac{0.2516 \text{ (g)}}{0.0007560 \left(\frac{\text{mol}}{\text{h}}\right)} \\ &= 332 \text{ g.h/mol} \end{aligned}$$

Appendix E

The linear combination fitting (LCF) from

in situ TR-XANES

E1. The Cu fraction from LCF of 8CuPS during the calcination in 20%O₂/N₂ evaluated by Athena software with R-factor value.

Temperature	Cu fraction				R-factor
	Cu foil	Cu ₂ O	CuO	CuSO ₄	
50 °C	0	0	0.236	0.764	0.020221
100 °C	0	0	0.257	0.743	0.0013619
200 °C	0	0	0.294	0.706	0.0021313
300 °C	0	0	0.391	0.609	0.002824
400 °C	0	0	0.41	0.59	0.0029331
400 °C, 60 min	0	0	0.411	0.589	0.0039163
400 °C, 90 min	0	0	0.41	0.59	0.0040795
400 °C, 120 min	0	0	0.409	0.591	0.032563

E2. The Cu fraction from LCF of 20CuPS during the calcination in 20%O₂/N₂ evaluated by Athena software with R-factor value.

Temperature	Cu fraction				R-factor
	Cu foil	Cu ₂ O	CuO	CuSO ₄	
50 °C	0	0	0.339	0.661	0.002345
100 °C	0	0	0.353	0.647	0.001405
200 °C	0	0	0.404	0.596	0.0014
300 °C	0	0	0.467	0.533	0.001515
400 °C	0	0	0.466	0.534	0.003777
400 °C, 60 min	0	0	0.481	0.519	0.000957
400 °C, 90 min	0	0	0.489	0.511	0.000967
400 °C, 120 min	0	0	0.486	0.514	0.000943

E3. The Cu fraction from LCF of 30CuPS during the calcination in 20%O₂/N₂ evaluated by Athena software with R-factor value.

Temperature	Cu fraction				R-factor
	Cu foil	Cu ₂ O	CuO	CuSO ₄	
50 °C	0	0	0.386	0.614	0.002849
100 °C	0	0	0.405	0.595	0.002801
200 °C	0	0	0.47	0.53	0.003068
300 °C	0	0	0.485	0.515	0.001756
400 °C	0	0	0.488	0.512	0.004024
400 °C, 60 min	0	0	0.496	0.504	0.001195
400 °C, 90 min	0	0	0.503	0.497	0.001221
400 °C, 120 min	0	0	0.519	0.481	0.004078

E4. The Cu fraction from LCF of 20Cu/SiO₂ during the calcination in 20%O₂/N₂ evaluated by Athena software with R-factor value.

Temperature	Cu fraction				R-factor
	Cu foil	Cu ₂ O	CuO	CuSO ₄	
50 °C	0	0	1	0	0.000578
100 °C	0	0	1	0	0.000627
200 °C	0	0	1	0	0.000627
300 °C	0	0	1	0	0.000731
400 °C	0	0	1	0	0.000828
400 °C, 60 min	0	0	1	0	0.001486
400 °C, 90 min	0	0	1	0	0.001748
400 °C, 120 min	0	0	1	0	0.001784

E5. The Cu fraction from LCF of 0.05K-CuPS during the calcination in 20%O₂/N₂ evaluated by Athena software with R-factor value.

Temperature	Cu fraction				R-factor
	Cu foil	Cu ₂ O	CuO	CuSO ₄	
50 °C	0	0	35.4	64.6	0.003236
80 °C	0	0	36.6	63.4	0.003935
100 °C	0	0	37.1	62.9	0.003874
200 °C	0	0	38.4	61.6	0.003779
300 °C	0	0	40.4	59.6	0.003723
400 °C	0	0	41.7	58.3	0.007477
400 °C, 60 min	0	0	42.1	57.9	0.008872
400 °C, 90 min	0	0	42	58	0.008336
400 °C, 120 min	0	0	41.7	58.3	0.009079

E6. The Cu fraction from LCF of 8CuPS during the reduction in 10%H₂/N₂ evaluated by Athena software with R-factor value.

Temperature	Cu fraction				R-factor
	Cu foil	Cu ₂ O	CuO	CuSO ₄	
50 °C	0	0	0.418	0.582	0.010762
60 °C	0	0	0.418	0.582	0.010872
70 °C	0	0	0.417	0.583	0.010643
80 °C	0	0	0.433	0.567	0.0084694
90 °C	0	0	0.442	0.558	0.0084048
100 °C	0	0	0.441	0.559	0.0096864
110 °C	0	0	0.451	0.549	0.0099974
120 °C	0	0	0.458	0.542	0.010156
130 °C	0	0	0.471	0.529	0.0091349
140 °C	0	0	0.476	0.524	0.010063
150 °C	0	0	0.49	0.51	0.0098353
160 °C	0	0	0.507	0.493	0.0077314
170 °C	0	0	0.519	0.481	0.0091862
180 °C	0	0	0.543	0.457	0.0082255

This material is reserved for educational use only, not allowed for commercial use.

Forbidden to modify the content, and cite the document when use.

Temperature	Cu fraction				R-factor
	Cu foil	Cu ₂ O	CuO	CuSO ₄	
190 °C	0	0	0.558	0.442	0.0090402
200 °C	0	0	0.595	0.405	0.0077947
210 °C	0	0	0.654	0.346	0.0075459
220 °C	0	0.14	0.622	0.238	0.0006256
230 °C	0.011	0.4	0.521	0.068	0.0018566
240 °C	0.452	0.408	0.14	0	0.0013376
250 °C	0.767	0.233	0	0	0.0024208
250 °C, 10 min	0.785	0.215	0	0	0.0028718
250 °C, 20 min	0.794	0.206	0	0	0.0029658
250 °C, 30 min	0.815	0.185	0	0	0.0030334
250 °C, 40 min	0.814	0.186	0	0	0.0029981
250 °C, 50 min	0.82	0.18	0	0	0.0031683
250 °C, 60 min	0.829	0.171	0	0	0.0032587
250 °C, 70 min	0.828	0.172	0	0	0.0031854
250 °C, 80 min	0.831	0.169	0	0	0.0033289
250 °C, 90 min	0.823	0.177	0	0	0.0033043
250 °C, 100 min	0.833	0.167	0	0	0.0034068
250 °C, 110 min	0.832	0.168	0	0	0.0034646
250 °C, 120 min	0.838	0.162	0	0	0.003342

E7. The Cu fraction from LCF of 20CuPS during the reduction in 10%H₂/N₂ evaluated by Athena software with R-factor value.

Temperature	Cu fraction				R-factor
	Cu foil	Cu ₂ O	CuO	CuSO ₄	
50 °C	0	0	0.474	0.526	0.001647
60 °C	0	0	0.477	0.523	0.002655
70 °C	0	0	0.468	0.532	0.001666
80 °C	0	0	0.464	0.536	0.001411
90 °C	0	0	0.47	0.53	0.001603
100 °C	0	0	0.472	0.528	0.001598

This material is reserved for educational use only, not allowed for commercial use.

Forbidden to modify the content, and cite the document when use.

Temperature	Cu fraction				R-factor
	Cu foil	Cu ₂ O	CuO	CuSO ₄	
110 °C	0	0	0.477	0.523	0.001571
120 °C	0	0	0.481	0.519	0.001557
130 °C	0	0	0.488	0.512	0.001542
140 °C	0	0	0.494	0.506	0.001506
150 °C	0	0	0.505	0.495	0.001466
160 °C	0	0	0.513	0.487	0.001409
170 °C	0	0	0.527	0.473	0.001339
180 °C	0	0	0.552	0.448	0.001256
190 °C	0	0	0.58	0.42	0.001225
200 °C	0	0	0.632	0.368	0.001279
210 °C	0	0.175	0.467	0.358	0.000937
220 °C	0	0.435	0.403	0.163	0.002255
230 °C	0.646	0.192	0.122	0.04	0.000795
240 °C	0.756	0.148	0.089	0.006	0.000752
250 °C	0.807	0.152	0.041	0	0.000697
250 °C, 10 min	0.859	0.141	0	0	0.001002
250 °C, 20 min	0.869	0.131	0	0	0.001152
250 °C, 30 min	0.878	0.122	0	0	0.001248
250 °C, 40 min	0.883	0.117	0	0	0.00133
250 °C, 50 min	0.885	0.115	0	0	0.001388
250 °C, 60 min	0.889	0.111	0	0	0.001453
250 °C, 70 min	0.889	0.111	0	0	0.001492
250 °C, 80 min	0.892	0.108	0	0	0.001529
250 °C, 90 min	0.894	0.106	0	0	0.001578
250 °C, 100 min	0.894	0.106	0	0	0.001578
250 °C, 110 min	0.898	0.102	0	0	0.001646
250 °C, 120 min	0.899	0.101	0	0	0.001675

This material is reserved for educational use only, not allowed for commercial use.

Forbidden to modify the content, and cite the document when use.

E8. The Cu fraction from LCF of 30CuPS during the reduction in 10% H_2/N_2 evaluated by Athena software with R-factor value.

Temperature	Cu fraction				R-factor
	Cu foil	Cu ₂ O	CuO	CuSO ₄	
50 °C	0	0	0.533	0.467	0.004312
60 °C	0	0	0.542	0.458	0.004169
70 °C	0	0	0.542	0.458	0.004215
80 °C	0	0	0.545	0.455	0.004148
90 °C	0	0	0.549	0.451	0.004167
100 °C	0	0	0.552	0.448	0.004075
110 °C	0	0	0.556	0.444	0.004093
120 °C	0	0	0.561	0.439	0.003951
130 °C	0	0	0.563	0.437	0.003887
140 °C	0	0	0.572	0.428	0.003792
150 °C	0	0	0.578	0.422	0.003687
160 °C	0	0	0.589	0.411	0.003451
170 °C	0	0	0.604	0.396	0.003176
180 °C	0	0	0.623	0.377	0.002796
190 °C	0	0	0.659	0.314	0.002252
200 °C	0	0	0.733	0.267	0.001487
210 °C	0.015	0.095	0.705	0.185	0.000848
220 °C	0.116	0.37	0.514	0	0.001094
230 °C	0.659	0.227	0.115	0	0.000875
240 °C	0.812	0.116	0.072	0	0.001
250 °C	0.838	0.128	0.034	0	0.001056
250 °C, 10 min	0.877	0.123	0	0	0.001212
250 °C, 20 min	0.891	0.109	0	0	0.001269
250 °C, 30 min	0.896	0.104	0	0	0.001372
250 °C, 40 min	0.903	0.097	0	0	0.001445
250 °C, 50 min	0.905	0.095	0	0	0.001486
250 °C, 60 min	0.907	0.093	0	0	0.001561
250 °C, 70 min	0.91	0.09	0	0	0.001562

This material is reserved for educational use only, not allowed for commercial use.

Forbidden to modify the content, and cite the document when use.

Temperature	Cu fraction				R-factor
	Cu foil	Cu ₂ O	CuO	CuSO ₄	
250 °C, 80 min	0.915	0.085	0	0	0.00166
250 °C, 90 min	0.917	0.083	0	0	0.001729
250 °C, 100 min	0.916	0.084	0	0	0.001725
250 °C, 110 min	0.92	0.08	0	0	0.001746
250 °C, 120 min	0.924	0.076	0	0	0.001813

E9. The Cu fraction from LCF of 20Cu/SiO₂ during the reduction in 10%H₂/N₂ evaluated by Athena software with R-factor value.

Temperature	Cu fraction				R-factor
	Cu foil	Cu ₂ O	CuO	CuSO ₄	
50 °C	0	0	1	0	0.000784
60 °C	0	0	1	0	0.000754
70 °C	0	0	1	0	0.000756
80 °C	0	0	1	0	0.000733
90 °C	0	0	1	0	0.000737
100 °C	0.01	0	0.99	0	0.00072
110 °C	0.011	0	0.989	0	0.000726
120 °C	0.015	0	0.985	0	0.000689
130 °C	0.013	0	0.987	0	0.000679
140 °C	0.016	0	0.984	0	0.000695
150 °C	0.018	0	0.982	0	0.000689
160 °C	0.022	0	0.978	0	0.000684
170 °C	0.023	0	0.977	0	0.000689
180 °C	0.03	0	0.97	0	0.000673
190 °C	0.036	0	0.964	0	0.000646
200 °C	0.043	0	0.957	0	0.000656
210 °C	0.054	0	0.946	0	0.000649
220 °C	0.081	0	0.919	0	0.000612
230 °C	0.142	0	0.858	0	0.000551

This material is reserved for educational use only, not allowed for commercial use.

Forbidden to modify the content, and cite the document when use.

Temperature	Cu fraction				R-factor
	Cu foil	Cu ₂ O	CuO	CuSO ₄	
240 °C	0.318	0	0.682	0	0.000592
250 °C	1	0	0	0	0.001673
250 °C, 10 min	1	0	0	0	0.002096
250 °C, 20 min	1	0	0	0	0.002151
250 °C, 30 min	1	0	0	0	0.002268
250 °C, 40 min	1	0	0	0	0.002299
250 °C, 50 min	1	0	0	0	0.002387
250 °C, 60 min	1	0	0	0	0.002466
250 °C, 70 min	1	0	0	0	0.002599
250 °C, 80 min	1	0	0	0	0.002664
250 °C, 90 min	1	0	0	0	0.002709
250 °C, 100 min	1	0	0	0	0.002728
250 °C, 110 min	1	0	0	0	0.002721
250 °C, 120 min	1	0	0	0	0.002781

E10. The Cu fraction from LCF of 0.05K-CuPS during the reduction in 10%H₂/N₂ evaluated by Athena software with R-factor value.

Temperature	Cu fraction				R-factor
	Cu foil	Cu ₂ O	CuO	CuSO ₄	
50 °C	0	0	0.677	0.323	0.002235
60 °C	0	0	0.689	0.311	0.002203
70 °C	0	0	0.715	0.285	0.003081
80 °C	0	0	0.723	0.277	0.002428
90 °C	0	0	0.741	0.259	0.002993
100 °C	0	0	0.76	0.24	0.003596
110 °C	0	0	0.776	0.224	0.003747
120 °C	0	0	0.783	0.217	0.002935
130 °C	0	0	0.797	0.203	0.003576
140 °C	0	0	0.81	0.19	0.00359

This material is reserved for educational use only, not allowed for commercial use.

Forbidden to modify the content, and cite the document when use.

Temperature	Cu fraction				R-factor
	Cu foil	Cu ₂ O	CuO	CuSO ₄	
150 °C	0	0	0.829	0.171	0.004271
160 °C	0	0	0.848	0.152	0.004038
170 °C	0	0	0.883	0.117	0.004724
180 °C	0	0	0.908	0.092	0.001648
190 °C	0	0	0.978	0.022	0.002262
200 °C	0.121	0.013	0.866	0	0.001901
210 °C	0.136	0.133	0.731	0	0.002638
220 °C	0.287	0.314	0.399	0	0.001418
230 °C	0.408	0.452	0.14	0	0.00208
240 °C	0.721	0.233	0.046	0	0.000876
250 °C	0.78	0.22	0	0	0.000797
250 °C, 10 min	0.808	0.192	0	0	0.000997
250 °C, 20 min	0.825	0.175	0	0	0.001117
250 °C, 30 min	0.835	0.165	0	0	0.001194
250 °C, 40 min	0.841	0.159	0	0	0.001277
250 °C, 50 min	0.847	0.153	0	0	0.001301
250 °C, 60 min	0.85	0.15	0	0	0.001366
250 °C, 70 min	0.856	0.144	0	0	0.001348
250 °C, 80 min	0.858	0.142	0	0	0.001471
250 °C, 90 min	0.864	0.136	0	0	0.001514
250 °C, 100 min	0.865	0.135	0	0	0.001557
250 °C, 110 min	0.864	0.136	0	0	0.001596
250 °C, 120 min	0.859	0.141	0	0	0.001679

This material is reserved for educational use only, not allowed for commercial use.

Forbidden to modify the content, and cite the document when use.

E10. The Cu fraction from LCF of 0.01K-CuPS during the reduction in 10% H_2/N_2 evaluated by Athena software with R-factor value.

Temperature	Cu fraction				R-factor
	Cu foil	Cu ₂ O	CuO	CuSO ₄	
50 °C	0	0	0.796	0.204	0.001888
60 °C	0	0	0.806	0.194	0.001878
70 °C	0	0	0.818	0.182	0.001969
80 °C	0	0	0.83	0.17	0.002023
90 °C	0	0	0.854	0.146	0.002075
100 °C	0	0	0.854	0.146	0.002103
110 °C	0	0	0.864	0.136	0.002198
120 °C	0	0	0.876	0.124	0.002242
130 °C	0	0	0.886	0.114	0.002341
140 °C	0	0	0.896	0.104	0.002331
150 °C	0	0	0.908	0.092	0.002393
160 °C	0	0	0.945	0.055	0.002411
180 °C	0.033	0	0.967	0	0.002449
200 °C	0.043	0.051	0.907	0	0.002785
210 °C	0.033	0.172	0.796	0	0.003686
220 °C	0.038	0.342	0.619	0	0.005767
230 °C	0.149	0.521	0.33	0	0.003936
240 °C	0.41	0.498	0.092	0	0.00334
250 °C	0.844	0.147	0.009	0	0.000984
250 °C, 10 min	0.878	0.122	0	0	0.001086
250 °C, 20 min	0.889	0.111	0	0	0.001114
250 °C, 30 min	0.895	0.105	0	0	0.001131
250 °C, 40 min	0.898	0.102	0	0	0.001146
250 °C, 50 min	0.898	0.102	0	0	0.001153
250 °C, 60 min	0.9	0.1	0	0	0.001163
250 °C, 70 min	0.902	0.098	0	0	0.001165
250 °C, 80 min	0.901	0.099	0	0	0.001168
250 °C, 90 min	0.899	0.101	0	0	0.001158

This material is reserved for educational use only, not allowed for commercial use.

Forbidden to modify the content, and cite the document when use.

Temperature	Cu fraction				R-factor
	Cu foil	Cu ₂ O	CuO	CuSO ₄	
250 °C, 100 min	0.901	0.099	0	0	0.001167
250 °C, 110 min	0.904	0.096	0	0	0.001188
250 °C, 120 min	0.9	0.1	0	0	0.001186

E10. The Cu fraction from LCF of 0.10K-CuPS during the reduction in 10%H₂/N₂ evaluated by Athena software with R-factor value.

Temperature	Cu fraction				R-factor
	Cu foil	Cu ₂ O	CuO	CuSO ₄	
50 °C	0	0	0.634	0.366	0.005402
60 °C	0	0	0.651	0.349	0.005494
70 °C	0	0	0.669	0.331	0.005659
80 °C	0	0	0.686	0.314	0.005707
90 °C	0	0	0.701	0.299	0.005799
100 °C	0	0	0.713	0.287	0.00583
110 °C	0	0	0.726	0.274	0.005737
120 °C	0	0	0.739	0.261	0.005773
130 °C	0	0	0.753	0.247	0.005571
140 °C	0	0	0.766	0.234	0.005415
150 °C	0	0	0.784	0.216	0.005201
160 °C	0	0	0.81	0.19	0.004884
170 °C	0	0	0.852	0.148	0.004549
180 °C	0	0	0.908	0.092	0.004436
190 °C	0	0	0.995	0.005	0.004696
200 °C	0.079	0.008	0.913	0	0.005771
210 °C	0.117	0.157	0.726	0	0.008228
220 °C	0.248	0.362	0.39	0	0.006357
230 °C	0.507	0.384	0.109	0	0.002866
240 °C	0.784	0.187	0.029	0	0.000688
250 °C	0.814	0.182	0.004	0	0.000754

This material is reserved for educational use only, not allowed for commercial use.

Forbidden to modify the content, and cite the document when use.

Temperature	Cu fraction				R-factor
	Cu foil	Cu ₂ O	CuO	CuSO ₄	
250 °C, 10 min	0.834	0.166	0	0	0.000878
250 °C, 20 min	0.839	0.161	0	0	0.009251
250 °C, 30 min	0.841	0.159	0	0	0.000936
250 °C, 40 min	0.842	0.158	0	0	0.000976
250 °C, 50 min	0.843	0.157	0	0	0.000961
250 °C, 60 min	0.841	0.159	0	0	0.000961
250 °C, 70 min	0.842	0.158	0	0	0.000962
250 °C, 80 min	0.837	0.163	0	0	0.000955
250 °C, 90 min	0.837	0.163	0	0	0.000959
250 °C, 100 min	0.838	0.162	0	0	0.000995
250 °C, 110 min	0.837	0.163	0	0	0.000969
250 °C, 120 min	0.837	0.163	0	0	0.000962

This material is reserved for educational use only, not allowed for commercial use.

Forbidden to modify the content, and cite the document when use.

Author Biography

Name	Mr. Warot Prasanseang
Date of Birth	2 December 1991
Address	50/1, Anusawari, Bang Khen, Bangkok, 10220
Education	(2014) Bachelor of Science in Industrial Chemistry GPA 2.77 King Mongkut's Institute of Technology Ladkrabang (2016) Master of Science in Chemistry GPA 3.75 King Mongkut's Institute of Technology Ladkrabang
Scholarship	KMITL Doctoral Scholarship (KDS2018/009)

Academic publications

1. Tuning Cu^+ species/Brønsted acids of copper phyllosilicate by K^+ doping for selective hydrogenation of methyl palmitate to hexadecanol
Journal of Catalysis, 2023, 428, 115115.
2. Linear long-chain α -olefins from hydrodeoxygenation of methyl palmitate over copper phyllosilicate catalysts.
Applied Catalysis A: General, 2022, 5, 635, 118555.
3. Effect of Synthesized Ag Nanoparticles by Using the Different Amounts of Polyvinylpyrrolidone for Ag-Natural Rubber Hybrid Sheets and their Antibacterial Properties.
Key Engineering Materials, 2017, 25, 751, 270-6.